UNIVERSIDADE D
COIMBRA

Ana Íris Dias Machado

TIME-GATED FLUORESCENCE LIFETIME MICROSCOPE WITH LIGHT-SHEET ILLUMINATION

Thesis submitted to the University of Coimbra in fulfillment of the requirements for the Master's Degree in Physics Engineering under the scientific supervision of Professor António Miguel Lino Santos Morgado

October of 2021

University of Coimbra

Integrated Master's in Engineering Physics

Time-Gated Fluorescence Lifetime Microscope with Light-Sheet Illumination

---

Ana Íris Dias Machado

Thesis submitted to the University of Coimbra in fulfillment of the requirements for the Master's Degree in Physics Engineering

Supervisor:
Professor António Miguel Lino Santos Morgado

Coimbra, October of 2021

Aos meus pais...

Agradecimentos

Primeiramente, gostaria de agradecer ao meu orientador Professor Doutor Miguel Morgado pela disponibilidade, ensinamentos e orientação do trabalho para a direção certa de modo a concluir o projeto. A sua calma e positividade ajudaram a não me desmotivar durante a realização do projeto. Obrigada pelo voto de confiança. Agradeço à Doutora Ana Batista e ao Carlos Correia pela disponibilidade e ajuda. Agradeço também à minha colega Diana pela companhia no laboratório.

Agradeço aos meus pais Cristina e Walter e aos meus irmãos Ana Catarina e João Valter por todo o carinho, educação e conselhos que me concederam e por me terem ajudado a crescer. Obrigada por me ensinarem a confiar nas minhas decisões, pela motivação e apoio para alcançar todos os meus objetivos.

Agradeço à minha prima Leonor e aos meus tios Ana Maria e José Luís pela preocupação e motivação que me deram para realizar e terminar o projeto.

Agradeço ao João por ser a pessoa maravilhosa que é, por me apoiar e incentivar incessantemente e por estar ao meu lado em todas as situações e dificuldades. Obrigada por toda a tua incansável ajuda durante o meu percurso académico e pela tua paciência infinita.

O meu muito obrigada.

Abstract

Time-Gated fluorescence lifetime microscopy is based on the fluorescence decay process and allows to observe the spatial distribution of the fluorophores contained in a sample through their lifetime. The emitted photons from the sample are acquired in successive temporal gates with delays relative to the excitation pulse, resulting in a mono or multi-exponential decay curve used to determine the fluorescence lifetimes. This microscopy technique allows functional imaging of biological metabolism, based on the endogenous fluorescence of metabolic co-factors NAD(P)H and FAD.

In this work, it was implemented a Time-Gated fluorescence lifetime microscope with light-sheet illumination at 440 nm for fluorescence imaging in the range between 520 and 570 nm, in thick biological tissues. Also, it was evaluated, through computational simulations, the accuracy and precision of the Rapid Lifetime Determination (RLD) algorithm to estimate the parameters of the fluorescence decay.

The system was characterized through tests of optical and timing parameters. The axial resolution of the system is in the range of 20 μm. The timing parameter corresponds to the accuracy of the measurements of fluorescence lifetime and depends on the gate width used for acquisitions. The relative error of the fluorescence lifetime estimation is in the range of 5 to 14%. The system was tested using animal corneas.

The obtained parameters met the system requirements, except the optical sectioning that exceeds the value in more than 6 μm. However, the implemented microscope works as expected and allows the evaluation of its application for imaging biological samples. The system needs to be improved to decrease the light-sheet thickness and increase the optical sectioning to obtain images of thick tissues with adequate contrast.

The computational evaluation of the RLD algorithm showed that it is not suitable for metabolic imaging based on the ratio of the pre-exponential factors of the FAD decay. The accuracy of this ratio is always worse than 20%, even for high values of total counts.

Keywords: Time-Gated, Fluorescence lifetime microscopy, Light-sheet, Corneas, Rapid Lifetime Determination

Resumo

A microscopia de tempo de vida de fluorescência Time-Gated baseia-se no processo de decaimento de fluorescência e permite observar a distribuição espacial dos fluoróforos contidos na amostra através do seu tempo de vida. Os fotões emitidos pela amostra são adquiridos em sucessões de janelas temporais com atrasos relativos ao pulso de excitação, resultando numa curva de decaimento mono ou multi-exponencial de onde é possível retirar os tempos de vida de fluorescência. Esta técnica de microscopia constitui um método de imagiologia funcional do metabolismo biológico, baseado na fluorescência endógena dos cofactores metabólicos NAD(P)H e FAD.

O trabalho desenvolvido consiste na implementação de um microscópio de tempo de vida de fluorescência Time-Gated com iluminação light-sheet a 440 nm para imagiologia de fluorescência entre os 520 e 570 nm, em tecidos biológicos espessos. Procedeu-se ainda, à avaliação da exatidão e precisão do algoritmo Rapid Lifetime Determination (RLD) para a determinação dos parâmetros do decaimento de fluorescência através de simulações computacionais.

A sistema foi caracterizado através de testes dos parâmetros óticos e temporais. A resolução axial do sistema é da ordem dos 20 μm. O parâmetro temporal corresponde à exatidão das medições de tempo de vida de fluorescência e depende da largura da gate utilizada para as aquisições. O erro relativo da estimativa dos tempos de vida encontra-se entre os 5 e 14%. Por fim, testou-se o sistema com córneas animais.

Os parâmetros obtidos cumpriram os requisitos do sistema, exceto o seccionamento ótico que se excedeu em mais de 6 μm. No entanto, o sistema implementado é funcional e permitiu avaliar a sua aplicação em imagiologia de amostras biológicas. O sistema necessita de ser otimizado de modo a reduzir a espessura da light-sheet e aumentar o seccionamento ótico para obter imagens com contraste adequado de tecidos espessos.

A avaliação computacional do algoritmo RLD mostrou que este não é adequado para imagiologia metabólica baseada na razão dos fatores pre-exponenciais do decaimento do FAD. A exatidão desta razão é sempre pior que 20%, mesmo para contagens totais elevadas.

Palavras-chave: Time-Gated, Microscopia de tempo de vida de fluorescência, Light-sheet, Córneas, Rapid Lifetime Determination

Contents

Acknowledgments **i**

Abstract **iii**

Resumo **v**

List of Figures **xv**

List of Tables **xviii**

Acronyms **xix**

1 Introduction **1**

1.1 Objectives 2

1.2 Context and motivation 2

1.3 Requirements analysis 3

1.4 Thesis content 3

2 Fluorescence lifetime imaging microscopy principles and state of the art **5**

2.1 Fluorescence process 6

2.2 Fluorescence Lifetime Imaging Microscopy 8

2.3 FLIM acquisition techniques 9

2.3.1 Time-Correlated Single Photon Counting technique 9

2.3.2 Time-Gated technique 11

2.4 Image formation techniques 12

2.5 Light-Sheet Fluorescence Microscopy 13

2.5.1 Developments in LSFM . . . 14
2.5.2 Applications of FLIM-LSFM . . . 15
2.6 Fluorescence lifetime determination . . . 16
2.6.1 Instrument Response Function . . . 16
2.6.2 FLIMfit software . . . 16
2.6.3 Rapid Lifetime Determination . . . 17

3 Microscope implementation 21
3.1 System components . . . 22
3.1.1 Light source . . . 23
3.1.2 HRI delay unit . . . 25
3.1.3 High Rate Imager (HRI) . . . 25
3.1.4 CCD . . . 27
3.1.5 DaVis software . . . 28
3.2 Optical components . . . 28
3.2.1 Infinity-corrected microscope objective . . . 29
3.2.2 Tube lens . . . 29
3.2.3 Telecentric objective . . . 30
3.2.4 Spherical and cylindrical lenses . . . 31
3.2.5 Emission filters . . . 31
3.3 Microscope setup . . . 32

4 Microscope evaluation 35
4.1 Field of view . . . 36
4.2 Light-sheet thickness . . . 41
4.3 Axial resolution . . . 45
4.4 Lateral resolution . . . 49
4.5 Timing accuracy . . . 51
4.6 Results evaluation . . . 54

5 Corneal imaging tests 55

5.1 Introduction 56
5.2 Animal corneas imaging 57
5.3 Discussion 64

6 Computational evaluation of Rapid Lifetime Determination algorithm 67
6.1 Methods 68
6.2 Results 71
6.3 Discussion 73

7 Conclusions 77
7.1 Conclusions 78
7.2 Future work 79

References 81

Appendix A Data analysis 89

Appendix B Fluorescence decay of cornea images 95

Appendix C Simulations 99

List of Figures

2.1 Diagram of the fluorescence process 6

2.2 The General setup for a TCSPC FLIM acquisition system 10

2.3 Diagram of the principle of Time-Gated FLIM 11

2.4 The General setup for a Time-Gated FLIM acquisition system 12

2.5 Principle of LSFM 14

2.6 Graphic of the contiguous areas for a mono-exponential decay 18

2.7 Graphic of the four integrated areas in a bi-exponential decay 18

3.1 Diagram of the implemented Time-Gated fluorescence lifetime microscope with a light-sheet illumination 23

3.2 Pulsed diode laser 24

3.3 Multichannel picosecond diode laser driver 24

3.4 Image of the elliptical shape of the diode laser 24

3.5 HRI trigger delay unit 25

3.6 HRI and the HRI controller module 26

3.7 Quantum efficiency of the photocathode 26

3.8 Quantum efficiency of VGA sensor of the CCD camera 28

3.9 Infinity-corrected microscope objectives 29

3.10 Tube lens 30

3.11 Telecentric objective 30

3.12 Spherical and cylindrical lenses 31

3.13 Measured spectrum of the normalized transmission of the emission filters . 32

3.14 Diagram of the microscope optical setup 33

4.1 Intensity plot of the target image acquired with Olympus Plan N 20x objective 37

4.2 Intensity plot of the target image acquired with Olympus Plan N 20x objective with outliers removed 38

4.3 Target image with Olympus Plan N 20x objective with the histogram stretching enhancement 38

4.4 Width determination for the detection unit with Olympus Plan N 20x for the x-axis 40

4.5 Plot of the measured data with the Khosrofian and Garetz fit 43

4.6 Plot of the obtained beam radius as a function of the position with the respective beam waist fit for $M^2 = 2$ 44

4.7 Plot of the intensity data with the respective sigmoidal fit for the microscope with each objective. 47

4.8 Plot of the first derivative of the computed sigmoidal function and the half-maximum intensity of the microscope with each objective 48

4.9 Plot of the intensity data with the moving average filter 50

4.10 Plot of the measured IRF for each gate width 51

4.11 Plot of the obtained fluorescence decay from the acquired IRF and fluorescence data of each sample 53

5.1 Diagram of the human eye 56

5.2 Diagram of the human cornea structures 56

5.3 Fluorescence intensity image of the epithelium using the Olympus Plan N 20x 58

5.4 Fluorescence intensity image of the epithelium using the Olympus Plan N 40x 58

5.5 Fluorescence intensity image of the endothelium using the Olympus Plan N 20x 59

5.6 Fluorescence intensity image of the endothelium using the Olympus Plan N 40x 59

5.7 Fluorescence intensity image of the border of the cornea using the Olympus Plan N 20x 61

5.8 Fluorescence lifetime image of figure 5.5 merged with intensity image . . . 62

5.9 Fluorescence lifetime image of figure 5.7a merged with intensity image . . . 63

5.10 Fluorescence lifetime image of figure 5.7b merged with intensity image . . . 64

A.1 Intensity plot of the target image acquired with Olympus Plan N 40x objective 89

A.2 Intensity plot of the target image acquired with Olympus Plan N 40x objective with outliers removed 90

A.3 Acquired target image with Olympus Plan N 40x objective with the histogram stretching enhancement and outliers removed 90

A.4 Width determination for the microscope detection unit 91

A.5 Plot of the measured data with the Khosrofian and Garetz fit at different positions across the beam propagation 92

A.6 Plot of the obtained beam radius as a function of the position with the respective beam waist fit for different values of M^2 93

B.1 Fluorescence decay and bi-exponential fit of the epithelium images acquired with Olympus Plan N 20x 95

B.2 Fluorescence decay and bi-exponential fit of the epithelium images acquired with Olympus Plan N 40x 96

B.3 Fluorescence decay and bi-exponential fit of the endothelium images acquired with Olympus Plan N 20x 96

B.4 Fluorescence decay and bi-exponential fit of the endothelium images acquired with Olympus Plan N 20x 97

C.1 Accuracy and precision errors of the decay parameters for 1.05 cnts/e^- and laser power set to 80% as a function of the Δt 100

C.2 Accuracy and precision errors of the decay parameters for 1.05 cnts/e^- and laser power set to 90% as a function of the Δt 101

C.3 Accuracy and precision errors of the decay parameters for 1.05 cnts/e^- and laser power set to 100% as a function of the Δt 102

C.4 Accuracy and precision errors of the decay parameters for 2.41 cnts/e^- and laser power set to 80% as a function of the Δt 103

C.5 Accuracy and precision errors of the decay parameters for 2.41 cnts/e^- and laser power set to 90% as a function of the Δt 104

C.6 Accuracy and precision errors of the decay parameters for 2.41 cnts/e^- and laser power set to 100% as a function of the Δt 105

C.7 Accuracy and precision errors of the decay parameters for 5.2 cnts/e^- and laser power set to 80% as a function of the Δt 106

C.8 Accuracy and precision errors of the decay parameters for 5.2 cnts/e^- and laser power set to 90% as a function of the Δt 107

C.9 Accuracy and precision errors of the decay parameters for 5.2 cnts/e^- and laser power set to 100% as a function of the Δt 108

C.10 Accuracy and precision errors of the decay parameters for 1.05 cnts/e^- and laser power set to 90% as a function of τ_1 and τ_2 109

C.11 Accuracy and precision errors of the decay parameters for 2.41 cnts/e^- and laser power set to 90% as a function of τ_1 and τ_2 110

C.12 Accuracy and precision errors of the decay parameters for 1.05 cnts/e^- and laser power set to 90% as a function of the α_1 111

C.13 Accuracy and precision errors of the decay parameters for 2.41 cnts/e^- and laser power set to 90% as a function of the α_1 112

List of Tables

1.1 Nonfunctional requirements of the system. 3

3.1 MCP gain for different applied voltages 27

3.2 Specifications of the Imager Compact CCD 27

3.3 Specifications of infinity-corrected microscope objectives 29

3.4 Specifications of the LSM04-BB telecentric objective 31

3.5 Specifications of the lenses used on the microscope 31

4.1 Angles of the target relative to the x-axis and y-axis of the acquired image 39

4.2 Obtained widths in number of pixels of one line for the x-axis and y-axis of the detection unit 40

4.3 Obtained FOV for the detection unit with each objective 41

4.4 Obtained beam radius with a 95% confidence level for different positions along beam propagation 43

4.5 Coefficients of the sigmoidal equation used to fit the plot of intensity . . . 47

4.6 Lateral resolution for the x-axis and the y-axis of the detection unit with each objective 50

4.7 Results of the samples measured lifetimes with the respective χ^2 and the relative error with the reference value 52

5.1 Comparison of the pig and human corneal structures thicknesses 57

5.2 Measured fluorescence lifetimes of epithelium and endothelium for each objectives 60

5.3 Measured fluorescence lifetimes of images 5.7a and 5.7b acquired with Olympus Plan N 20x objective 61

6.1 Gain and excess noise used in the simulations as a function of the MCP voltage. 69

Acronyms

ADC Analog-to-Digital Converter

CCD Charge-Coupled Device

CFD Constant Fraction Discriminator

DSLM Digital Scanned Light-Sheet Microscopy

FAD Flavin Adenine Dinucleotide

FLIM Fluorescence Lifetime Imaging Microscopy

FOV Field Of View

FRET Förster Resonance Energy Transfer

FWHM Full Width at Half Maximum

GOI Gated Optical Intensifier

HRI High Rate Imager

IRF Instrument Response Function

LSFM Light-sheet Fluorescence Microscopy

MCP Micro Channel Plate

NAD(P)H Nicotinamide Adenine Dinucleotide

PCI Peripheral Component Interconnect

RLD Rapid Lifetime Determination

SPIM Selective Plane Illumination Microscopy

TAC Time-to-Amplitude Converter

TCSPC Time-Correlated Single Photon Counting

TDC Time to Digital Converter

Chapter 1

Introduction

1.1 Objectives 2

1.2 Context and motivation 2

1.3 Requirements analysis 3

1.4 Thesis content 3

1.1 Objectives

The objectives of this work are the design and implementation of a Time-Gated fluorescence lifetime microscope with light-sheet illumination to image thick biological tissues such as corneas. Therefore, it was necessary to divide the work into two phases. The first phase consists of the design and implementation of the microscope setup. The second phase is the test and characterization of the microscope, to evaluate the quality of the images and the lifetime determination.

Due to a malfunction in the PC computer that controls the gated-intensified camera used in this project, and because this malfunction prevented the use of the camera for a period of almost 3 months, it was proposed an additional task. This supplementary objective consists of the accuracy and precision evaluation of the Rapid Lifetime Determination (RLD) algorithm for simulated data for fluorescence emission for the metabolic co-factor Flavin Adenine Dinucleotide (FAD), in conditions similar to the implemented microscope.

1.2 Context and motivation

This work results from research studies done in the Instrumentation Group of the Coimbra Institute for Biomedical Imaging and Translational Research (CIBIT). One of the main objectives of this group is the research and development of optical imaging methods to image and evaluate the metabolism of biological tissues, specifically ocular tissues.

The cornea is the transparent tissue at the front of the eye. It is a highly differentiated tissue to allow refraction and transmission of light, with specialized characteristics to maintain transparency and resist external adverse factors like dehydration, microbial invasion, and trauma. It is a convex-concave lens with an average refractive power of 43 diopters (about 70% of the total refractive power of the eye) [1]. Corneal pathologies cause pain, affect vision, and can lead to blindness. These pathologies are the second cause of blindness in the world [2]. Therefore, a non-invasive method of early diagnosis to identify anomalies and prevent progression of pathologies to irreversible states, has the potential of being of clinical interest. Current, clinical methods of corneal imaging are mainly structural imaging methods. This is a disadvantage, as the corneal dysfunctions must already have enough progression to produce observable structural alterations. It is necessary a functional imaging method capable of identifying cellular abnormalities at an early stage of the pathology progression. Fluorescence lifetime imaging microscopy may

be able to satisfy this need.

This work followed a previous project where a wide-field Time-Gated fluorescence lifetime microscope with structured illumination was developed. The obtained images with the previous system have little contrast due to the lack of adequate optical sectioning. The microscopy with light-sheet illumination allows excitation only in a thin axial plan. Thereby, it is reasonable to expect that the acquired images will have higher contrast and better optical sectioning compared to structured illumination.

The project was constrained by the lack of funds for acquiring expensive optical and optomechanical components, namely microscope objectives and precision translation stages. The work developed was entirely based on equipment and components already available the laboratories of the research group.

1.3 Requirements analysis

The requirements analysis shows the requirements the system must satisfy. The functional requirement of the system is to produce fluorescence lifetime images in thick biological tissues with thickness lower than 500 μm using an excitation wavelength of 440 nm. The nonfunctional requirements, shown in table 1.1, are related to the performance of the system.

Table 1.1: Nonfunctional requirements of the system.

Parameter	Value
Optical sectioning	10 - 15 μm
Timing resolution	300 - 400 ps
Lateral resolution	20 μm
Field of view	200 x 300 μm^2
Accuracy and precision error	$< 10\%$

1.4 Thesis content

This document is organized into seventh chapters. The first chapter contains the objectives and context of this work. It includes the motivation for doing this project and the requirements the system must fulfill.

The second chapter presents the principles of fluorescence lifetime imaging microscopy (FLIM) and the state of the art concerning this project. The physics of the fluorescence process is explained and related to FLIM technique. The basis and advantages of fluorescence lifetime microscopy and the design considerations are described. The FLIM acquisition techniques are presented, with focus on the time domain methods. This chapter also presents the principle of light-sheet fluorescence microscopy, its developments over the years, and its applications. The algorithms for fluorescence lifetime determination used in this work (Rapid Lifetime Determination and FLIMfit software) are also presented in this chapter.

In the third chapter, the implementation of the microscope is presented. The microscope implementation contains the characteristics and functions of each system and optical component, and a detailed description of the final setup of the microscope.

The evaluation of the microscope performance is shown in the fourth chapter. Here are described the methods used to determine each parameter. The parameters include optical and timing parameters.

In the fifth chapter, are presented the results of imaging trials done with animal corneas.

The sixth chapter is dedicated to the evaluation of the accuracy and precision of the Rapid Lifetime Determination (RLD) algorithm. This evaluation concerns the measurement of FAD decays with the developed Time-Gated microscope.

The seventh chapter includes the conclusions of this work, the general discussion of the results, and a presentation of the future work.

Chapter 2

Fluorescence lifetime imaging microscopy principles and state of the art

2.1 Fluorescence process 6

2.2 Fluorescence Lifetime Imaging Microscopy 8

2.3 FLIM acquisition techniques 9

2.4 Image formation techniques 12

2.5 Light-Sheet Fluorescence Microscopy 13

2.6 Fluorescence lifetime determination 16

2.1 Fluorescence process

Fluorescence Lifetime Imaging Microscopy (FLIM) is a microscopy technique based on a radiative decay process named fluorescence. This microscopy modality reveals the spatial distribution of the fluorescence lifetimes of fluorophores contained in a sample [3]. FLIM produces images in which the contrast is given by the molecules fluorescence lifetimes. These resulting images allow not only distinguishing the different structures but also retrieve information on the fluorophore microenvironment or functional information on the sample.

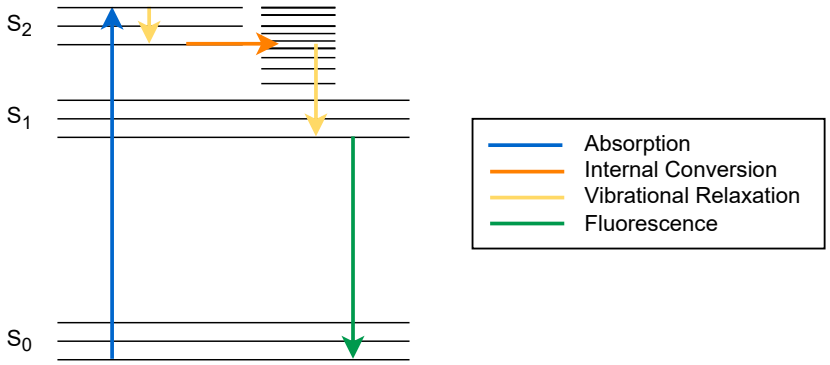

Figure 2.1: Diagram of the fluorescence process adapted from [4]. The fluorophore absorbs one photon and goes to an excited state. Next, occurs internal conversion and vibrational relaxation. When the molecule returns to the ground state S_0, there is emission of light.

The fluorescence process occurs in fluorophores, which are molecules with fluorescent properties. This process is pictured in figure 2.1 through an adaptation of the Jablonski diagram. When fluorophores absorb light, their electrons are excited from the ground state (S_0) to an excited singlet state. The fluorophore goes to the first (S_1) or second (S_2) excited singlet state depending on the energy $E = \frac{hc}{\lambda}$ of the absorbed photon (where h is Planck constant, c is the speed of light and λ is the wavelength). The electron from the most external layer, which is now in an excited singlet state, is still paired to the second electron in the ground state. Next, internal conversion (from a higher to a lower state) and vibrational relaxation (to a lower vibrational level within the same electronic state) occur to the lowest vibrational level of the first excited singlet state S_1. Fluorescence happens when the excited molecule returns to the ground singlet state S_0 and occurs emission of photons [4–6].

The emitted photons have lower energy than the absorbed ones due to losses during the return to the ground state, such as internal conversion and vibrational relaxation. The

difference between the excitation and emission energies is named Stokes shift [4–6].

Fluorescence lifetime (τ) is the average time the fluorophore stays excited before returning to the ground state. This parameter is typically in the nanoseconds range and follows equation 2.1, where k_r is the radiative decay rate of the fluorophore and k_{nr} is the non-radiative rate [4–6].

$$\tau = \frac{1}{k_r + k_{nr}} \tag{2.1}$$

The ratio between the number of emitted photons and the number of absorbed photons is the fluorescence quantum yield (Φ_F) [5, 6]. This parameter demonstrates the efficiency of the fluorescence process and is defined by equation 2.2.

$$\Phi_F = \frac{k_r}{k_r + k_{nr}} \tag{2.2}$$

During the fluorescence process, the initial number of excited fluorophores decreases with time due to radiative and non-radiative decay processes. The number $n(t)$ of fluorophores in excited state at time t after the excitation pulse is given by equation 2.3 [6, 7].

$$dn(t) = -(k_r + k_{nr})n(t)dt \tag{2.3}$$

The fluorescence intensity results from emitted photons and has an exponential decay behavior resulting from the integration of equation 2.3. Fluorescence intensity $I(t)$ is defined by equation 2.4, where I_0 corresponds to the number of excited fluorophores at $t = 0$ after the excitation pulse [8].

$$I(t) = I_0 \exp\left[-\frac{t}{\tau}\right] \tag{2.4}$$

When the sample has different non-interacting fluorophores, the fluorescence intensity is given by the summation of the fluorescence decay of the several fluorophores with different lifetimes and intensities in t=0. Thus, the fluorescence intensity decay is multi-exponential and is represented by equation 2.5 [6, 9].

$$I(t) = \sum_{i=1}^{N} I_i \exp\left[-\frac{t}{\tau_i}\right] \tag{2.5}$$

2.2 Fluorescence Lifetime Imaging Microscopy

FLIM systems are designed around the fluorescence process. As seen in section 2.1, fluorophores can emit fluorescence photons following light absorption. Therefore, FLIM systems include an illumination component responsible for exciting the fluorophores in the sample [10]. The light source in the illumination component needs to have the required energy to excite the fluorophores under study [4]. Moreover, since different species of fluorophores have distinct excitation and emission spectra, the light source has to be chosen accordingly [5, 11]. The fluorescence lifetimes typically are in the nanosecond range [3]. Therefore, for time domain systems, the excitation light pulses must be shorter in duration to prevent the overlapping of fluorescence signals [3,12]. FLIM systems include a detection component to capture the emitted fluorescence photons [10]. The emitted light is filtered before being detected by the sensor, therefore the generated images result exclusively from the fluorescence photons [4].

The FLIM data is processed and analyzed to estimate the fluorescence lifetime of fluorophores [13]. These estimations allow computing the fluorescence lifetime map of the sample, the goal of the FLIM technique. From these images, FLIM allows to know the position of fluorophores and the composition of the sample since different fluorophores have a characteristic lifetime [9]. This technique is typically used in biological imaging as it provides structural and functional information about the specimen under study [3,11,14].

The FLIM technique is more advantageous than the intensity-based fluorescence microscopy because is independent of fluorophore concentration and intensity-based artifacts. Some of these artifacts are induced by the excitation light intensity, the detection gain and photobleaching (destruction of the fluorescence capability due to light excitation). Furthermore, intensity-based fluorescence microscopy cannot distinguish fluorophores with similar excitation and emission spectra [13, 15, 16]. The lifetime measurements are absolute and are not affected by nonuniform illumination. Thus, these measurements are reproducible and comparable despite the different microscopes instrumentation [16].

There are different FLIM microscopes configurations, which differ in illumination, detection mechanism and acquisition techniques [15]. These microscopes are typically custom-built because are developed for a specific application, regarding the sample under study [3]. The illumination and detection mechanism defines the image formation technique and the acquisition techniques characterize the process of fluorescence signal measurement [8,15].

There are also different analytical methods for fitting the decay curve and estimate the fluorescence lifetime of the sample through FLIM data [13, 15].

2.3 FLIM acquisition techniques

Fluorescence data can be acquired using two methods: in the frequency domain or in the time domain. The differences between these methods are related to the excitation and detection techniques [11].

In the frequency domain method, the sample is typically excited with a sinusoidally modulated light source. Albeit the emitted fluorescence signal has the same frequency as the excitation light, it has shifted phase and a decreased modulation depth. The fluorescence lifetime is determined by these phase shift and relative modulation depth [3, 12, 17].

In the time domain method, the sample is excited with a pulse of light shorter than the fluorophore fluorescence lifetime. The intensity distribution of the detected fluorescence photons generates the decay curve of the fluorophores. This decay curve is used to estimate the fluorescence lifetime [11, 12]. The Time-Correlated Single Photon Counting (TCSPC) and Time-Gated techniques are based on the time-domain method [3, 6, 15].

2.3.1 Time-Correlated Single Photon Counting technique

The principle of operation of the TCSPC technique is the measurement of the arrival time of the first detected photon after each excitation pulse. The light pulses must have a certain repetition rate to ensure that the cycles of excitation and emission do not overlap. The measurements of the arrival times of the first emitted photon in each cycle are accumulated until creating a histogram of the arrival times of the first photon. The resulting histogram represents the fluorescence decay curve of the sample. This curve represents the number of detected emitted photons versus time after the excitation pulse [3, 6, 17].

The fluorescence photon is collected by photodetectors. Commonly, the used detectors in this application are the Photomultiplier Tube, the Micro Channel Plate (MCP) and the Single Photon Avalanche Diode [18]. A TCSPC system requires two photodetectors, one for detecting the excitation pulse and the other for detecting the fluorescence photon.

Each photodetector is coupled to a Constant Fraction Discriminator (CFD). The CFDs marks with precision and consistency the arrival times of pulses from the photodetector. The output signals of the CFDs are used as Start and Stop pulses. These signals control a Time-to-Amplitude Converter (TAC). The TAC produces a voltage proportional to the time difference between the excitation and emission of the sample (Start and Stop signals). The signal is amplified and converted to digital in an Analog-to-Digital Converter (ADC) [17, 18]. For low illumination conditions, the histogram of the arrival times of the first detected fluorescence photon corresponds to the fluorescence decay profile of the sample. In practice, this requires an average value of detected photons per excitation cycle lower than 0.1 [17,18] or a more restrictive value of 0.02, according to some authors [19,20]. The working principle of the TCSPC technique is described in figure 2.2.

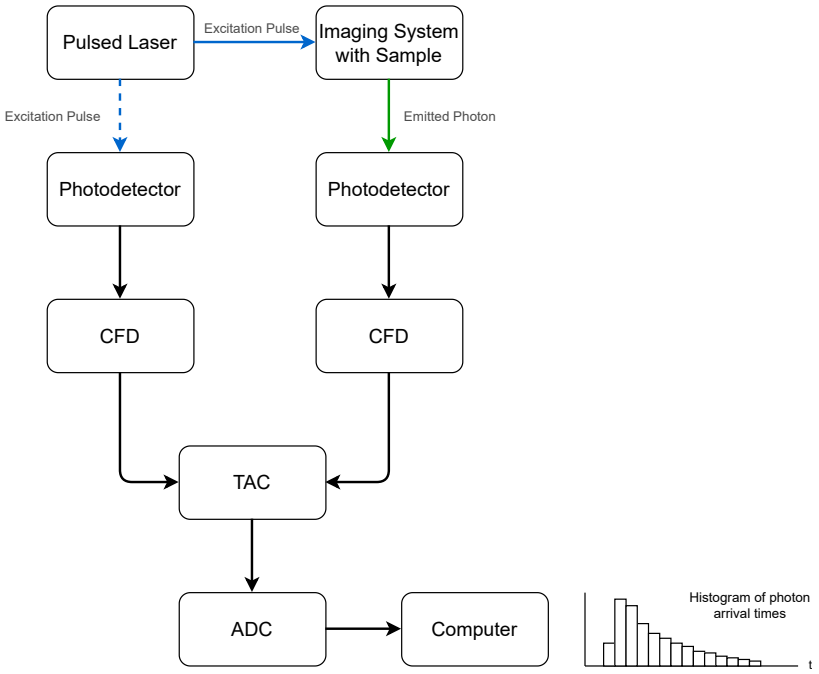

Figure 2.2: The General setup for a TCSPC FLIM acquisition system adapted from [8]. A pulsed laser is used to excite the sample. The emitted fluorescence photons and a fraction of the excitation pulse are detected by photodetectors and registered in CFDs. The TAC receives the two signals from CFDs. The TAC produces a voltage that increases with the time difference between the excitation and emission pulses. This voltage is converted to digital in an ADC and send to a computer to be processed. The process of excitation and detection is repeated and accumulated until obtaining the histogram of photon arrival times [8, 17, 18].

The more recent TCSPC systems only have one photodetector. The synchronization signal is obtained electrically through an impulse from the light source. This impulse is typically provided by the laser source or its controller. A second photodetector is used solely when the light source does not give an adequate synchronization signal [17, 18]. These systems also use a TDC (Time to Digital Converter), which have the same functions as the TAC

and the ADC [18].

2.3.2 Time-Gated technique

In the Time-Gated technique, the sample is excited by a pulse of light with a short duration. The acquisition of the fluorescence signal occurs in specific time intervals, named gates. The fluorescence decay curve of the sample is formed by the number of emitted photons detected in the gates plotted against time, as seen in figure 2.3 [6, 21].

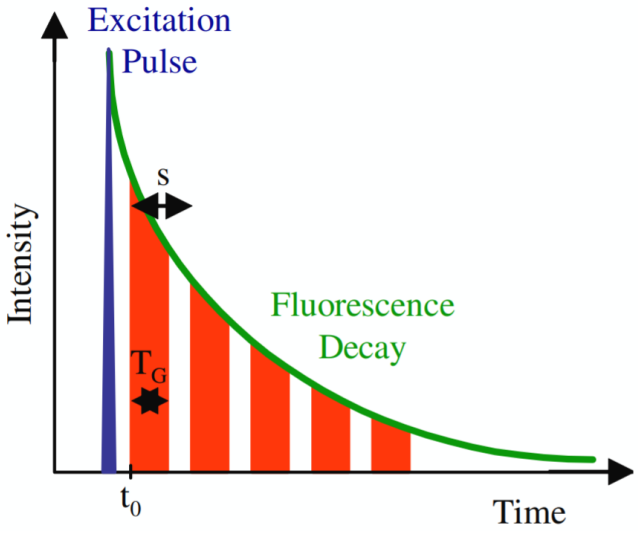

Figure 2.3: Diagram of the principle of Time-Gated FLIM. The detection of emitted photons by the sample occurs in successions of gates after the excitation pulse. The gate width is defined by T_G and the time between two consecutive gates is S [21].

The detection of the fluorescence signal requires a Gated Optical Intensifier (GOI), which allows the acquisition of photons in temporal gates and specific rates. This device comprises a photocathode, an MCP and a phosphor screen. The gating voltage pulse applied to the photocathode defines the gate width. This pulse determines when the acquisition of emitted photons occurs. These photons are converted to electrons in the photocathode. Next, they are amplified in the MCP according to the gain voltage applied. The multiplied electrons are reconverted into photons in the phosphor screen and detected in a Charge-Coupled Device (CCD) [21].

In the Time-Gated technique, similar to the TCSPC technique, the laser system generates a trigger pulse at the same instant as it outputs the excitation pulse. The trigger pulse starts the acquisition of the fluorescence signal. There are temporal delays between the excitation of the sample and the opening of the detector. The user controls these delays

through a delay generator. The trigger signal suffers a delay and is sent to the GOI to open the gates. A computer controls the system, also stores measured data and processes the fluorescence images [6, 8, 22]. Figure 2.4 summarizes the working principle of the Time-Gated technique.

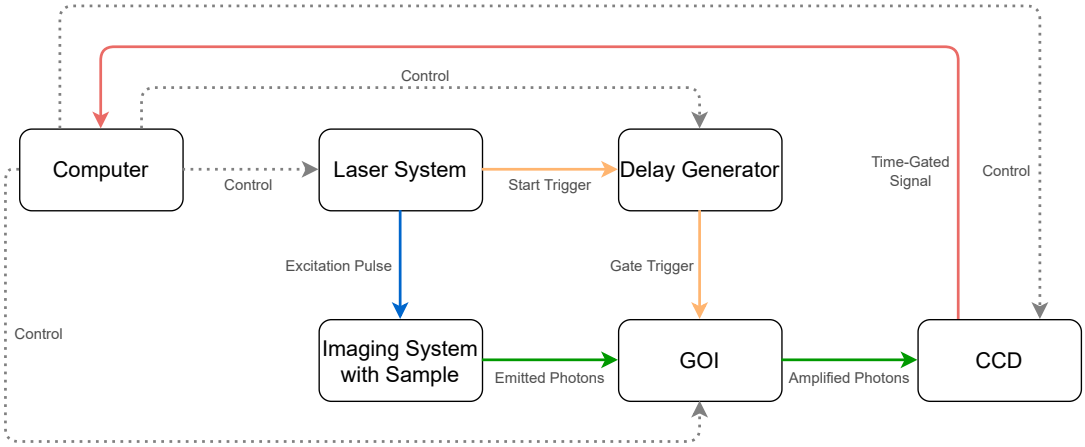

Figure 2.4: The General setup for a Time-Gated FLIM acquisition system adapted from [6]. The excitation pulse from the Laser System works as a Start Trigger signal. This signal suffers a delay in the Delay Generator, resulting in a Gate Trigger which is sent to GOI to start the acquisition. A computer controls and all the devices.

Time-Gated, when compared to TCSPC, has a lower electronic dead times and higher count rates due to the acquisition of fluorescence photons in successive gates after one excitation pulse, resulting in faster acquisition times. As seen in section 2.3.1, the TCSPC technique measures the arrival time of the first detected photon after each excitation pulse [13]. Due to system dead time, the photon count rate per excitation cycle must be low to not detect just the fluorescence photons with shorter arrival times [13, 18]. The detection of emitted photons is repeated several times until creating a histogram of the arrival times, leading to a longer acquisition time than the Time-Gated method. The Time-Gated technique has a lower time resolution than the TCSPC. The decrease in time resolution is a result of the possibility of undersampling the fluorescence signal due to gates [13].

2.4 Image formation techniques

There are two configurations to produce FLIM images with one-photon excitation: wide-field and confocal microscopy [10]. They have different illumination and detection strategies. In wide-field microscopy, the entire sample is illuminated simultaneously. Therefore,

no scanning mechanism is required to produce a FLIM image. Conceptually in this configuration, the illumination and detection occur in the focal plane of the objective lens. But in reality, the acquired fluorescence signal also comes from the out-of-focus regions, worsening the spacial resolution. Wide-field microscopy can generate images rapidly because the fluorescence photons from all pixels are collected simultaneously. Also, as this microscopy technique does not require scanning, its implementation is relatively simple [3, 10, 13].

The concept of confocal microscopy is the acquisition of fluorescence photons from a single point at a time. After the excitation of the sample, the emitted photons are spatially filtered by a pinhole located in the image plane to reject the out-of-focus fluorescence. Therefore, confocal microscopy has higher contrast and spatial resolution than wide-field. In confocal microscopy, the process of acquisition is longer and the instrumentation more complex [3, 10, 13].

2.5 Light-Sheet Fluorescence Microscopy

Light-Sheet Fluorescence Microscopy (LSFM) is an imaging technique where the illumination of the sample is accomplished by a sheet of light with a small thickness to excite the fluorophores. The detection of emitted photons occurs orthogonally to the excitation beam. The illumination of the sample occurs in the focal plane of the detection objective lens. This configuration enables the excitation of just a well-defined slice, providing optical sectioning [23, 24]. Figure 2.5 illustrates the principle of LSFM.

The principal advantage of LSFM is the ability to obtain optical sectioning. Because solely a thin volume of sample is illuminated, there is no excitation of fluorophores outside this volume. Consequently, the acquired fluorescence data only includes signals from in-focus regions. The resulting image has optical sectioning and contrast [23–25].

Comparing with wide-field and confocal microscopy, which illuminate the whole sample, the LSFM only illuminates the plane of interest. This concept in LSFM decreases both the risk of photobleaching the sample and the acquisition time. Also, the LSFM has higher penetration depth than wide-field and confocal microscopy due to perpendicular excitation and detection [23–25].

The light-sheet can be static or virtual. A static light-sheet is generated with cylindrical lenses and a virtual light-sheet is achieved with a rapid scanning system that moves the

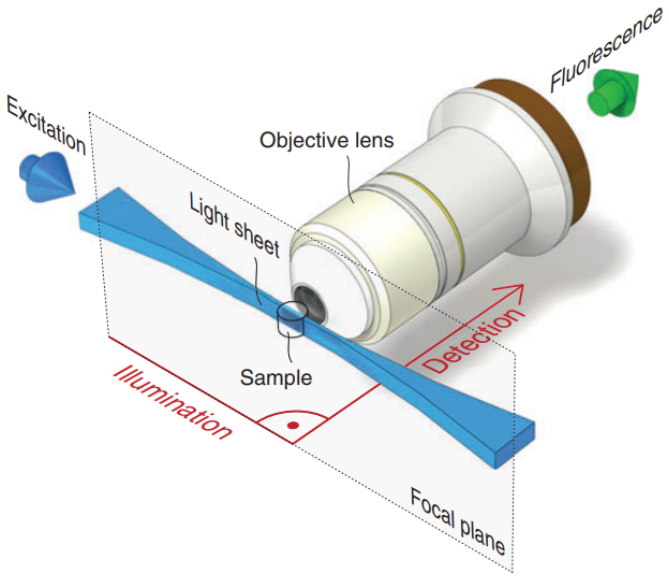

Figure 2.5: In LSFM, the illumination takes place perpendicularly to the detection of emitted photons. As a result, a thin volume of the sample is excited in the focal plane of the detection [23].

light beam along the detection axis. The Selective Plane Illumination Microscopy (SPIM) and Digital Scanned Light-Sheet Microscopy (DSLM) are two LSFM techniques, which use a static and virtual light-sheet, respectively [22, 24].

2.5.1 Developments in LSFM

Siedentopf and Zsigmondy [23, 26] described the first application of light-sheet in 1902. They generated the light-sheet with a projection of sunlight through a slit to observe gold particles. In 1993 the light-sheet was applied in fluorescence microscopy with a technique named Orthogonal-Plane Fluorescence Optical Sectioning. The implemented microscope imaged the cochlea structure through a light-sheet generated with a cylindrical lens. The acquired images had lateral and axial resolutions of 10 μm and 26 μm, respectively [27].

The development of LSFM techniques was boosted after the implementation of a Selective Plane Illumination Microscopy system in 2004 [28] [29]. This system was used to visualize the intern structure of medaka embryos. A cylindrical lens generated the light-sheet to excite the specimens. This system has an axial resolution better than 6 μm at a depth of 500 μm inside the embryo [28].

Currently, several LSFM techniques were implemented and improved to observe and measure specific samples. It is noteworthy that the improvements in LSFM are different for

each application [29]. However, there are only a few studies that merge LSFM with FLIM. Next, are presented three FLIM-LSFM systems implemented in 2011, 2018 and 2020.

The FLIM-SPIM system developed in 2011 [30] with frequency domain acquisition was used to observe Madin-Darby canine kidney cysts. The light-sheet was generated by a beam expander, two slits and a cylindrical lens. This system had a lateral full width at half maximum (FWHM) of 0.79 μm vertically and 0.82 μm horizontally.

In 2018, a FLIM-SPIM system [31] was implemented with time domain acquisition to image cleared mouse brains. A slit and a cylindrical lens generated a light-sheet. The lateral resolution of the microscope was 7.0 μm on the horizontal axis and 7.8 μm on the vertical axis. The axial resolution was 9.9 μm.

In 2020, a FLIM-DSLM system [22] was built with time domain acquisition to observe zebrafish embryos. The lateral and axial resolution was 6.4 μm and 23 μm, respectively, with the light-sheet produced by a scanning system.

2.5.2 Applications of FLIM-LSFM

The LSFM is used for biological imaging. Mostly, in the fields of developmental and cellular biology, anatomical studies, biophysics and neurosciences [32]. This microscopy can be used to observe and measure intact mesoscopic living samples. Therefore, LSFM is useful for the study of embryos and cells [23].

Combining the LSFM with FLIM allows distinguishing fluorophores with different lifetimes with similar spectral properties and mapping the lifetime of mesoscopic living samples. FLIM-LSFM microscopy is also advantageous to map protein-protein interactions by the Förster Resonance Energy Transfer (FRET) process [22,29]. This process is based on the energy transference between two molecules, the donor and acceptor. The FRET process allows the determination of the distance between these two molecules [33].

The FLIM-LSFM can provide favorable non-invasive functional information of biological processes in metabolism. This technique can be an advantageous imaging method. Therefore, it is necessary to invest in its development.

2.6 Fluorescence lifetime determination

Simply fitting exponentials to equations 2.4 and 2.5 is not an acceptable method to determine fluorescence lifetimes [6]. This method is not efficient to calculate the exponential decay parameters due to the prolonged processing time of a large number of data. [34]. Also, in time domain systems, the acquired data has artifacts that wrongly affect the results [6].

To accurately determine the fluorescence lifetimes of fluorophores in time domain acquisition techniques is necessary to measure the Instrument Response Function (IRF). This measurement is used to correct the distortions in data caused by the system IRF [35].

The utilization of algorithms allows calculating the actual fluorescence lifetimes of fluorophores in the sample more efficiently and accurately than a simple exponential fitting. The Rapid Lifetime Determination (RLD) and Rapid Global Fitting Method (FLIMfit software) algorithms are examples of algorithms used in time domain systems [6].

2.6.1 Instrument Response Function

The IRF is the system response to a an infinitely narrow pulse signal. The acquired fluorescence data corresponds to the convolution between the actual fluorescence data and the system IRF. To obtain the actual fluorescence data is required a deconvolution from the IRF. Then, it is necessary to measure the IRF to remove the distortions [6, 8].

There are two ways to determine the system IRF. Through the measurement of reference fluorophores with a short and known lifetime or the detection of the reflected or scattered excitation pulse [8, 35]. The deconvolution of IRF with the true decay data is usually achieved by iterative algorithms [6, 8].

2.6.2 FLIMfit software

FLIMfit is a tool to analyze and observe fluorescence lifetime data acquired with a time domain system. It allows fittings and global analysis of large datasets [36]. This software results from the Rapid Global Fitting Method, which is based on nonlinear least square fitting [6]. It offers different analyzing and fitting options, such as mono-exponential or multi-exponential decays. Other features include the histogram of the decay parameters

and the production of false-color maps of the sample.

The FLIMfit software accounts for limitations from the instrument and background measurements. Besides, it uses IRF measurements to deconvolute the acquired data. This software is helpful because takes into consideration the parameters that affect the estimation of fluorescence decay [6, 36].

2.6.3 Rapid Lifetime Determination

The Rapid Lifetime Determination (RLD) is an algorithm used to determine the fluorescence decay parameters described for the first time by Ashworth in 1983 [37]. The lifetimes and pre-exponential factors are estimated through integrations of the fluorescence decay data over several time intervals [38]. The curve is divided into areas, that results from photon intensity accumulation at equal time intervals [39]. In a Time-Gated system, these areas correspond to the gates during the acquisition and can be contiguous or overlapping [6, 38].

The fluorescence curve is divided into two areas (D_0 and D_1) with equal width for a mono-exponential decay, given by equation 2.6, where t is the time and $I(t)$ is the fluorescence intensity [39]. In a situation of contiguous gates, as seen in figure 2.6, the fluorescence lifetime (τ) and pre-exponential factor (k) are determined by equations 2.7 and 2.8 [39], respectively. These equations were applied by Ballew and Demas in 1989 [39].

$$I(t) = k \exp\left(-\frac{t}{\tau}\right) \tag{2.6}$$

$$\tau = \frac{-\Delta t}{\ln(D_1/D_0)} \tag{2.7}$$

$$k = \frac{D_0}{\tau(1 - D_1/D_0)} \tag{2.8}$$

If the decay is bi-exponential, equation 2.9, there are two fluorescence lifetimes (τ_1 and τ_2) and two pre-exponential factors (k_1 and k_2) to estimate. In this case, the fluorescence decay is divided into four areas: D_0, D_1, D_2 and D_3 [38]. Consequently, the determination of the parameters is more complex relatively to mono-exponential decay. The equations to determine the decay parameters can be used for contiguous or overlapping gates and

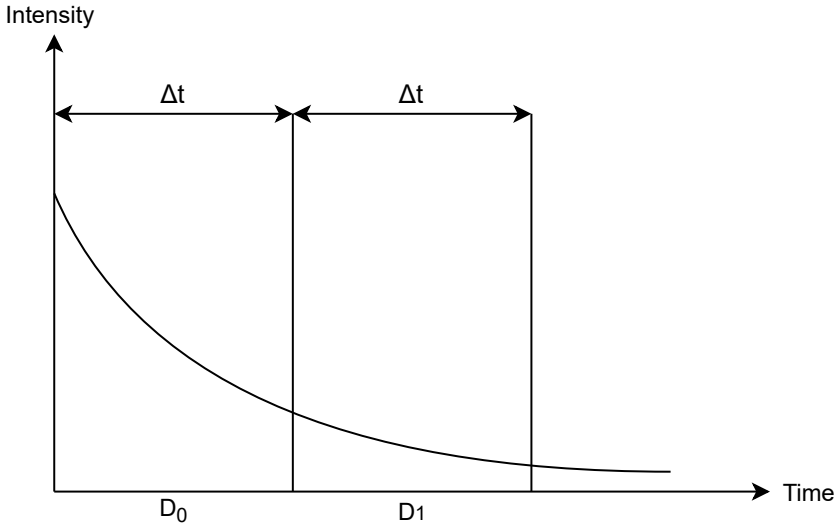

Figure 2.6: Graphic of the contiguous areas D_0 and D_1 for a mono-exponential decay adapted from [38]. The time between the same points of two consecutive gates is Δt.

were published in 2009 by Chang [15]. Figure 2.7 shows the graphic of a bi-exponential decay with the four areas, where g is the gate width and Δt is the time interval between the same points of two consecutive gates. In overlapping gates, Δt is smaller than the gate width. The parameters are estimated through equations 2.10, 2.11, 2.12 and 2.13, and intermediate calculations are required (2.14, 2.15, 2.16, 2.17, 2.18, 2.19) [15].

$$I(t) = k_1 \exp\left(-\frac{t}{\tau_1}\right) + k_2 \exp\left(-\frac{t}{\tau_2}\right) \tag{2.9}$$

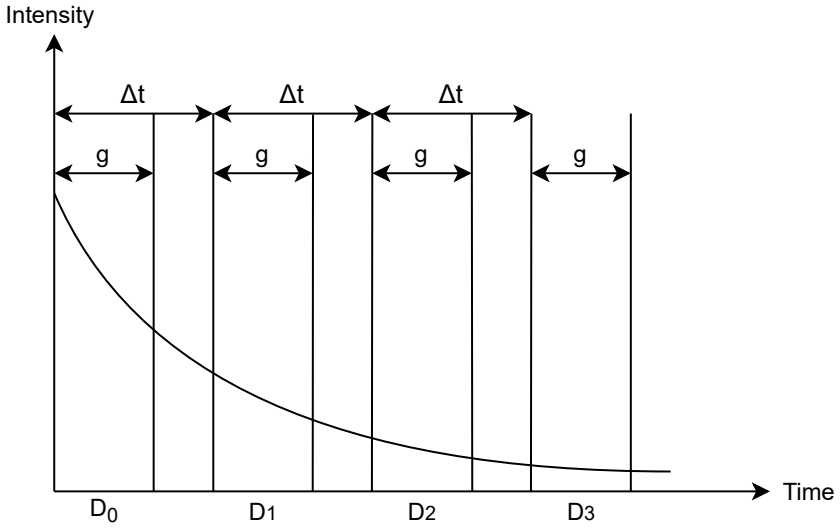

Figure 2.7: Graphic of the four integrated areas in a bi-exponential decay adapted from [15]. The gate with is g and Δt is the time between the same points of two consecutive gates.

$$\tau_1 = \frac{-\Delta t}{\ln y} \tag{2.10}$$

$$\tau_2 = \frac{-\Delta t}{\ln x} \tag{2.11}$$

$$k_1 = \frac{-\left(xD_0 - D_1\right)^2 \ln(y)}{\Delta t \left(x^2 D_0 - 2xD_1 + D_2\right)\left[1 - \left(\frac{xD_1 - D_2}{xD_0 - D_1}\right)^{\frac{g}{\Delta t}}\right]} \tag{2.12}$$

$$k_2 = \frac{-R \ln(x)}{\Delta t \left(x^2 D_0 - 2xD_1 + D_2\right)\left[x^{\frac{g}{\Delta t}} - 1\right]} \tag{2.13}$$

$$R = D_1 D_1 - D_2 D_0 \tag{2.14}$$

$$P = D_3 D_0 - D_2 D_1 \tag{2.15}$$

$$Q = D_2 D_2 - D_3 D_1 \tag{2.16}$$

$$DISC = P^2 - 4RQ \tag{2.17}$$

$$x = \frac{-P - \sqrt{DISC}}{2R} \tag{2.18}$$

$$y = \frac{-P + \sqrt{DISC}}{2R} \tag{2.19}$$

Chapter 3

Microscope implementation

3.1 System components 22

3.2 Optical components 28

3.3 Microscope setup 32

3.1 System components

The system developed in this work aims to image biological tissues with a thickness inferior to 500 μm, in this case, eye corneas. The implemented system is a fluorescence lifetime microscope with a Time-Gated acquisition method. The sample is illuminated through a static light-sheet and the emitted fluorescence photons are detected perpendicularly. This mechanism of illumination and detection derives from the functional principle of LSFM. The obtained images must have contrast and optical sectioning.

The objective is to image corneas through the fluorophore Flavin Adenine Dinucleotide (FAD). The cornea cells contain these molecules, which are involved with several enzymatic reactions in metabolism. The fluorescence lifetimes and intensities of FAD give information about the metabolic state of the cells. Any changes in these parameters could be a result of complications in cell biology, such as the presence of cancer cells [6, 40]. The excitation of FAD occurs between 420 and 500 nm and the emission between 520 and 570 nm [41]. Therefore, it is necessary to consider the excitation and emission spectrum of the fluorophore under study when designing the microscope.

The excitation light beam has a center wavelength of 440 nm. The laser has a controller that sends a trigger signal to a delay generator every time a pulse occurs. The resulting fluorescence signal is acquired in a GOI-High Rate Imager. A High Rate Imager (HRI) is a high repetition rate (order of MHz) GOI, with gate widths wider than 200 ps [42]. An HRI Control Unit controls the HRI and receives the signals from the delay generator. A CCD collects the photons from HRI for later processing and analysis in a computer. The devices of the system are controlled by software. The acquired data are analyzed with the FLIMfit software [36]. The complete setup of the Time-Gated fluorescence lifetime microscope with light-sheet illumination is presented in the diagram of figure 3.1.

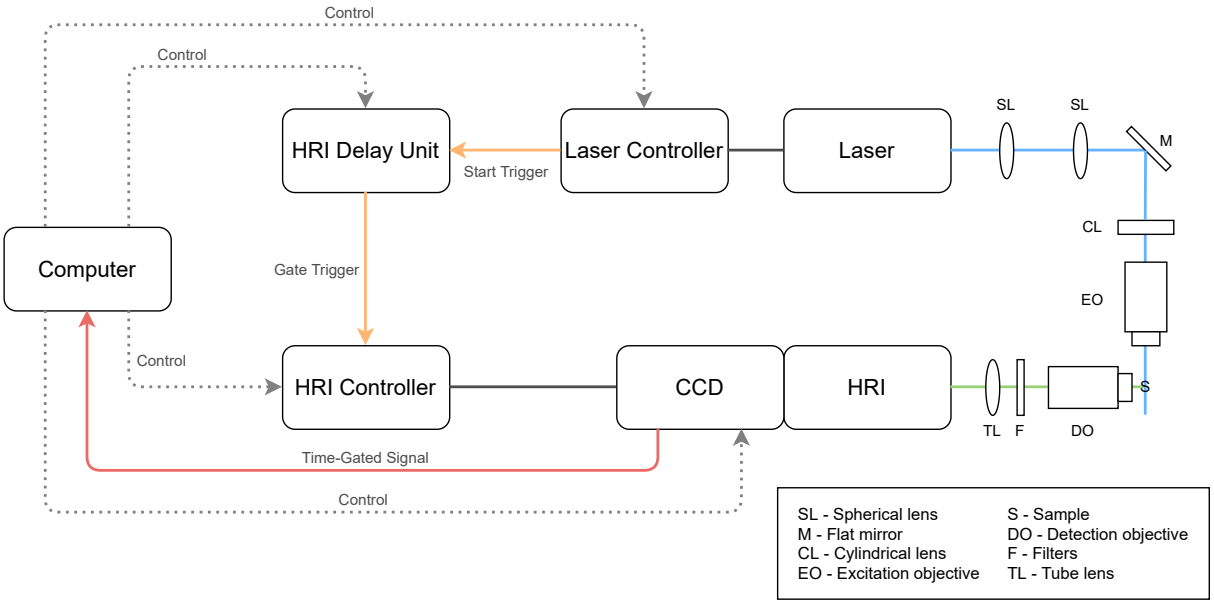

Figure 3.1: Diagram of the implemented Time-Gated fluorescence lifetime microscope with a light-sheet illumination. The laser controller generates a start trigger to the HRI delay unit when the light pulse occurs. The HRI delay unit sends a gate trigger to the HRI controller, which controls the CCD/HRI. The computer controls all the devices of the system and reads the acquired data. The optical setup for the light-sheet production and fluorescence photons detection is also depicted in the diagram.

3.1.1 Light source

The microscope uses a pulsed diode laser (LDH-P-C-440M, PicoQuant, Berlin, Germany) with a central wavelength of 440 nm as a light source (figure 3.2). A multichannel picosecond diode laser driver (PDL 828 "Sepia II") (figure 3.3) controls the laser. The laser driver sends a trigger signal to the delay generator. This trigger occurs simultaneously with each laser pulse and is responsible for the synchronization of the system. The laser has a maximum repetition rate of 40 MHz and a maximum average power of 22.5 mW. The minimum and maximum pulse FWHM of the laser are 63 ps and 190 ps, respectively [6]. The repetition rate and the laser power are parameters adjustable through the computer interface of the laser driver, via USB [43].

The diode laser beam has an elliptical shape with dimensions 1.5 × 3.5 mm (figure 3.4) [44]. These values were measured using a Ophir Photonics Spiricon SP620U beam profiling camera. This diode laser has a fast and a slow axis that corresponds to a higher and a lower value of divergence, respectively [45]. The typical divergence values is 0.11 mrad on the parallel plane and 0.32 mrad on the perpendicular plane relative to the beam [44].

The optical focal length of the beam is 4.5 mm [44].

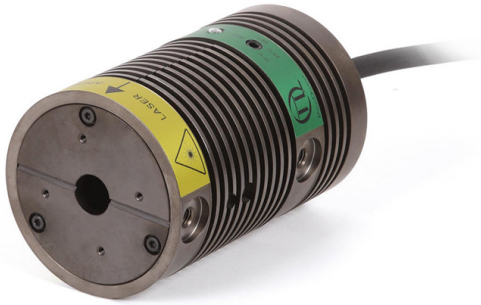

Figure 3.2: LDH-P-C-440M pulsed diode laser from PicoQuant [44].

Figure 3.3: PDL 828 "Sepia II" multichannel picosecond diode laser driver from PicoQuant [43].

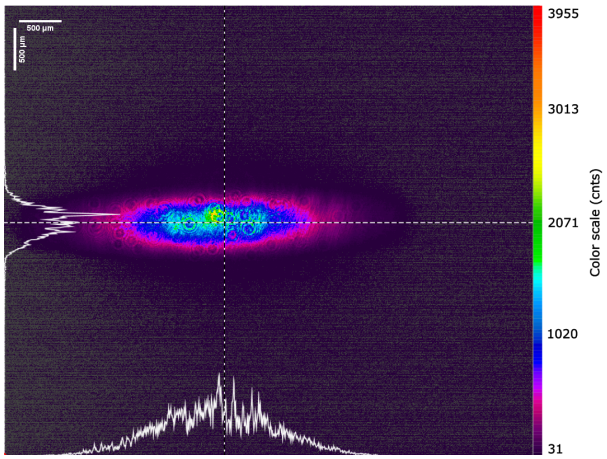

Figure 3.4: Image of the elliptical shape of the diode laser acquired through a Spiricon SP620U beam profiling camera from Ophir Photonics.

3.1.2 HRI delay unit

The HRI delay unit from LaVision (LaVision GmbH, Göttingen, Germany), shown in figure 3.5, receives the trigger signal from the laser controller when the excitation pulse occurs. The repetition rates of these trigger signals must be in the range of 20 to 80 MHz. This unit is responsible for generating a delayed trigger signal that is sent to the HRI to start the acquisition. It has a delay range of 0 to 50 ns and a resolution of 1 ps. A user computer controls the HRI delay unit through an RS232 interface [6, 46].

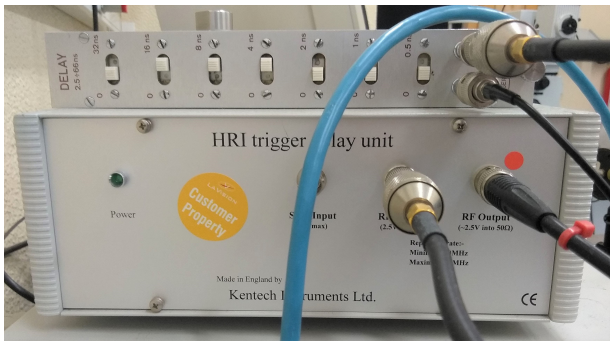

Figure 3.5: The HRI trigger delay unit from LaVision generates a delayed trigger signal, which commands the opening of the intensifier gates.

3.1.3 High Rate Imager (HRI)

An HRI is responsible for the acquisition of the fluorescence photons in temporal gates. The HRI of the implemented system is a Picostar HR from LaVision (LaVision GmbH, Göttingen, Germany) and has an HRI controller module, shown in figure 3.6. The computer also controls this unit through an RS232 interface. The HRI is a high repetition rate GOI comprised of an S25 photocathode, an MCP and a P43 phosphor screen . The phosphor screen has efficiency around 90% with emission in the region of green. The quantum efficiency curve of the HRI photocathode is shown in figure 3.7 [46].

(a) **(b)**

Figure 3.6: The HRI (figure 3.6a) and its controller module (figure 3.6b) from LaVision.

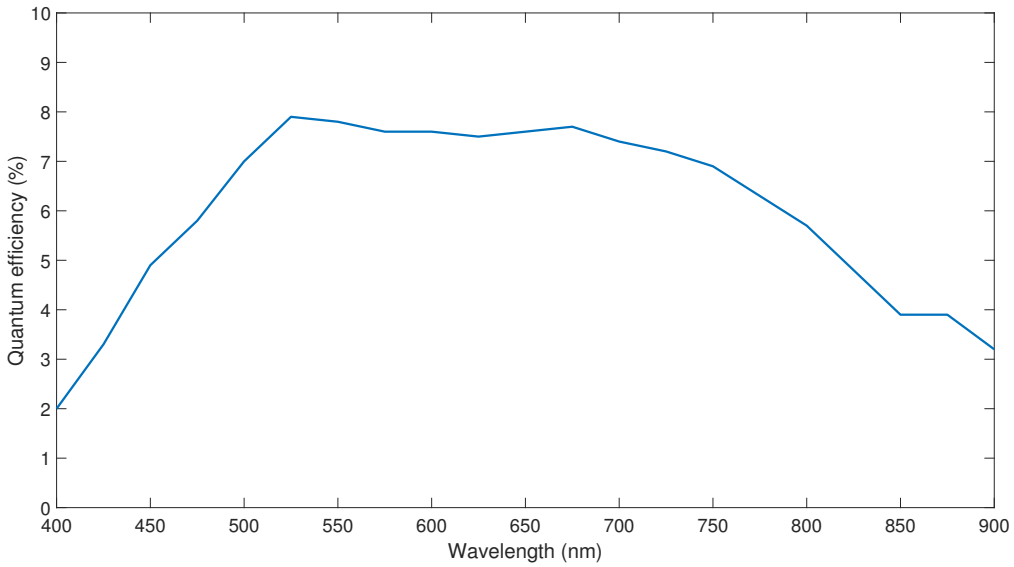

Figure 3.7: Quantum efficiency versus wavelength of the photocathode of the HRI. Data from [46].

The COMB was the chosen working mode of the HRI due to the pre-programmed gate width feature. Another characteristic of the HRI is the capability of defining the gain of the MCP. The gain voltage applied to the MCP defines the average number of counts detected by the CCD per electron arriving at the MCP, as presented in table 3.1 [6, 46].

Table 3.1: MCP gain (counts per electron) for different applied voltages [46].

UMCP (V)	Gain (cnts/e^-)
260	0.01
300	0.02
350	0.06
400	0.17
450	0.43
500	1.05
550	2.41
600	5.2
650	11.1
700	21.6
750	45
800	83
850	140

3.1.4 CCD

The CCD is an LaVision Imager Compact. It is connected to the HRI, and collects the incident photons and generates the corresponding electrical signal. This VGA camera communicates with the PC through a Peripheral Component Interconnect (PCI) board [46]. Table 3.2 presents the specifications of the CCD and figure 3.8 represents the quantum efficiency of the VGA sensor.

Table 3.2: Specifications of the Imager Compact CCD from LaVision [46].

CCD specifications	
Number of pixel	640 (H) x 480 (V)
Pixel size	9.9 μm x 9.9 μm
Scan area	6.3 mm x 4.8 mm
Digitization	12 bits
Spectral range bandwidth	280 - 1000 nm

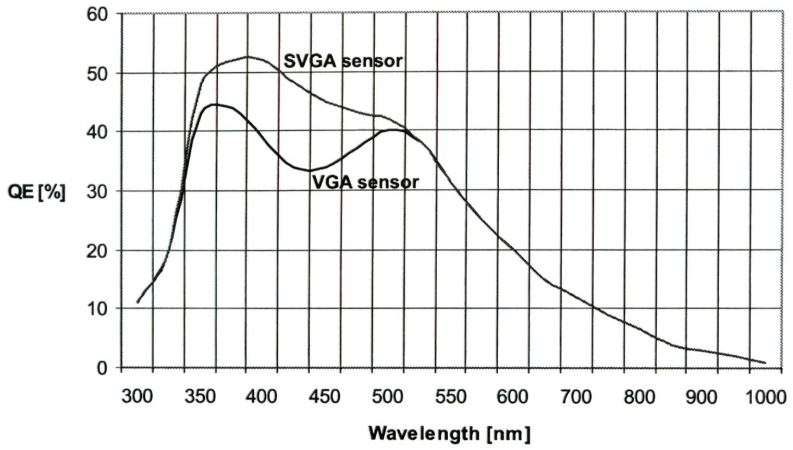

Figure 3.8: Quantum efficiency versus wavelength of the VGA sensor of the CCD camera [46].

3.1.5 DaVis software

The DaVis software controls the system devices and displays the live images and decay profiles. These devices are the HRI delay unit, the HRI and the respective controller module and the CCD. After establishing a connection with the devices, this software allows the user to configure the system and start the acquisition. The user can define the CCD exposure time with a minimum of 20 ms, the gate widths of the HRI and the voltage gain of the MCP. Relatively to the HRI delay unit, the user can define the delay and the temporal increments. These parameters specify when the acquisition will occur.

3.2 Optical components

The principle of the implemented microscope is the excitation of the sample through light-sheet illumination and orthogonal detection of the fluorescence photons. Therefore, the microscope has two optical units: one for excitation of fluorophores and the other for detection of fluorescence photons. Both units contain several optical components with specific characteristics. The excitation unit requires lenses for creating the light-sheet illumination from the elliptical laser beam [47]. The detection unit includes a microscope objective, filters and lenses for fluorescence light collection [6].

3.2.1 Infinity-corrected microscope objective

The microscope uses infinity-corrected microscope objectives for light collection: the Olympus Plan N 20x and Olympus Plan N 40x objective lenses, shown in figure 3.9. Table 3.3 summarizes the specifications of both objective lenses.

(a) Olympus Plan N 20x. **(b)** Olympus Plan N 40x.

Figure 3.9: Infinity-corrected microscope objectives from Olympus used on the microscope setup [48].

Table 3.3: Specifications of infinity-corrected microscope objectives [48, 49].

	Olympus Plan N 20x	Olympus Plan N 40x
Magnification	20x	40x
Numerical aperture	0.4	0.65
Working distance (mm)	1.2	0.6
Immersion medium	air/dry	air/dry
Wavelength Range	visible	visible

3.2.2 Tube lens

The microscope comprises an infinity-corrected microscope objective, which produces parallel beams that focus on the infinite. However, it is necessary to focus the light on the image plane [50]. This is done by an MS-200-SHORT tube lens with a focal length of 200 mm (figure 3.10) from Seiwa (Seiwa Optical Europe GmbH, Frankfurt, Germany).

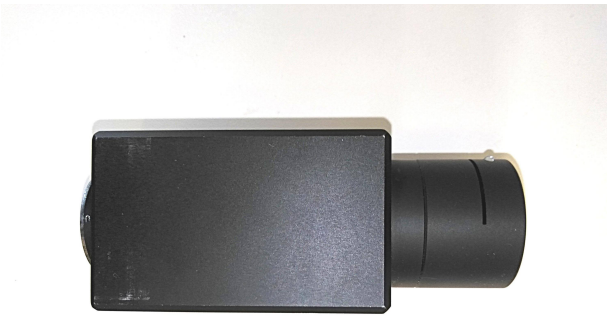

Figure 3.10: MS-200-SHORT tube lens from Seiwa.

3.2.3 Telecentric objective

A telecentric objective is used for the illumination of the sample. This type of objective has a non-angular field of view, which enables the light beams to focus on a flat surface [51,52]. Telecentric lenses are very useful in scanning systems, due to a proportional relation between the entrance and exit positions of light rays in the objective [52–54]. In this work, the excitation light is static, therefore it is not necessary to scan the laser beam.

The LSM04-BB telecentric objective from Thorlabs (Thorlabs GmbH, Munich, Germany), shown in figure 3.11, is used on the microscope. Although the optimal wavelength range of this objective is 810 to 890 and 1000 to 1100 nm, it was used for 440 nm since it was the only available objective. The consequence is a lower transmission efficiency [54]. Table 3.4 presents the main specifications of this objective.

Figure 3.11: LSM04-BB telecentric objective from Thorlabs [52].

Table 3.4: Specifications of the LSM04-BB telecentric objective from Thorlabs [54].

LSM04-BB	
Magnification	3x
Optimal wavelength range (nm)	810 to 890 and 1000 to 1100
Working distance (mm)	42.3
Numerical aperture	0.037
Effective focal length (mm)	54

3.2.4 Spherical and cylindrical lenses

It is important to change the shape of the laser beam to create a light-sheet. Our setup uses two convex spherical lenses (LA1509-ML and LB1761) and one convex cylindrical lens (LJ1703RM) from Thorlabs (Thorlabs GmbH, Munich, Germany) to this purpose. Figure 3.12 shows these lenses and table 3.5 summarizes their characteristics.

(a) LB1761 lens [55]. **(b)** LA1509-ML lens [56]. **(c)** LJ1703RM lens [57].

Figure 3.12: Spherical and cylindrical lenses from Thorlabs used in the microscope.

Table 3.5: Specifications of the lenses used in the microscope [55–57].

	LB1761	LA1509-ML	LJ1703RM
Classification	convex spherical	convex spherical	convex cylindrical
Focal length (mm)	25.4	100	75
Wavelength range (nm)	350 to 2000	350 to 2000	350 to 2000
Working distance[1](mm)	-	93.5	66.4

3.2.5 Emission filters

Emission filters are necessary to guarantee that the detected data is generated only from the emitted fluorescence photons. These filters only transmit light of a specific wavelength range, blocking the out of the range photons [47]. If there is no filter, scattered excitation

[1]At the design wavelength of 587.6 nm.

light will reach the CCD, resulting in incorrect measurements [6]. As seen in 3.1, the fluorescence photons have wavelengths between 520 and 570 nm, therefore the filters used on the microscope must transmit this range.

The spectral responses of the system emission filters are presented in figure 3.13. The filters transmission curves were obtained through an Ocean Optics Spectrometer. The filters are illuminated with white light and the spectrometer only acquires the transmitted wavelengths.

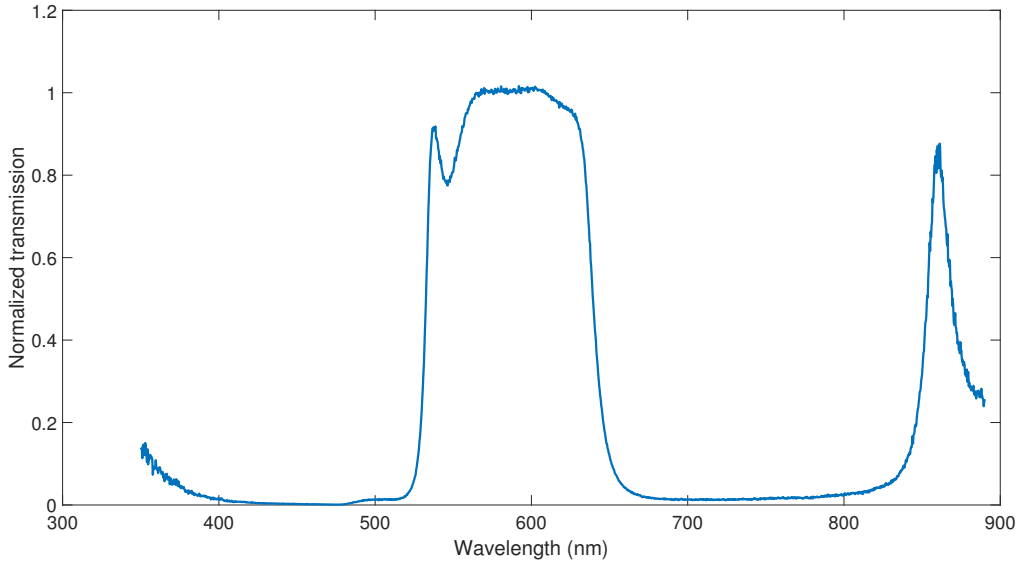

Figure 3.13: Measured spectrum of the normalized transmission of the emission filters.

3.3 Microscope setup

The microscope contains illumination and detection units. The spherical and cylindrical lenses, the mirror, and the telecentric objective are components of the illumination unit. The detection unit is similar to a wide-field microscope and comprises the infinity-corrected microscope objective, the emission filters and the tube lens [25]. The optical setup of the microscope is pictured in the diagram of figure 3.14.

The spherical lenses are used to enlarge the laser beam through a Keplerian beam expander. It has two converging lenses distanced by the sum of their focal lengths, with the lens with the lower focal length placed near the laser [58]. The magnification of the beam expander is 3.9, given by the ratio between the focal length of the LA1509-ML and

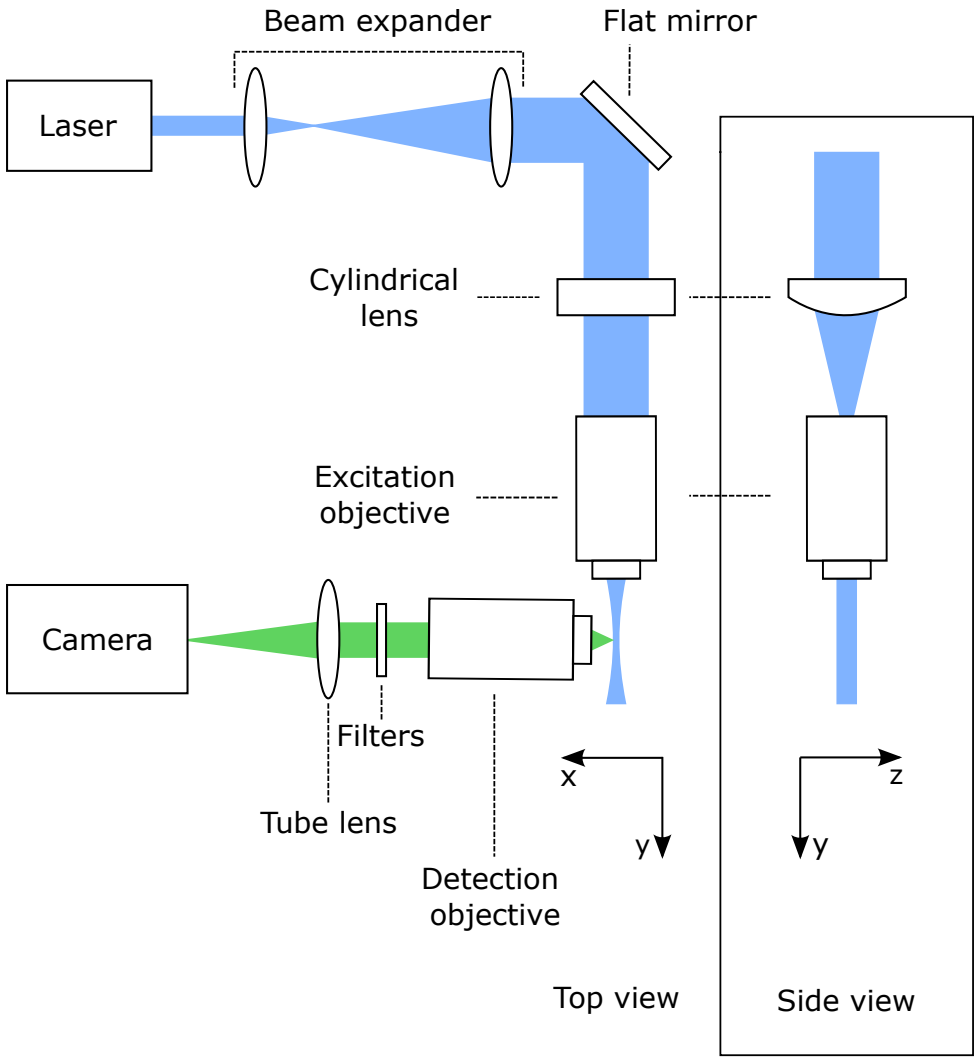

Figure 3.14: Diagram of the implemented microscope optical setup. The left image shows the top view of the setup and the right image demonstrates the side view. The beam expander increases the size of the laser beam and the flat mirror changes its direction in 90 degrees. The light beam passes through the cylindrical lens, which generates a line of light that fills the back aperture of the excitation objective along one axis. The cylindrical lens and the excitation objective define the height and thickness of the light-sheet, respectively. The excitation and detection objectives are perpendicular to each other. The sample is placed where the focal plane of both objectives intersect. The tube lens focuses the light from the detection objective to the CCD and the filters transmit only the fluorescence photons blocking the other wavelengths.

LB1761 lenses. The beam exits collimated from the beam expander and passes through a flat mirror to change its direction by 90 degrees.

The light beam goes to the cylindrical lens, which converges the light in one dimension leaving the other unaltered [59]. This convergence results in a line of light that fills the back aperture of the telecentric objective in just one axis. This objective cannot focus the light on the z-axis due to the thin dimension of the beam. Thus, the cylindrical lens

defines the height, and the numerical aperture of the objective determines the thickness of the light-sheet [29, 59]. The cylindrical lens decreases the beam height on the z-axis, and the telecentric objective produces a light-sheet creating a waist-like shape called beam waist [23].

The acquisition of the fluorescence photons occurs orthogonally to the illumination beam. Therefore, the excitation and the detection objectives are perpendicular to each other. The light-sheet should focus on the sample and the focal plane of the telecentric objective must coincide with the focal plane of the detection objective [59]. The infinity-corrected microscope objectives are used as detection objectives to collect the photons and the tube lens focuses the fluorescence photons on the CCD camera. The filters are placed between the detection objective and the tube lens to block wavelengths lower than 530 and higher than 640 nm.

This setup includes two actuators, a T-LA28A from Zaber (Zaber Technologies Inc., Vancouver, Canada) and an MT1A from Thorlabs. The T-LA28A actuator has a microstep of 0.099 μm and a travel range of 28 mm. This actuator is controlled by the computer through RS232. The MT1A actuator is a mechanical translation stage with a 12.7 mm range and a 0.5 μm microstep. The T-LA28A and MT1A are used to move the sample on the x-axis and the y-axis, respectively. These components are used to place the sample in the ideal imaging position, which is at the intersection of the focal plane of the telecentric and detection objectives.

Chapter 4

Microscope evaluation

The optical and timing parameters define the performance of a fluorescence lifetime microscope. The optical parameters are related to the imaging system and the timing parameters concern the accuracy and the precision in the lifetime estimations of the system. These parameters were measured in this work to evaluate the microscope. The measured optical parameters were the field of view, light-sheet thickness, axial resolution, and lateral resolution.

4.1 Field of view 36

4.2 Light-sheet thickness 41

4.3 Axial resolution 45

4.4 Lateral resolution 49

4.5 Timing accuracy 51

4.6 Results evaluation 54

4.1 Field of view

The field of view (FOV) defines the object observed by the microscope. This parameter depends on the optical components of the detection unit and on the CCD camera [23]. The FOV of the implemented microscope was measured for the two infinity-corrected microscope objectives, the Olympus Plan N 20x and the Olympus Plan N 40x. This parameter is calculated through the analysis of images of resolution test targets.

In this work, a negative 1951 USAF resolution test target was placed on the focal plane of the detection objective to determine the FOV. This type of target comprises different sizes of sets of three vertical and horizontal lines. Each set corresponds to an element and a group number. The size of the lines increases for lower element and group numbers. By using sets of three lines, this target prevents the occurrence of spurious resolution, which is recognizable by the appearance of blurred lines. This blurring causes the disappearance of a line from the set and inverted lines, which leads to erroneous resolution measurements. With sets of three lines, is easier to notice the disappearance of one line and consequently the occurrence of spurious resolution [60]. The target was dyed with fluorescent ink and illuminated by green light. The emitted photons have the same wavelength as the fluorescence photons under study. The recorded images of the target were used to calculate the FOV of the detection system.

Histogram stretching

An image enhancement technique must be applied to the recorded target images to improve their quality and enable their analysis [61]. This technique must increase the contrast of the image while preserving the information on the image. Therefore, we used a spatial domain enhancement technique. In this technique, the algorithms are applied directly to image pixels [61]. Histogram stretching was chosen as the contrast increasing technique. This technique extends the intensities of the pixels of an image to a given range [61]. This stretching was computed using the equation 4.1 [62]. The $f(x, y)$ is the pixel intensity at the position (x, y), f_{min} and f_{max} are the minimum and maximum pixel intensities of the image, respectively, and $g(x, y)$ is the new pixel intensity. The intensity images were stretched to an 8 bit range, following the DaVis software image representation. An 8 bit image ranges from 0 to 255, where 0 corresponds to the absence of light and 255 to the highest detected intensity.

$$g(x,y) = \left(2^8 - 1\right)\left[\frac{f(x,y) - f_{min}}{f_{max} - f_{min}}\right] \tag{4.1}$$

The acquired target image has pixels with very high intensity values that do not represent correct measurements. These values were considered as outliers by visual analysis. The emitted photons go through the lines of the target and get blocked outside those areas. Therefore, pixels with high intensity on black areas (blocked photons) are outliers. There are also outliers on areas corresponding to the lines of the target. These pixels are distinguished from the others by the abrupt variation of intensity.

The contrast of the image was increased using the histogram stretching technique (equation 4.1). The pixels considered as outliers were removed by changing its value to 0. These outliers were identified by having an intensity value higher than the signal maximum. Figures 4.1 and 4.2 show the intensity graphics of the target image acquired using the Olympus Plan N 20x, before and after removal of the outliers, respectively. Figure 4.3 shows the target image with the histogram stretching enhancement. The target images relative to the Olympus Plan N 40x objective are presented in the appendix A (figures A.1, A.2 and A.3).

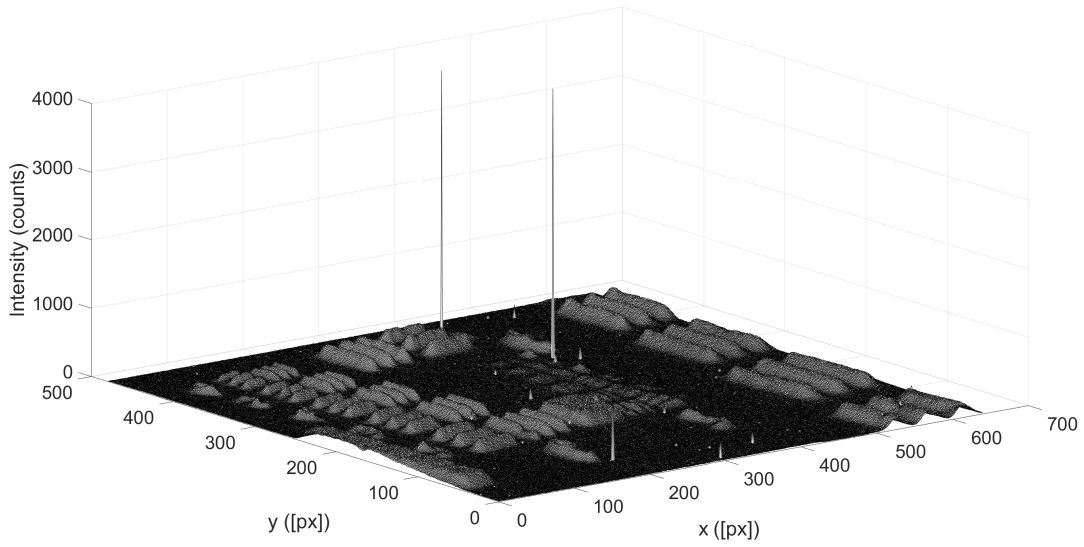

Figure 4.1: Intensities graphic of the target image acquired with Olympus Plan N 20x objective. There are isolated pixels with a disproportional intensity relative to the areas of signal corresponding to the lines of the target. These peaks are considered outliers.

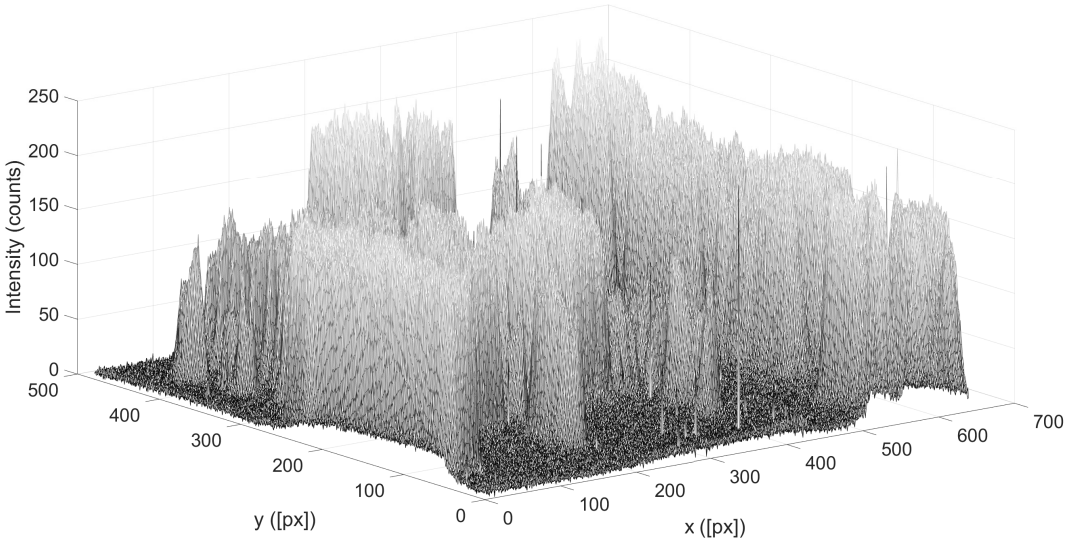

Figure 4.2: Intensities graphic of the target image acquired with Olympus Plan N 20x objective with outliers removed. There are some isolated pixels with higher intensity, but the histogram stretching resulting image is not affected due to almost uniform maximum intensities. A MATLAB®script was used to remove the outliers.

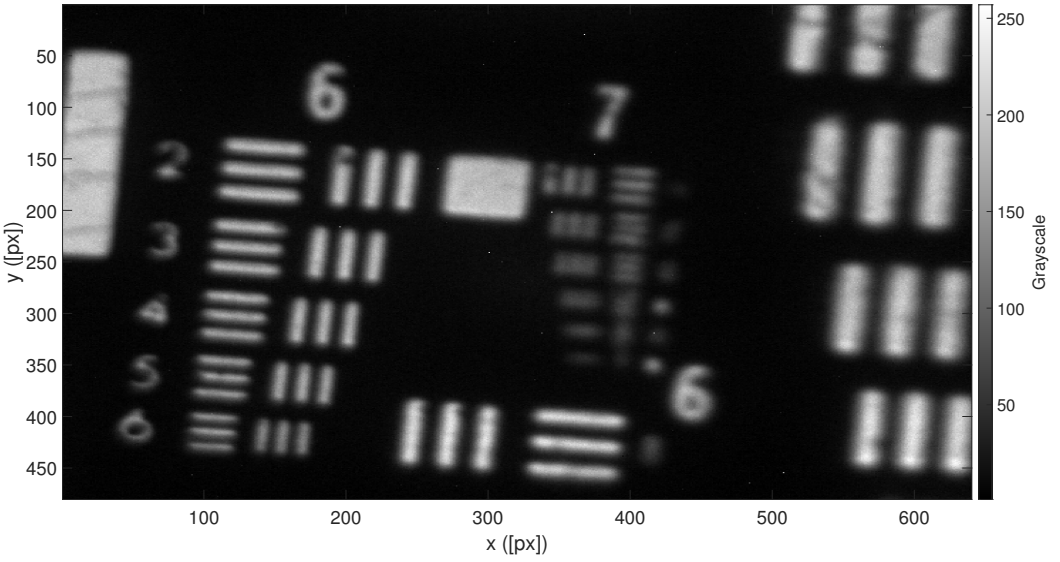

Figure 4.3: Acquired target image with Olympus Plan N 20x objective with the histogram stretching enhancement and outliers removed. Some outliers can be seen in the image. However their intensity is lower than the maximum of the signal and, therefore, do not negatively affect the data analysis.

Angle determination

The target was not properly positioned to be aligned with the detector, resulting in a slightly rotated image. Therefore, the angle of rotation of the target relative to the detection unit was determined to accurately calculate the FOV. A *region-of-interest* tool (Image Processing toolbox from MATLAB®) allows drawing a line over the image and show its properties. This tool was used to draw a line perpendicular to the set of lines of the target, giving the rotation angle of the target. The tool returns the initial and final positions of the line. These positions are used to obtain the angle through the geometric equation $\tan\alpha = \frac{y_2-y_1}{x_2-x_1}$. The method of drawing a line is not entirely precise due to the human interaction component, resulting in different angles on every measurement. The process was repeated six times for each target. The values of the angles are presented as mean ± standard deviation. The angles of the target relative to the x-axis and y-axis of the acquired image are summarized in table 4.1.

Table 4.1: Angles of the target relative to the x-axis and y-axis of the acquired image. The values are average ± standard deviation.

Objective	x-axis angle (degree)	y-axis angle (degree)
Olympus Plan N 20x	5.4 ± 0.7	84.2 ± 0.6
Olympus Plan N 40x	6.5 ± 0.9	82.9 ± 0.7

Line width determination

The pixel width of the detection unit was determined with the images of the set of lines of group number 6 and element number 2 for Olympus Plan N 20x and element number 4 for Olympus Plan N 40x. The *improfile* tool from the Image Processing toolbox was used to trace a path over the set of lines to give the values of the respective pixels. These values form three peaks corresponding to the lines of the target. The values of the middle peak underwent a nine-degree polynomial fitting to reduce the error. Next, the FWHM was obtained through the intersection of the polynomial fit with the half-maximum intensity. This process gives the width of one line in number of pixels. This method also requires to draw a path over the set of lines. Thus, as referred above, the points of the path are not the same in each reiteration, which decreases the precision.

A large visible set of lines of the target image was chosen to trace the path. The edges are more defined with increasing line width. Therefore, the width determination will be more accurate. Figure 4.4 shows the plot of the middle peak data, the respective nine-degree

polynomial fit, and the half-maximum intensity for the x-axis of the detection unit with the Olympus Plan N 20x objective. This procedure is repeated for the x and y-axis for both detection objectives. The plot for the y-axis with Olympus Plan N 20x and for the x and y-axis with Olympus Plan N 40x are shown in figures A.4 in the appendix.

The correct width of one line is calculated using the FWHM and the angles of the target through trigonometry. Table 4.2 summarizes the calculated widths for the x-axis and y-axis of the microscope detection unit with each objective.

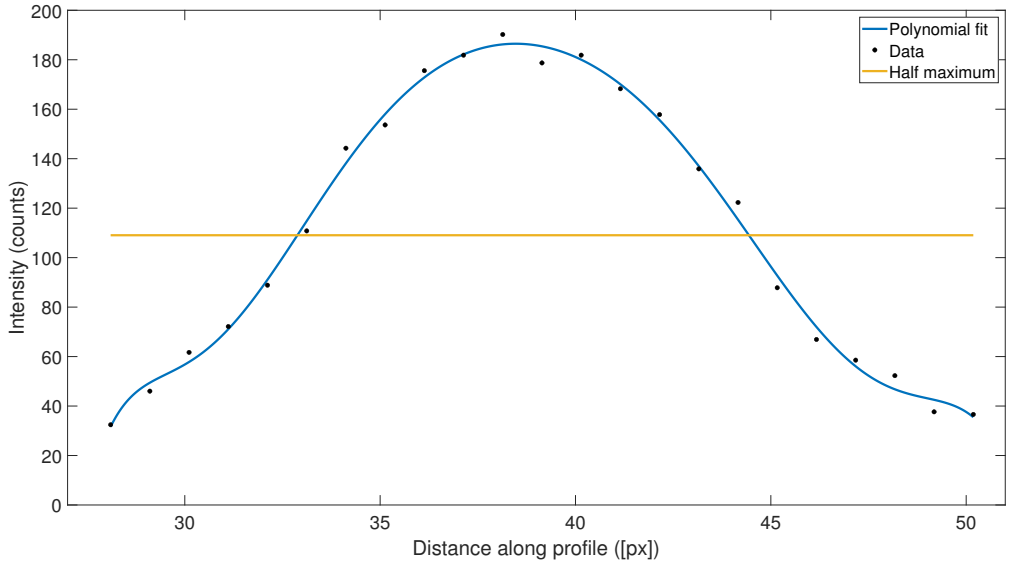

Figure 4.4: Plot of the middle peak data, the corresponding nine-degree polynomial fit, and the half-maximum intensity. The intersection allows to determine the width in number of pixels of one line for the x-axis of the detection unit, when using the Olympus Plan N 20x objective.

Table 4.2: Obtained widths in number of pixels of one line for the x-axis and y-axis of the detection unit. The values are average ± standard deviation.

Objective	x-axis line width ([px])	y-axis line width ([px])
Olympus Plan N 20x	11.5 ± 1.3	11.6 ± 0.7
Olympus Plan N 40x	15.3 ± 1.9	15.7 ± 1.5

FOV determination

The FOV was determined by the ratio of the true thickness of one line and the number of pixels of its width, multiplied by the number of pixels of one axis of the camera. This relation is shown in equation 4.2. The line thickness is defined by equation 4.3, and is

related to the element and group number of the set of lines [63]. When calculating the line thickness, is important to consider the angle of the target through trigonometry. The obtained FOV of the detection unit with each objective is presented in table 4.3.

$$\text{FOV} = \text{number of camera pixels} \times \frac{\text{line thickness}}{\text{line width}} \tag{4.2}$$

$$\text{line thickness [mm]} = \frac{1}{2^{\text{group}+1+(\text{element}-1)/6}} \tag{4.3}$$

Table 4.3: Obtained FOV for the detection unit with each objective. The values are average ± standard deviation.

Objective	x-axis dimension (μm)	y-axis dimension (μm)
Olympus Plan N 20x	390 ± 50	290 ± 20
Olympus Plan N 40x	230 ± 40	170 ± 20

Discussion

The FOV is larger for the Olympus Plan N 20x than Olympus Plan N 40x, a result that is expected due to a lower magnification factor. The FOV must be in accordance with the size of the sample structures under study. If the FOV is considerably larger than the sample structures, the observation of the details will be impaired.

The x and y-axis dimensions of the FOV has the same ratio as the scan size of the CCD. The choice of larger and focused line sets for FOV determination allowed more accurate results. This is due to a more defined and uniform line shape compared to smaller lines. A uniform line shape has an intensity profile with peaks well characterized. However, the several processing steps for the calculation of FOV induce an accumulation of errors and uncertainties in the measurements.

4.2 Light-sheet thickness

The light-sheet thickness is a characteristic of the illumination light and corresponds to the illuminated depth in the sample. This parameter was calculated through the knife-edge method. This method consists of moving a knife-edge perpendicularly to the beam

propagation axis to block the light [64]. The knife-edge can be placed at different distances over the beam. The power of the unblocked fraction of the beam is measured as a function of the knife-edge position [65]. This data allows to obtain the thickness of the beam at a specific distance over the beam propagation.

Knife-edge method and Khosrofian and Garetz fitting

The light-sheet thickness was measured using a Vega power meter from Ophir Photonics and a knife-edge on a micrometer with a resolution of 2 μm. The knife-edge moves horizontally on the x-axis until blocking the entire beam. Also, it was placed over the Zaber actuator to move across the beam propagation axis. The acquired data was fitted with a function developed by Khosrofian and Garetz [64] to obtain the thickness of the beam. The fitting function is shown in equations 4.4, 4.5 and 4.6. Here, P_N is the normalized power, x is the knife-edge position, x_0 is the center of the beam profile, and w is the beam radius. The acquired data were mirrored vertically and normalized to allow the fitting.

$$P_N(z) = \frac{1}{1 + \exp\left[a_0 + a_1 z + a_2 z^2 + a_3 z^3\right]} \tag{4.4}$$

$$\begin{aligned} a_0 &= -6.71387 \times 10^{-3} \\ a_1 &= -1.55115 \\ a_2 &= -5.13306 \times 10^{-2} \\ a_3 &= -5.49164 \times 10^{-2} \end{aligned} \tag{4.5}$$

$$z = \frac{\sqrt{2}(x - x_0)}{w} \tag{4.6}$$

Figure 4.5 shows the measured data with the Khosrofian and Garetz fit at position 0 along the beam propagation. Figure A.5 in appendix A shows the plots for other distances. The power meter and the micrometer have an error of 0.01 mW and 1 μm, respectively. The positions are not related to the distance from the excitation objective, but to the distance across sets of measurements. Thus, position 0 corresponds to the first measurement. The knife-edge was shifted in steps of 1 or 2 mm. Table 4.4 presents the obtained beam radius

with the respective 95% confidence interval for each position across the beam.

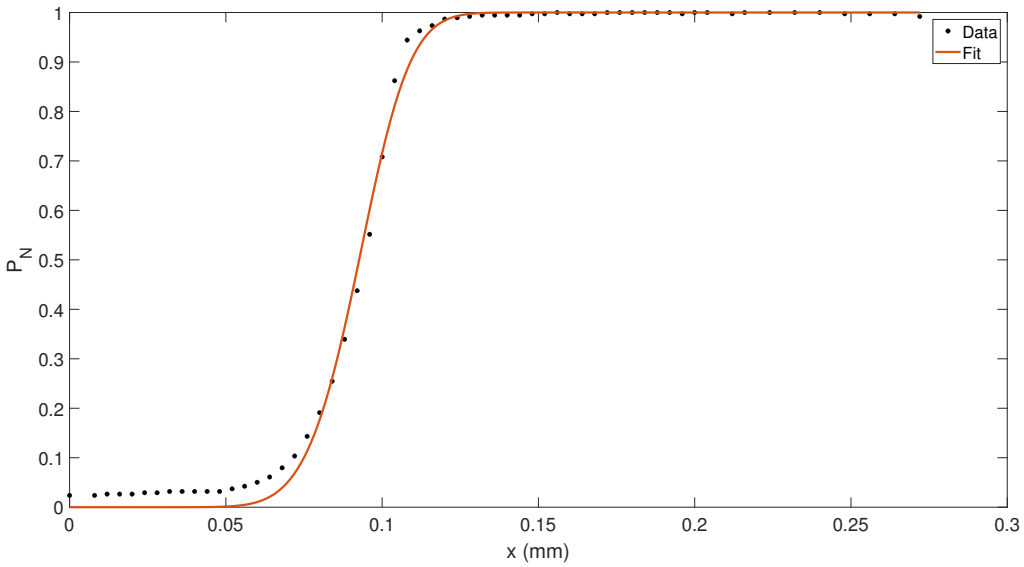

Figure 4.5: Plot of the measured data with the Khosrofian and Garetz fit at a position 0 along the beam propagation. P_N is the normalized power and x is the position of the knife-edge.

Table 4.4: Obtained beam radius with a 95% confidence level for different positions along beam propagation.

Position (mm)	Beam radius (mm)	Min confidence bound (mm)	Max confidence bound (mm)
0	0.01805	0.01680	0.01930
1	0.01873	0.01634	0.02113
2	0.01526	0.01390	0.01662
3	0.01332	0.01252	0.01412
5	0.03405	0.03214	0.03597
9	0.05137	0.04822	0.05451

Beam waist determination

There is no information on the specifications of the laser considering its mode structure. [44]. Therefore, it was considered as a non-Gaussian beam for the light-sheet thickness determination, since it is a diode laser. Equation 4.7 gives the model of the beam radius over its path. Here, x is the propagation axis, x_o is the waist position, and λ is the laser wavelength. The parameter w_o corresponds to the lower radius of the beam, named beam waist. The M^2 factor is a characteristic of the mode structure of the beam. It is higher than 1 for non-Gaussian beams and equal to 1 for Gaussian beams [66].

$$w(x) = w_0\sqrt{1 + \left[\frac{M^2\lambda}{\pi w_0^2}(x - x_o)\right]^2} \tag{4.7}$$

The data from table 4.4 were used to determine the beam waist through a fit with equation 4.7. There is no information about the M^2 factor value on the laser datasheet. Hence, it was necessary to evaluate different values for this parameter. The fit was applied for an M^2 factor of 1, 1.5, 2, and 3. The parameter $\frac{\lambda}{\pi w_o^2}$ was replaced by a coefficient on the software to reduce the fitting error. Figure 4.6 shows the plot of the obtained beam radius as a function of the position, with the beam waist fitting for $M^2 = 2$. The data errors correspond to the deviation between the beam radius and the confidence bounds. The actuator error is a lot smaller than the positions. So, the error in the position is negligible. Figure A.6 in the appendix A shows the fits for the remaining M^2 values. The values of the beam waist w_0 and position x_0 of the light-sheet are the same for each fitting. The value obtained for the beam waist was 16 ± 9 μm, resulting in a light-sheet thickness of 31 ± 17 μm.

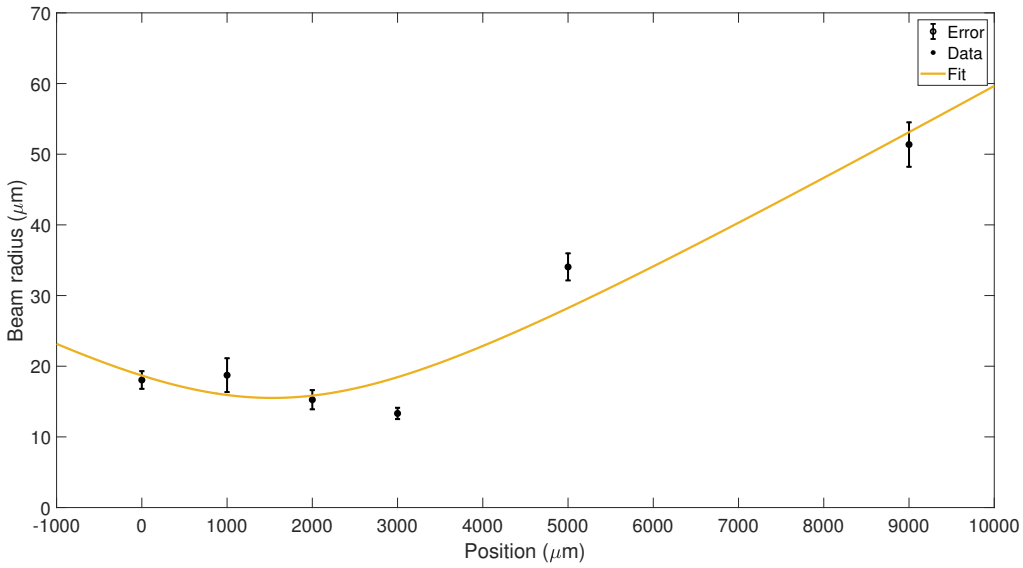

Figure 4.6: Plot of the measured beam radius as a function of the position with the respective beam waist fit for $M^2 = 2$.

Discussion

Theoretically, the Khosrofian and Garetz function have an error of 0.05% in the determination of the beam radius [64]. However, there is deviation between the fit and the measured data visible on figures 4.5 and A.5. Therefore, these deviations must be due

to errors in the measurement. The measured power might not correspond to the actual beam due to oscillations. Also, these values may be affected by stray solar light arriving to the CCD over the acquisition time.

The beam waist uncertainty is higher than half of the beam waist value. There is a lack of intersection of the fitting curve with the points, which might come from mechanical instability of the support. One possible solution to reduce the beam waist uncertainty is by increasing the number of beam radius measurements at different distances along the beam path. Also, the value of the beam waist does not change with the M^2, which indicates that the light-sheet thickness is independent of the laser beam mode structure.

4.3 Axial resolution

The axial resolution of the microscope is related to the optical sectioning. This resolution value depends on the light-sheet thickness and on the imaging capability of the detection unit. The optical sectioning allows to image slices of a thick sample due to a thin excitation beam, leading to clear and more defined images, due to the increased contrast that resulting from the absence of signal on the camera coming from layers above and below the focal plane [23].

Typically the axial resolution is determined using fluorescent microspheres, however, the samples were not available [67]. The axial resolution was measured using a fluorescent plastic slide. The plastic slide was moved towards the detection objective, intersecting the laser beam. An image of the plastic slide was acquired for each position increment. The average intensity of the acquired images in each position was used to calculate the axial resolution. This parameter was assessed for both objectives.

The fluorescent plastic slide works as an extended light source that approaches the detection objective in micrometer steps. The intensity distribution increases with the movement of the sample until it stabilizes at a maximum value. However, this effect is not observable. The intensity increases to a maximum and decreases with some oscillations afterward. This result is due to an internal filter effect. As the slide approaches the detection objective, a higher percentage of the laser passes through the plastic material. The plastic slide absorbs the excitation beam, and consequently, its intensity decreases and the same happens to the intensity of the emitted fluorescence photons. There is an absorption of the emitted fluorescence photons at higher depths due to a higher traveling distance across the plastic material.

Sigmoidal fit

The average intensity of the acquired images is presented as a function of the distance towards the objective. Only the data points before the intensity maximum are considered for determining the axial resolution. Also, the maximum intensity is prolonged over the distance to ensure that the fitting does not exceed this level. These intensities were normalized and fitted with a sigmoid function. The used sigmoidal fit is defined by equation 4.8 [68]. The value of the coefficient c was defined by inspection to minimize the fitting error. Figure 4.7 shows the plot of the intensity data with the respective sigmoidal fit for the microscope with each objective. Table 4.5 presents the obtained coefficients of the sigmoidal fit with uncertainties corresponding to the deviation relative to the 95% confidence bounds values.

$$y(x) = d + \frac{a}{1 + \exp\left[-(x - c)b\right)]} \tag{4.8}$$

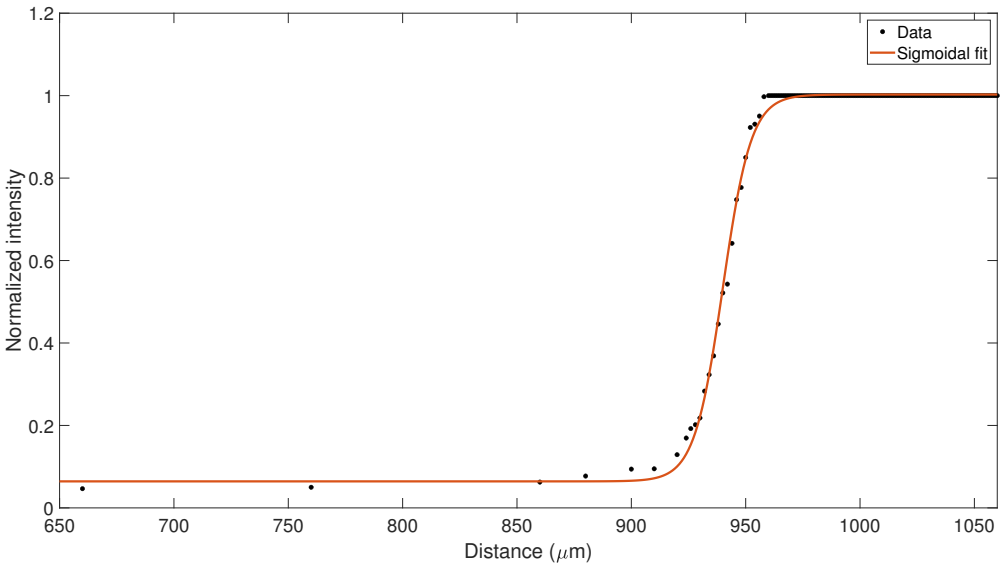

(a) Detection unit with Olympus Plan N 20x objective.

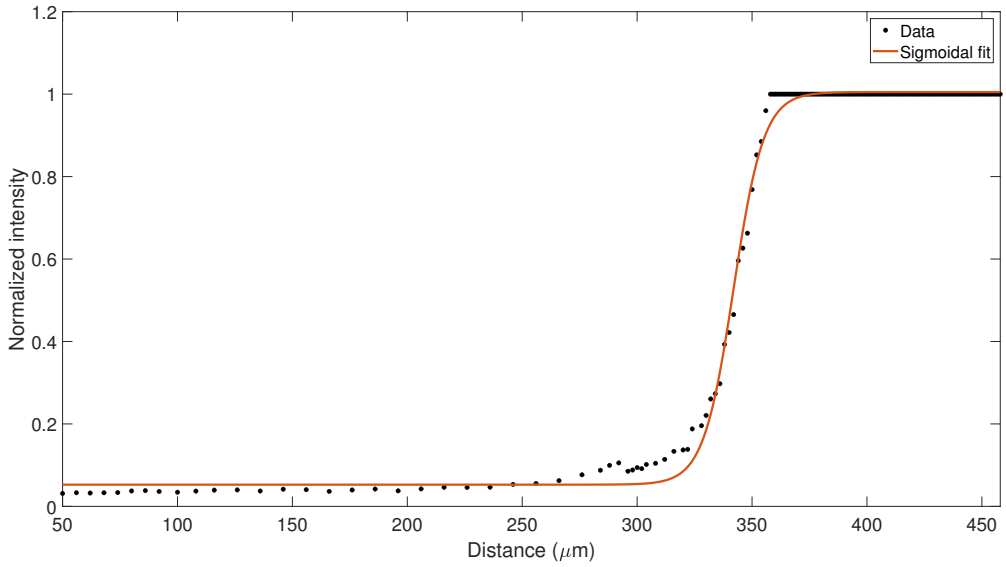

(b) Detection unit with Olympus Plan N 40x objective.

Figure 4.7: Plot of the intensity data with the respective sigmoidal fit for the microscope with each objective. The *Distance* is the fluorescent plastic slide path towards the objective.

Table 4.5: Coefficients of the sigmoidal equation used to fit the plot of intensity as a function of the traveled distance of the fluorescent plastic slide. The uncertainties correspond to the deviation of the obtained coefficients relative to the 95% confidence bounds values. The c value was defined by inspection to reduce the fitting error. The values are average ± standard deviation.

Objective	a	b	c	d
Olympus Plan N 20x	0.940 ± 0.009	0.160 ± 0.007	940	0.064 ± 0.007
Olympus Plan N 40x	0.952 ± 0.008	0.152 ± 0.009	342	0.053 ± 0.006

Axial resolution determination

The first derivative of the sigmoidal function has a shape close to a Gaussian curve and is defined by equation 4.9. The FWHM of this curve gives the axial resolution of the microscope [67]. Figure 4.8 shows the plot of the derivative of the computed sigmoidal function intensity and the half-maximum intensity of the microscope for each objective. The obtained axial resolutions of the microscope were 21 μm for the Olympus Plan N 20x and 23 μm for the Olympus Plan N 40x.

$$y(x) = \frac{ab\exp\left[-b(x-c)\right]}{\left(1+\exp\left[-b(x-c)\right]\right)^2} \tag{4.9}$$

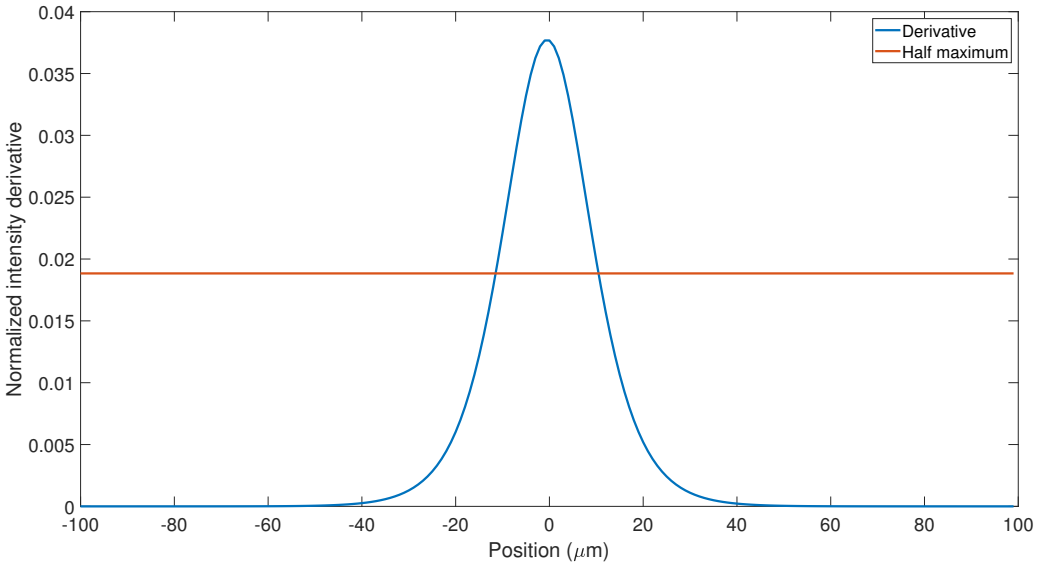

(a) Detection unit with Olympus Plan N 20x objective.

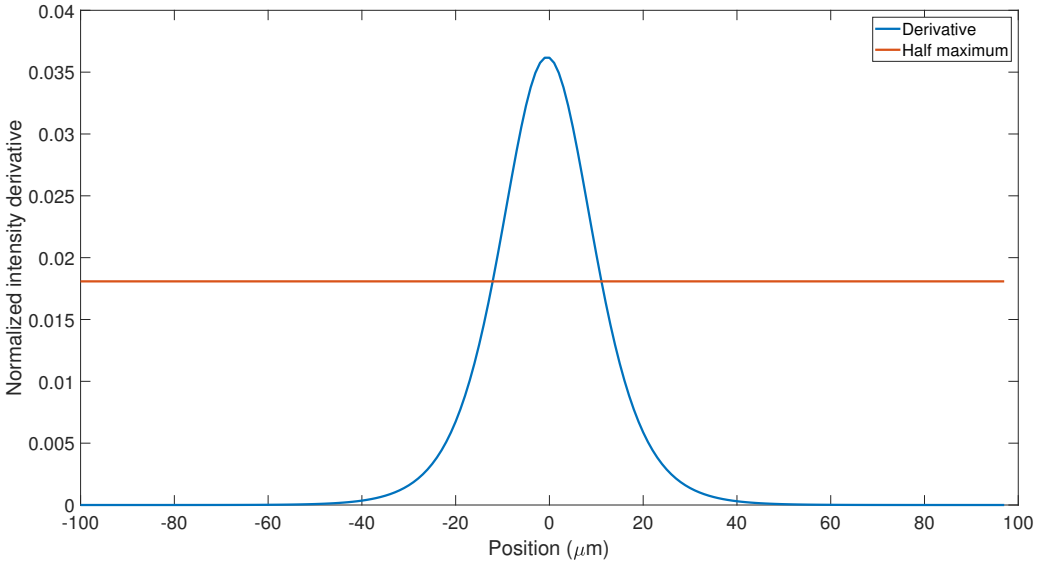

(b) Detection unit with Olympus Plan N 40x objective.

Figure 4.8: Plot of the first derivative of the computed sigmoidal function and the half-maximum intensity of the microscope with each objective. The intersections points give the axial resolution of the microscope. The y-axis is the derivative of the sigmoidal function intensity.

Discussion

The measured data has oscillations in intensity and the sigmoidal fit does not fit completely the data. As the unitary sigmoid function does not fit the measured data, a more general function was used (equation 4.8).

The fluorescent plastic slide was not the best sample to determine the axial resolution because is an extended light source. Hence, its intensity distribution does not follow a Gaussian function. The maximum measured value of intensity may not be the true value due to the internal filter effect. Consequently, the obtained axial resolution may not be the true resolution value. Usually, this parameter is obtained using fluorescent microspheres with dimensions smaller than the expected axial resolution. These samples behave as point light sources and move along the detection axis with a controlled actuator. The intensity distribution along the detection axis approximates a Gaussian function, wherein the FWHM gives the axial resolution [67].

4.4 Lateral resolution

The lateral resolution of the detection unit is defined by the shortest distance that allows distinguishing two points of the sample, located in the same focal plane. In theory, this parameter depends just on the numerical aperture of the detection unit and the wavelength of the fluorescence photons [23].

The target images shown in section 4.1 were used to determine the lateral resolution of the microscope. This includes both objectives and axes.

Lateral resolution determination

The *improfile* tool was used to draw a path perpendicularly to the set of lines. As described in section 4.1, this tool gives the intensity values of the crossed pixels. This data form a three-peak plot, in which the maximum and minimum intensities correspond to brighter and darker regions, respectively. The intensity plots of the detection unit with Olympus Plan N 40x reveal noise and nondefined peaks. Therefore, a moving average filter with five points was applied to smooth the curve and produce more defined peaks. Figure 4.9 shows the intensity plot of the set of lines with group number 7 and element number 3, with the respective moving average filter, of the acquired target image with Olympus Plan N 40x objective.

The relative amplitude of peaks and valleys intensities determine the lateral resolution. The averages of the peaks and valleys intensities are used to calculate the ratio between the minimum and maximum intensities. The process of obtaining the intensity plot and calculating the averages was repeated for several line sets until the intensities ratio meets

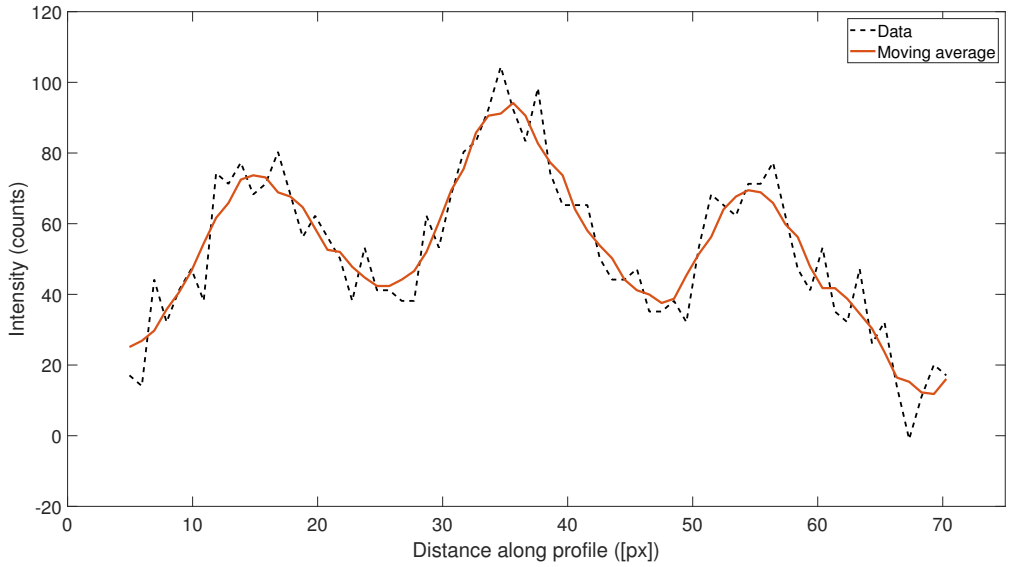

Figure 4.9: Plot of the intensity data from one line set with the moving average filter.

the Rayleigh criterion. This criterion defines that two points are distinguishable if the midway intensity is at most 0.735 of the maximum value [69]. Once the line set that meets the criterion is found, the width of the lines is calculated by equation 4.3. The line sets with group number 7 and element number 1 for Olympus Plan N 20x and element number 3 for Olympus Plan N 40x met the Rayleigh criterion. As the target has a rotation angle, the true line width is determined through trigonometry. This line width corresponds to the shorter distance the microscope can distinguish. The vertical and horizontal lines give the lateral resolution in the x-axis and y-axis, respectively. The lateral resolution for the x-axis and the y-axis of the detection unit for each objective is presented in table 4.6.

Table 4.6: Lateral resolution for the x-axis and the y-axis of the detection unit with each objective. The values are average ± standard deviation.

Objective	x-axis (μm)	y-axis (μm)
Olympus Plan N 20x	3.9 ± 0.3	3.9 ± 0.2
Olympus Plan N 40x	3.1 ± 0.3	3.1 ± 0.3

Discussion

The lateral resolution of the detection unit is in the range of 3 μm for both objectives. This resolution is the same on both the horizontal and vertical axes. The lateral resolution is better for the Olympus Plan N 40x due to a higher numerical aperture.

The intensities plots for the Olympus Plan N 20x has peaks well defined. However, a filter to reduce noise effects in data was needed for the Olympus Plan N 40x. This noise results from the target not being in the focal plane of the objective. Despite the processing, the noise could affect the determination of the true lateral resolution.

4.5 Timing accuracy

The timing accuracy represents the deviation of the measured fluorescence lifetimes compared to the reference values. The FLIMfit software was used to determine the fluorescence lifetime of the sample using the Time-Gated data. The acquired data does not correspond to the true fluorescence data. Instead, it is the convolution of the true fluorescence decay with the IRF. This function is approximately equal to the convolution of the excitation pulse with the camera gate function used in the acquisition [6]. As the laser pulse is shorter that the gate, the IRF will have a width close to the gate width. The IRF is longer for larger gate widths. The IRF was measured through the detection of the reflected excitation pulse, for the gates with nominal widths of 800, 900, and 1000 ps. Figure 4.10 shows the measured IRF for each gate width.

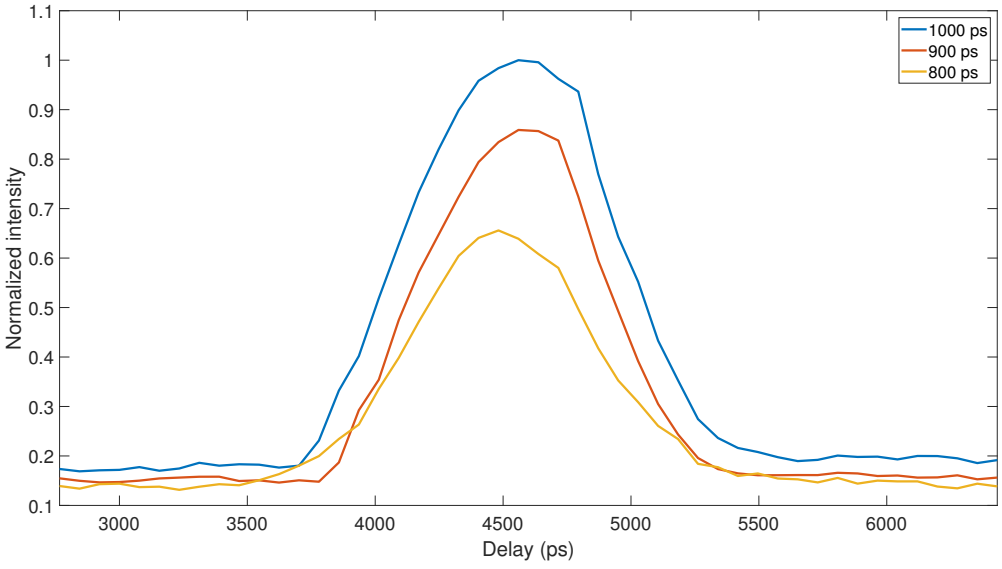

Figure 4.10: Plot of the measured IRF for gates widths of 800, 900, and 1000 ps.

Lifetime determination of samples

The Time-Gated microscope measured two samples of fluorescent dyes to obtain the timing accuracy of the system. These dyes must have excitation and emission wavelengths in the range of FAD. The samples were solutions of Coumarin 153 and Erythrosine B in methanol, which have a mono-exponential decay curve [70]. The data was acquired with the 1000 ps gate to ensure that a higher number of photons reach the CCD regardless of the MCP gain. The data acquired was processed using the FLIMfit software to estimate the lifetimes of the sample. Figure 4.11 shows the IRF and the fluorescence data of the samples with the obtained fluorescence decay. Table 4.7 summarizes the lifetimes resulting from the fluorescence decay fit and the corresponding reference values [70].

Table 4.7: Results of the samples measured lifetimes with the respective χ^2 and the relative error with the reference value [70]. The errors on the lifetimes correspond to the standard deviation, and the χ^2 is a measure of the goodness of fit [13]. Lifetime values are given as average $\pm$ standard deviation.

Sample	Reference lifetime (ns)	Measured lifetime (ns)	χ^2	Relative error
Coumarin 153 in methanol	4.3	4.0454 $\pm$ 0.6046	1.3226	0.059
Erythrosine B in methanol	0.47	0.4041 $\pm$ 0.0441	1.5993	0.14

Discussion

The observed oscillations of the decay fit curve are not expected. This effect possibly appeared due to a visual representation error. However, the resulting coefficients were considered correct because the fit followed a mono-exponential decay curve, as expected.

The timing resolution of the microscope is defined by the shortest lifetime the system is able to measure. In this case, the lifetime of the Erythrosine B was used to assess this parameter. The uncertainties of the lifetime measurements are in the range of 10 to 15%. The accuracy is given by the relative error which ranges from 5 to 14%. The aging of the fluorescence dyes influenced the error determination due to a decrease in the fluorescence properties of the samples.

Erythrosine B has a lifetime shorter than the width of the acquisition gates. Hence, there are fewer gates to acquire the fluorescence data due to the faster decay, resulting in a smaller number of images of the total fluorescence decay volume with a signal-to-noise ratio adequate to obtain accurate measurements. Usually, the signal-to-noise ratio is related to precision. However, more noise could affect the accuracy of measurements.

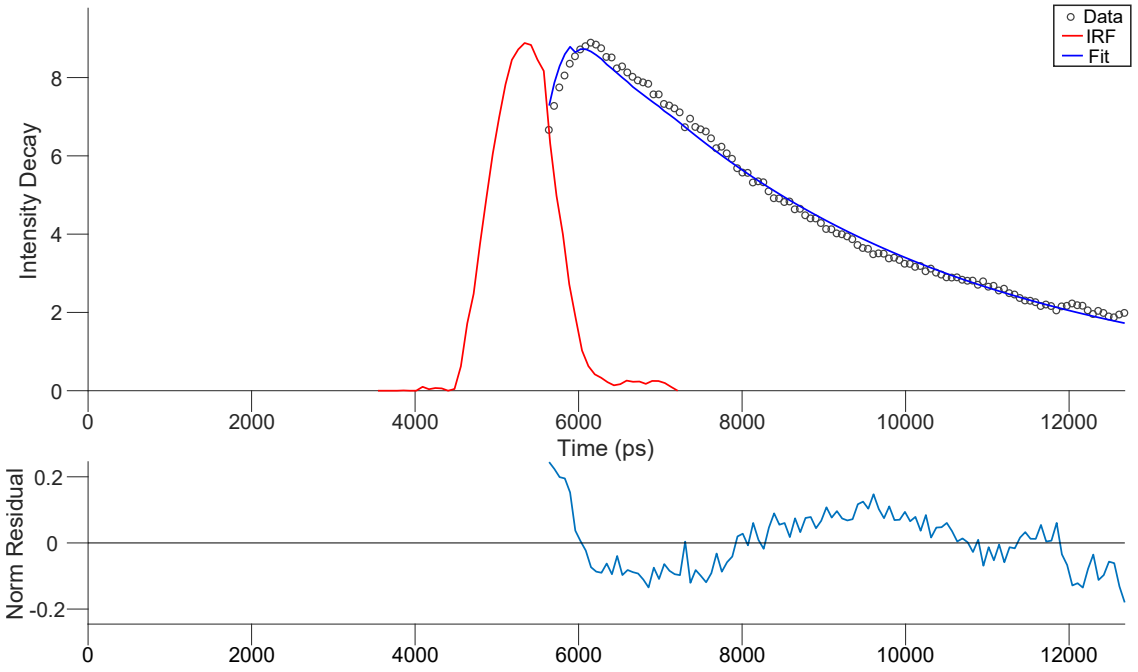

(a) Solution of Coumarin 153 and methanol.

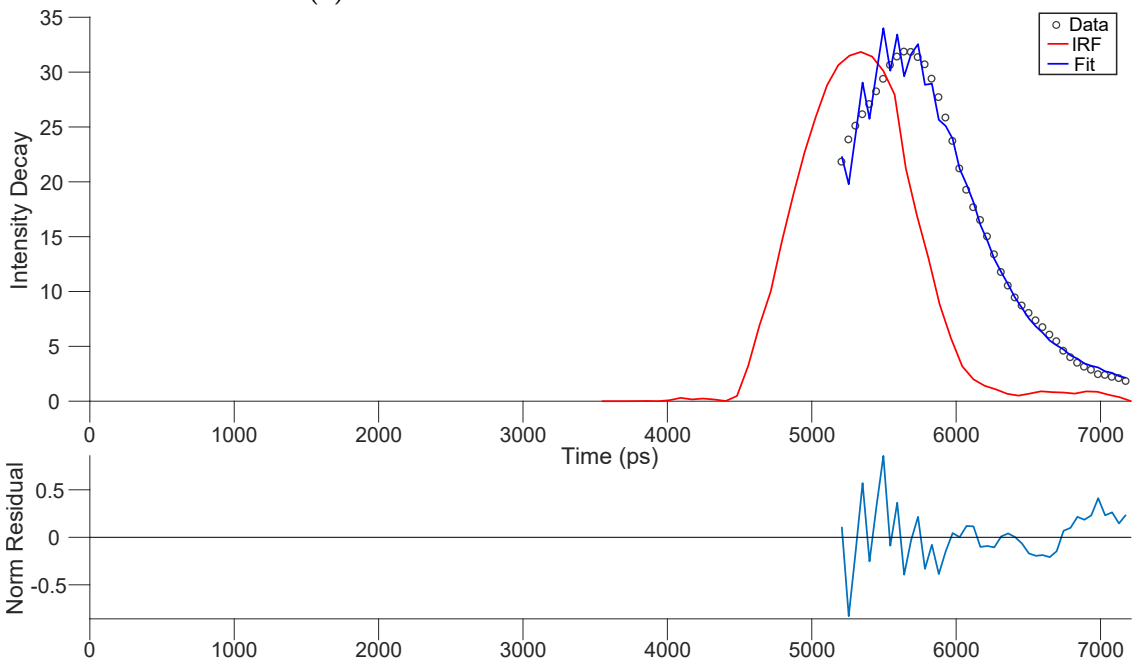

(b) Solution of Erythrosine B and methanol.

Figure 4.11: Plot of the obtained fluorescence decay from the acquired IRF and fluorescence data of each sample. The residual values correspond to the deviation of the data relatively to fit. The scale of the axes was defined by the software.

The Coumarin 153 has a lifetime four times longer than the gate width. This can explain the higher lifetime estimation error for Erythrosine B than Coumarin 153. Therefore, the system can have a more accurate lifetime estimation for samples with longer lifetimes than the acquisition gates. In this case, the system is more robust in estimating lifetimes

longer than 1000 ps.

4.6 Results evaluation

The FOV of the detection unit is 390 x 290 μm^2 for Olympus Plan N 20x and 230 x 170 μm^2 for Olympus Plan N 40x objective. The detection unit with Olympus Plan N 40x allows observing smaller areas compared with the other objective. Ideally, the sample under study must have an area larger than the FOV to ensure that the system only measures the sample.

The light-sheet defines the thickness of the excitation volume. The calculated light-sheet thickness is 31 μm. However, this value may not reflect the true thickness due to an uncertainty higher than 50%. Therefore, it is needed to improve the measurement process by reducing sources of systematic error from the materials and the process to obtain a more accurate value. Also, additional measurements are needed to reduce the uncertainty of the measurements.

The axial resolution indicates the shorter axial separation between two distinguishable separable objects. The obtained axial resolution of the microscope was 21 μm for Olympus Plan N 20x and 23 μm for the Olympus Plan N 40x. However, as seen before, the fluorescent plastic slide was not the best method to evaluate the axial resolution, inducing doubt in the reliability of the measurements.

The lateral resolution of the detection unit is similar for both objectives. The detection unit can distinguish different structures distanced by 3.1 μm for Olympus Plan N 40x and 3.9 μm for Olympus Plan N 20x. The objective with a higher numerical aperture has a better lateral resolution, a result that was expected since the lateral resolution is inversely proportional to the numerical aperture [6].

Regarding timing performance, the lifetime measurements are more accurate if the lifetimes of the fluorophores are longer than the acquisition gates. When the fluorescence decay is acquired, a higher number of gates generate larger amounts of data. In this system, the gate of 1000 ps was used to maximize the detected photons regardless of the MCP gain to reduce photon noise and shot noise on the image intensifier.

Chapter 5

Corneal imaging tests

5.1 Introduction 56

5.2 Animal corneas imaging 57

5.3 Discussion 64

5.1 Introduction

The main application of the developed microscope is the observation of corneas. Since the pig eyeball has an anatomical similarity with the human eye, pig corneas were chosen for the tests [71].

The human cornea is a transparent tissue and comprises five main structures (figure 5.1 and 5.2): the epithelium, Bowman's layer, stroma, Descemet's membrane, and endothelium. The Bowman's layer and Descemet's membrane separate the stroma from the epithelium and endothelium, respectively. The Bowman's layer is inexistent on pig corneas [71, 72].

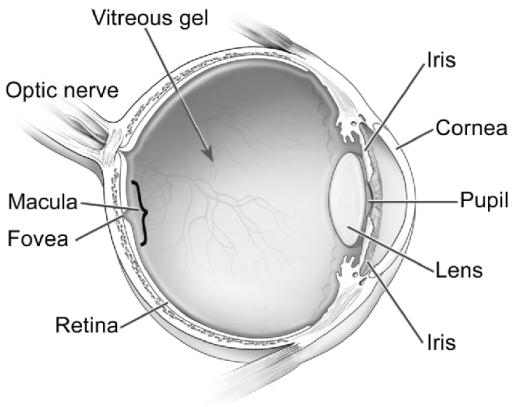

Figure 5.1: Diagram of the human eye structures [73].

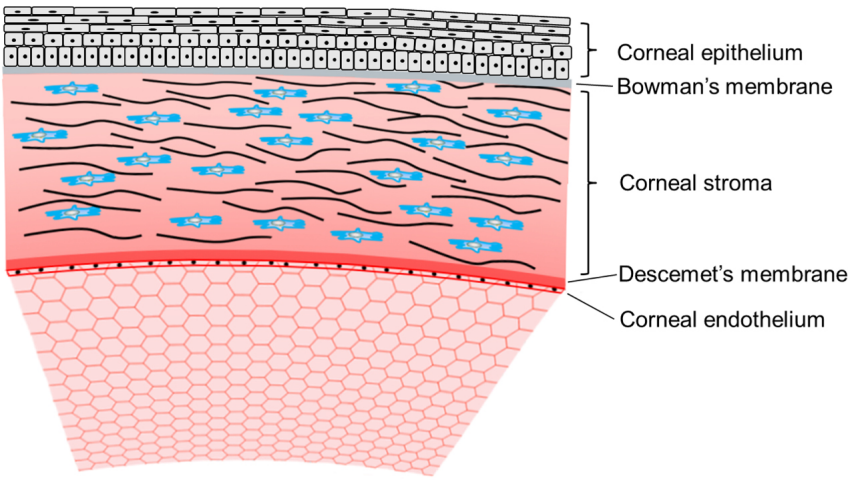

Figure 5.2: Diagram of the human cornea structures [74].

The external structure of the cornea is the epithelium and consists of three layers of cells:

superficial, wing, and basal, which are stacked from the outer (superficial) to inner (basal). The superficial cells have a flattened appearance and form a dense layer. The wing cells have a rounder shape and constitute the middle layer of the epithelium. The last layer is composed of basal cells, which have a larger and cylindrical shape. The stroma is the intermediate layer and corresponds to the thicker structure, making up around 90% of the cornea thickness and it is mainly made of collagen fibers. Also, nearly 5% of the stroma volume corresponds to keratocytes cells, which have a flattened shape. The endothelium is the inner structure of the cornea and consists of a single layer of cells. The Bowman's layer and Descemet's membrane are acellular structures formed by collagen fibers [6, 72]. Table 5.1 summarizes the thicknesses of the cornea and corneal structures for pig and humans [6, 71].

Table 5.1: Comparison of the pig and human corneal structures thicknesses [6, 71].

Structure	Pig thickness (μm)	Human thickness (μm)
Epithelium	80 ± 25	50 - 52
Bowman's layer	-	8 - 10
Stroma	~ 900	~ 470
Descemet's membrane	~ 30	~ 7
Endothelium		4 - 6
Cornea	~ 1010	$\sim$540

5.2 Animal corneas imaging

The microscope was used to observe the cornea epithelium and endothelium by acquiring the fluorescence photons of FAD, which has a bi-exponential decay. Since the cornea has a weak fluorescence signal due to a low concentration of FAD fluorophore, it was necessary to increase the exposure time to 5.12 seconds. Also, the MCP gain was set to 500 V to increase the counts in the CCD. The acquisitions were performed with the cornea placed in a holder with its curvature facing the detection unit.

Representative fluorescence intensity images of the epithelium, for each objective, are presented in figures 5.3 and 5.4. The lifetimes of the epithelium images were measured using the FLIMfit software tool. The data of the fluorescence intensity resemble a bi-exponential decay. The lifetimes measured in the epithelium are summarized in table 5.2. The fluorescence decays with the respective fit for each objective are presented in figures B.1 and B.2 in the appendix B. Despite the lifetime measurements, the fluorescence lifetime images of the epithelium do not allow distinguishing the different cells.

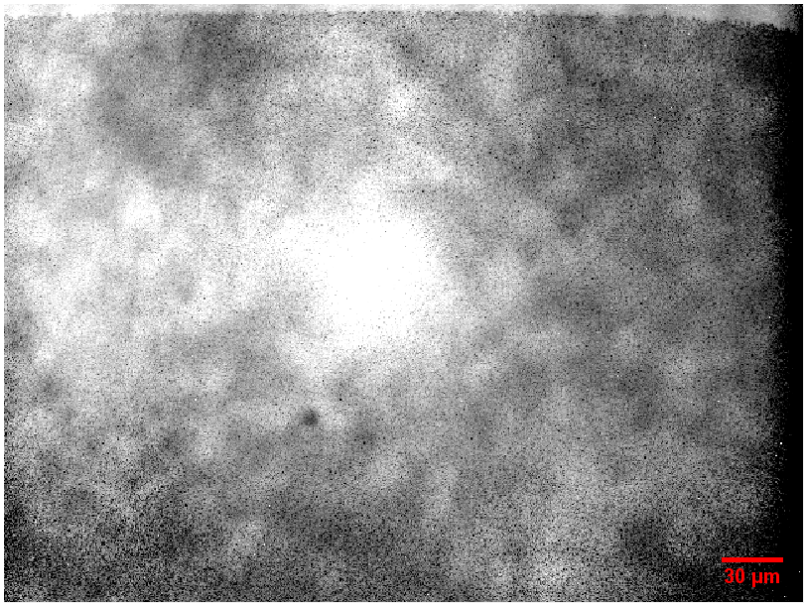

Figure 5.3: Fluorescence intensity image of the epithelium using the Olympus Plan N 20x.

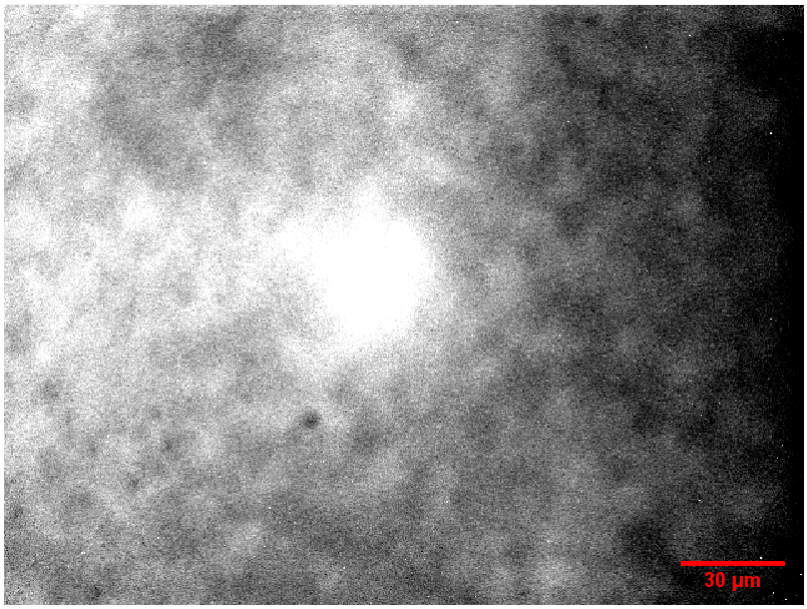

Figure 5.4: Fluorescence intensity image of the epithelium using the Olympus Plan N 40x.

The cornea was submerged in a fluorescein solution, which has a mono-exponential fluorescence decay, for 12 hours to increase its fluorescence and allow to distinguish its features. Later, the cornea was flipped and flattened using glass slides with the endothelium facing the objective. The acquired fluorescence intensity images of the endothelium are depicted in figures 5.5 and 5.6 for each detection objective. These images were also processed on the FLIMfit and fitted with an exponential decay. It was expected to observe a three-exponential decay due to components from the FAD and the fluorescein; however, the data approximate a bi-exponential decay. The fluorescence lifetimes of the endothelium

are also summarized in table 5.2. The fluorescence decays of the acquired images and the respective fit are shown in figures B.3 and B.4 in the appendix B.

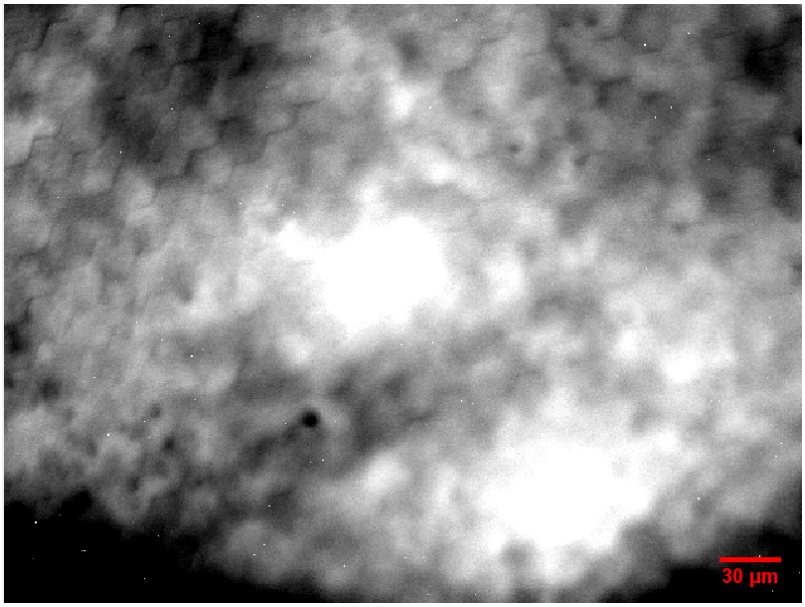

Figure 5.5: Fluorescence intensity image of the endothelium using the Olympus Plan N 20x. The visible honeycomb shaped structure is not a feature of the sample. It corresponds to the structure of the optical output from MCP of the GOI.

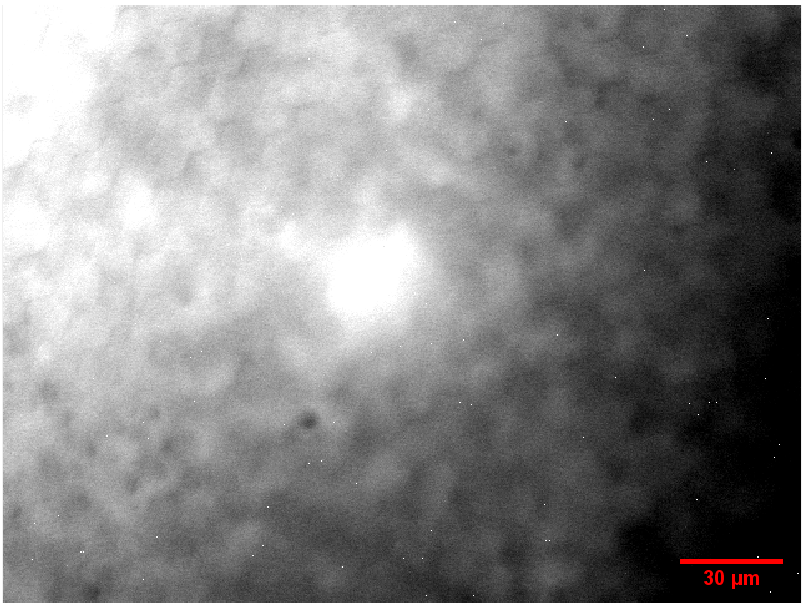

Figure 5.6: Fluorescence intensity image of the endothelium using the Olympus Plan N 40x.

Table 5.2: Measured fluorescence lifetimes of epithelium and endothelium for each objective. The errors on the lifetimes correspond to the standard deviation. The chi-square χ^2 is a measure of the goodness of fit [13]. The values are average ± standard deviation.

Objective	Structure	τ_1 (ns)	τ_2 (ns)	χ^2
Olympus Plan N 20x	Epithelium	29.590 ± 25.010	1.0257 ± 0.2643	0.9872
	Endothelium	4.4718 ± 3.3182	0.9311 ± 0.3889	1.3748
Olympus Plan N 40x	Epithelium	4.5758 ± 3.9142	0.8649 ± 0.2069	0.8437
	Endothelium	3.6365 ± 2.7245	1.1279 ± 0.2721	0.6223

The border of the cornea was observable in the fluorescence intensity images acquired with Olympus Plan N 20x, shown in figures 5.7a and 5.7b, by moving the support upwards on the detection plane. The lifetimes of these images are presented in table 5.3. The endothelium was the most external layer in these measurements.

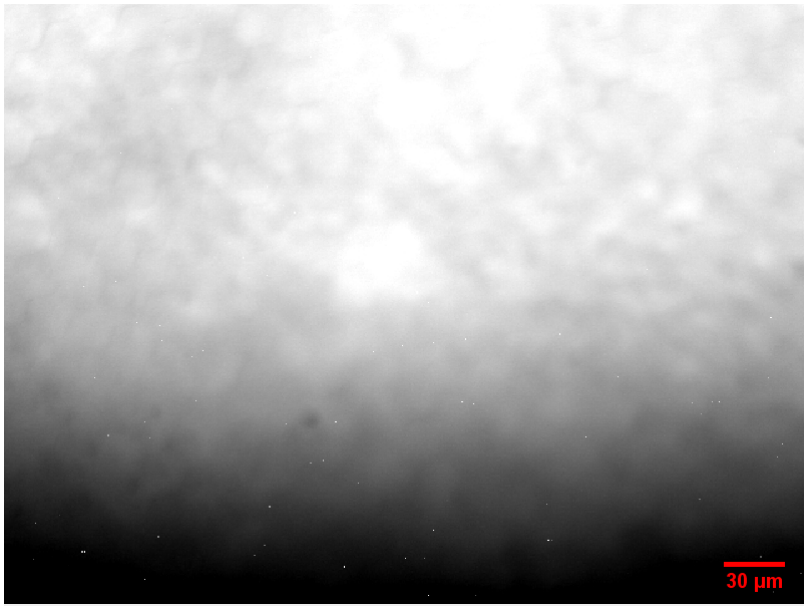

(a) The brighter regions correspond to the cornea, and its limit is visible.

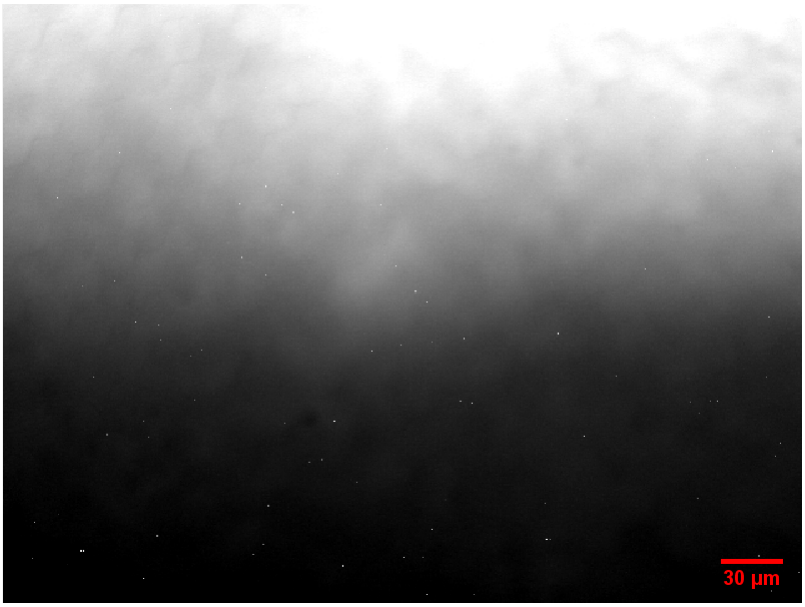

(b) The cornea is moved higher, showing half of the cornea in the image.

Figure 5.7: Fluorescence intensity image of the border of the cornea using the Olympus Plan N 20x.

Table 5.3: Measured fluorescence lifetimes of images 5.7a and 5.7b acquired with Olympus Plan N 20x objective. The errors on the lifetimes correspond to the standard deviation. The χ^2 gives the goodness of fit [13]. The values are average ± standard deviation.

Objective	Figure	τ_1 (ns)	τ_2 (ns)	χ^2
Olympus Plan N 20x	5.7a	4.1327 ± 1.2573	0.9724 ± 0.2176	1.0202
	5.7b	4.2028 ± 2.4672	1.1509 ± 0.3891	0.6117

It was only possible to obtain the fluorescence lifetime images of the cornea for the images presented in figures 5.5, 5.7a, and 5.7b. These images are depicted in figures 5.8, 5.9, and 5.10 with the respective range of the lifetimes τ_1 and τ_2.

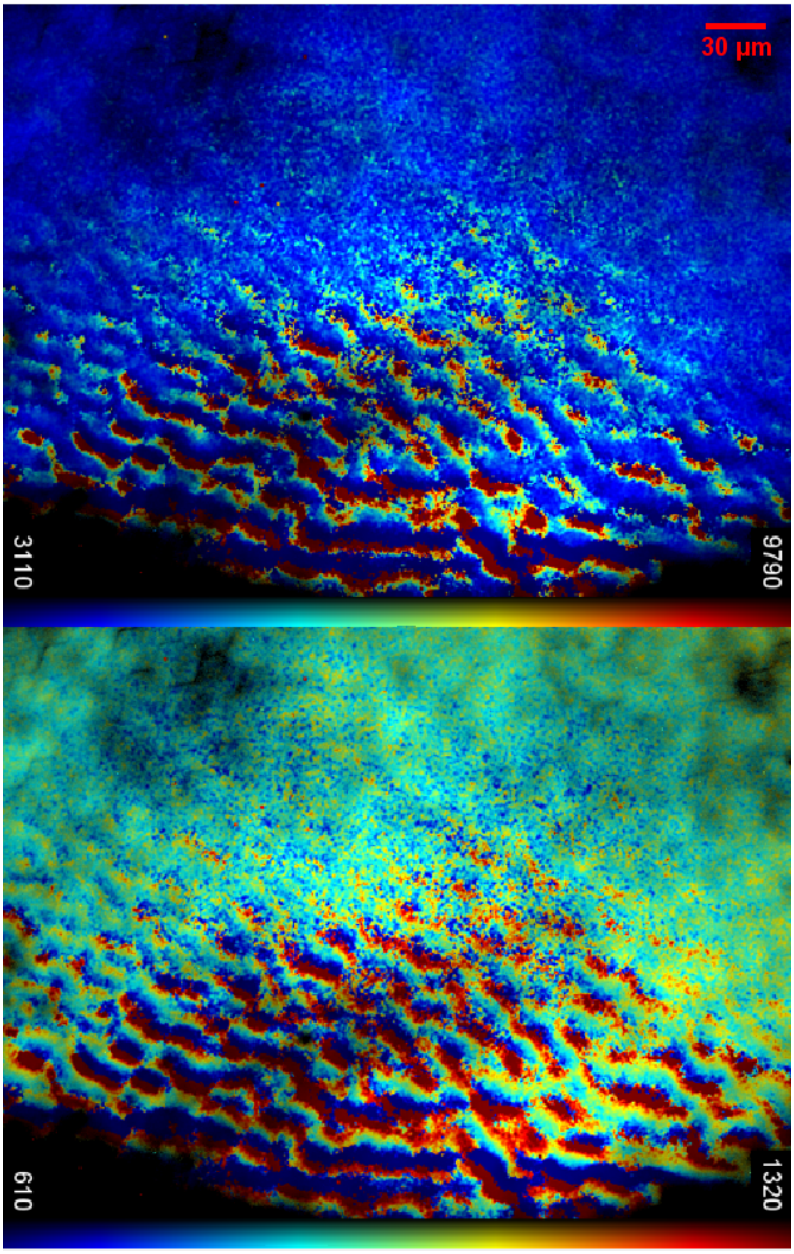

Figure 5.8: Fluorescence lifetime image of figure 5.5 merged with intensity image. The first image corresponds to τ_1 and the second image corresponds to τ_2. Both lifetimes are in picosecond scale.

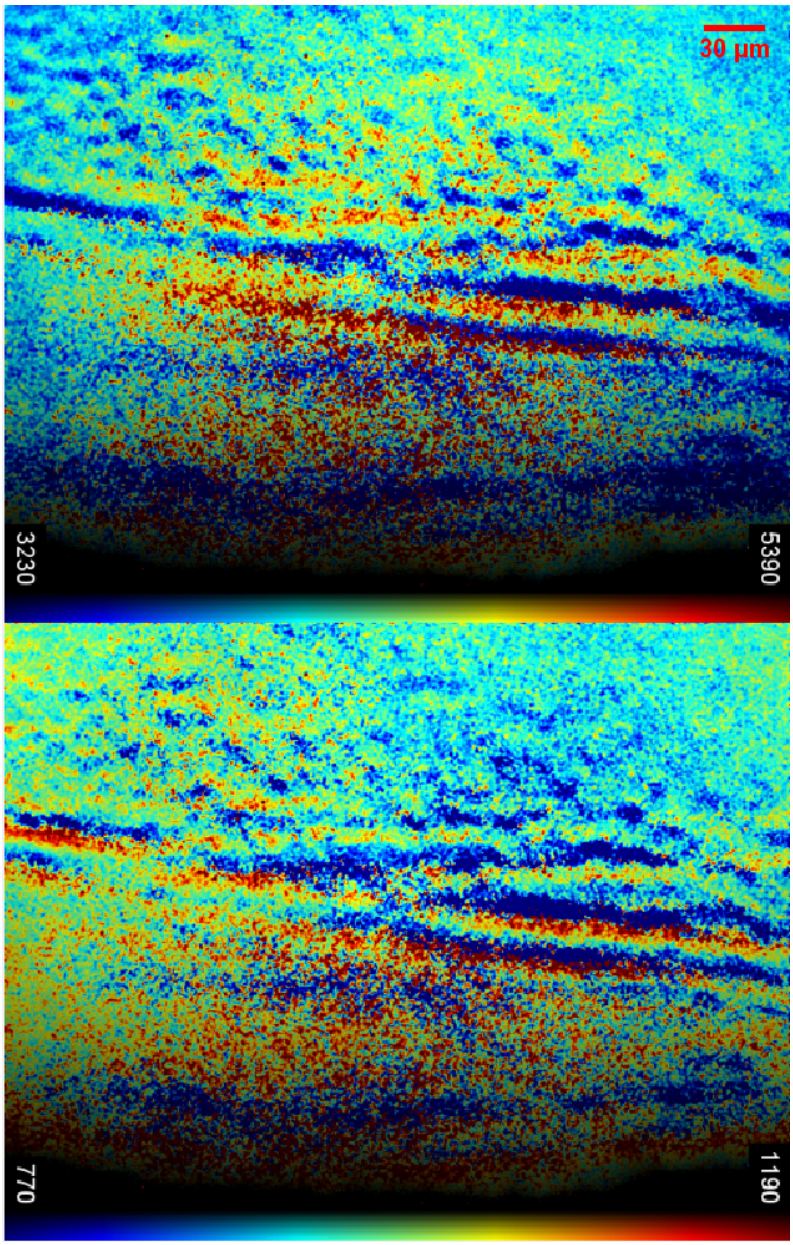

Figure 5.9: Fluorescence lifetime image of figure 5.7a merged with intensity image. The first image corresponds to τ_1 and the second image corresponds to τ_2. Both lifetimes are in picosecond scale.

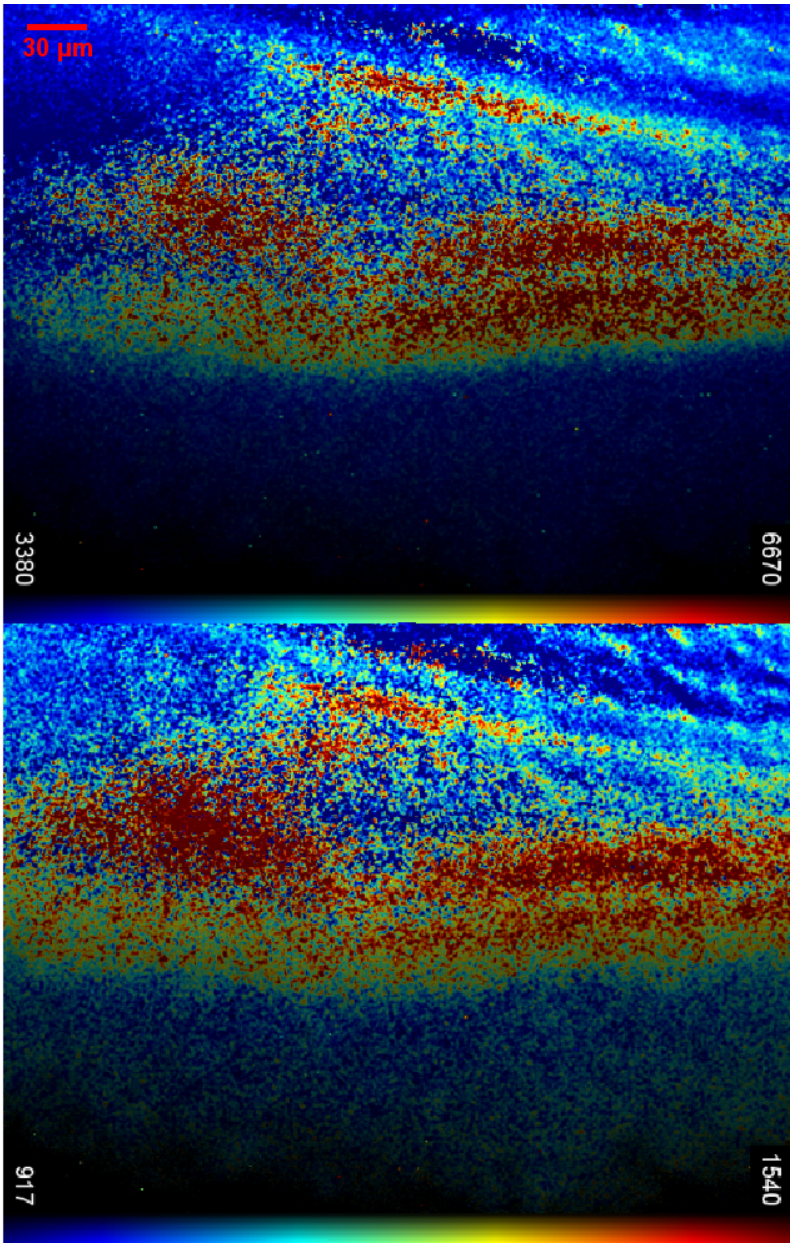

Figure 5.10: Fluorescence lifetime image of figure 5.7b merged with intensity image. The first image corresponds to τ_1 and the second image corresponds to τ_2. Both lifetimes are in picosecond scale.

5.3 Discussion

The images presented above show clearly that the optical sectioning of the the instrument is not adequate to image cellular features of the cornea. This is due to the large width of the excitation light-sheet. Fluorescence emission from out-of-focus planes anterior and posterior to the focal plane is imaged by the gated intensified camera. This emission blurs

the acquired images, decreasing their contrast and making impossible to visualize corneal cells.

The reference values of fluorescence lifetimes of FAD in pig corneas are 2.47 ± 0.89 ns and 0.55 ± 0.07 ns [75]. However, the pig cornea has collagen fibers, which are also fluorescent. The collagen fibers type 1 to 4 have an excitation peak at a central wavelength of 446 nm and emission in the range of 510 and 700 nm. Therefore, the microscope is able to excite collagen fluorescence and to detect its emission. Collagens type 1 to 4 have bi-exponential decay with lifetimes ranging from 0.47 to 0.74 ns, for the faster component, and 2.80 to 4.04 ns, for the slower component [8]. The fluorescein used to dye the cornea has a mono-exponential decay with a lifetime of 4 ns [76].

The measured lifetimes are different from the reference values. As the light-sheet has a measured thickness of 31 μm, fluorophores of different layers could have been excited simultaneously, resulting in an overlapping of their signals that affects the accuracy of the lifetime measurements.

The living cornea has a low concentration of FAD [6]. Moreover, this low concentration decreases for long *post-mortem* times. Therefore, long exposure times are required to image FAD fluorescence. However, the long exposure times lead to photobleaching, causing an irreversible loss of the fluorescence property of the corneal fluorophores. This effect impacts both on the precision and on the accuracy of the lifetime measurements. Photobleaching reduces the signal-to-noise ratio, particularly on the images corresponding to longer gate delays, decreasing the precision of the measurements. Moreover, photobleaching has an additional impact in Time-Gated instruments using an acquisition scheme where all the delayed acquisition gates are not present in any excitation cycle. In our microscope only one acquisition gate is active per excitation cycle. So, the acquisition gates corresponding to longer delays will deal with a smaller population of non-inhibited fluorophores in the sample. Therefore, when acquiring sequentially gated fluorescence intensity images it is highly likely that the decay profiles obtained in these conditions will have decay times different than those expected, affecting the accuracy of the lifetime measurements. Photobleaching should result in lifetimes shorter than the real values.

The lifetime τ_1 of the epithelium measured with Olympus Plan N 20x is almost ten times higher than the other τ_1 measurements. This results from the low counts of the acquired data. In the regions where the light-sheet loses intensity, the number of excited fluorophores is low. These regions are located mainly on the borders of the acquired image. In these darker regions, the value of τ_1 approximates the maximum value. The

minimum values of τ_1 are obtained in brighter regions. The intensity loss of the excitation light does not interfere with the measurements of lifetimes with Olympus Plan N 40x due to the lower FOV of the microscope when using this objective.

It was expected to measure the fluorescein lifetime with the data acquired from the endothelium. However, that was not the case. Fluorescein staining of the cornea occurs whenever there is disruption of cell-cell junctions, allowing fluorescein to accumulate in the intercellular space or to diffuse into the stroma. The lack of fluorescence signal can result from the preservation of the integrity of the corneal epithelium and endothelium, preventing the staining of the corneal layers.

Chapter 6

Computational evaluation of Rapid Lifetime Determination algorithm

The second part of this work was the evaluation of the accuracy and precision of the Rapid Lifetime Determination (RLD) algorithm in estimating the fluorescence decay parameters. RLD is the algorithm of choice whenever fast data acquisition is mandatory. This is the case of biological samples affected by photobleaching. It uses only two (mono-exponential decays) or four images (bi-exponential decays) and has low computational complexity.

6.1 Methods 68

6.2 Results 71

6.3 Discussion 73

6.1 Methods

The studies of the accuracy and precision were carried out through computational simulations of the algorithm on synthetic data, considering the effects of gain, noise and IRF of the developed system. The principles of the RLD were described in Chapter 2. As already referred, this algorithm is suitable for analyzing data acquired with Time-Gated systems.

The studies were based on simulated data of FAD fluorescence. The fluorescence decay of the FAD coenzyme has four fluorescence parameters due to its bi-exponential decay. The following reference values were used in this work: $\tau_1 = 550$ ps, $\tau_2 = 2470$ ps, $\alpha_1 = 0.65$, and $\alpha_2 = 0.35$ [75]. These parameters were used to generate four arrays of 100 x 100 elements (corresponding to the four decay parameters), where each array element was determined using a normal distribution, with mean equal to the corresponding reference value. The standard deviation was predefined as 5% of the mean value for each distribution.

A total of 25000 arrays of data with 100 x 100 elements were generated following equation 6.1, which is a model of the acquired fluorescence decay data [36]. In equation 6.1, τ_1, τ_2, α_1 and α_2 are the previously mentioned fluorescence lifetimes and proportion arrays, respectively, m is the array (image) number, corresponding to the sampling of the fluorescence decay along the time. $I(m)$ is the intensity as a function of the array number, $H(m)$ is the Heaviside function, T is the period of the excitation pulses and the N factor is used as a gain parameter.

$$I(m) = N \left\{ \left[H(m) + \frac{1}{\exp\left(\frac{T}{\tau_1}\right) - 1} \right] \alpha_1 \exp\left(-\frac{m}{\tau_1}\right) + \left[H(m) + \frac{1}{\exp\left(\frac{T}{\tau_2}\right) - 1} \right] \alpha_2 \exp\left(-\frac{m}{\tau_2}\right) \right\} \tag{6.1}$$

The 25000 data arrays represent the decay curve at intervals of 1 ps. The element (i, j) of the mth array was obtained with the decay parameters of the position (i, j). The decay curve was convolved with the measured IRF from the system to represent the acquired data. The code for the simulated fluorescence decay is shown below.

```
for i=1:arrayx
  for j=1:arrayy
```

```
    P1=(H+(1/(exp(number_arrays/tau1simul(i,j))-1))).*alpha1simul(i,j).*
   exp(-(arrays-delay)./tau1simul(i,j));
    P2=(H+(1/(exp(number_arrays/tau2simul(i,j))-1))).*alpha2simul(i,j).*
   exp(-(arrays-delay)./tau2simul(i,j));
    decaycurve=P1+P2; %equation of I(m) without N
    decaycurve=conv(decaycurve,g); %convolution with IRF
    norm_decaycurve=decaycurve./max(decaycurve); %normalization
    temp_decaycurve=norm_decaycurve.*(SPH/E).*k.*n; %add N
    value_decaycurve(i,j,:)=temp_decaycurve; %generate 25000 arrays of
   100 x 100 with fluorescence data
  end
end
```

Noise from the HRI was added to the simulated data using equation 6.2, which is an adaptation for our system of the one described by McGinty et al., where σ_I is the standard deviation of the signal, η is the quantum efficiency, k is the gain of the MCP, E is the excess noise, N_{ph} is the number of detected photons and σ_{CCD} is the readout noise associated with the CCD [6, 21]. The simulations were performed using the camera gains from 1.05 to 5.2 counts/electron. The gain and excess noise as a function of the MCP voltage are presented in table 6.1. The code for adding noise to the fluorescence decay is presented below.

$$\sigma_I^2 = \eta^2 k^2 E N_{ph} + \sigma_{CCD}^2 \tag{6.2}$$

Table 6.1: Gain and excess noise used in the simulations as a function of the MCP voltage.

MCP voltage (V)	k gain (cnts/e$^-$)	E
500	1.05	2.203
550	2.41	1.842
600	5.2	1.653

```
  for i=1:number_arrays
  value_decaycurve(:,:,i)=normrnd(value_decaycurve(:,:,i),sqrt(E*(k*n)
   ^2)); %add E*(k*n)^2 noise in the data
  value_decaycurve(:,:,i)=m*value_decaycurve(:,:,i); %increase counts
  end
```

```
for i=1:number_arrays
  value_decaycurve(:,:,i)=value_decaycurve(:,:,i)+normrnd(0,readout,
 arrayx,arrayy); %add readout noise in the data
end
```

The simulated fluorescence decay is divided into four integration windows due to FAD bi-exponential decay. The total counts of the simulated data were defined as the summation of the mean of each integration window. The maximum intensity peak of the simulated decay curve was chosen as the beginning of the first integration window for the RLD method. The other three windows have a shift from the first window defined by the Δt parameter. This parameter establishes the time interval between the beginning of consecutive gates. The gates are overlapped when Δt is lower than the gate width. The simulations were applied to a gate width of 1000 ps and a Δt parameter from 500 to 4000 ps. The RLD algorithm was evaluated for 10^4, 10^5, and 10^6 counts with laser power set to 80%, 90%, and 100%. The total number of counts was controlled by the gain parameter N (equation 6.1).

The accuracy and precision were measured for the parameters τ_1, τ_2, α_1, α_2 and α_1/α_2 ratio estimated using the RLD algorithm. The accuracy corresponds to the relative error and the precision to the standard deviation of the estimations (equations 6.3 and 6.4) [6]. The ratio α_1/α_2 is the free to protein-bound ratio used to evaluate cell metabolism [6]. The values of α_1 and α_2 were calculated through the pre-exponential factors of the decay (equation 6.5).

$$\text{accuracy} = \frac{|\text{average value} - \text{reference value}|}{\text{reference value}} \times 100\% \tag{6.3}$$

$$\text{precision} = \frac{\sigma_{\text{measurements}}}{\text{average value}} \times 100\% \tag{6.4}$$

$$\begin{aligned} \alpha_1 &= \frac{k_1}{k_1 + k_2} \\ \alpha_2 &= \frac{k_2}{k_1 + k_2} \end{aligned} \tag{6.5}$$

6.2 Results

The evaluation of the accuracy and precision of the RLD algorithm consisted of three tests: for different MCP gains, laser powers and total counts, for different values of τ_1 and τ_2, and different values of α_1 and α_2. The results of the simulations are presented in appendix C due to a high number (130) of graphics. The following parameters used in the simulations were predefined: Δt, gain, total number of counts, laser power, gate width and fluorescence decay parameters.

The simulations for different gains, laser powers, and counts yielded figures C.1 to C.9. Here, the accuracy and precision errors of the estimated parameters were calculated for Δt from 500 to 4000 ps. These errors were determined for 10^4, 10^5, and 10^6 total counts, with the laser power set to 80, 90, and 100% and for the gains of 1.05, 2.41, and 5.2 cnts/e^-.

The evaluation of the sensitivity of the RLD algorithm to different values of τ_1 and τ_2 generated figures C.10 and C.11. Here, the value of τ_1 ranged from 350 to 600 ps and τ_2 from 2000 to 3000 ps. The α_1 and α_2 were kept equal to the reference values presented in section 6.1. A Δt from 1500 to 2500 ps was selected for this simulation due to the stability of accuracy and precision in that range. The simulations were performed with the laser power set to 90%, for 10^4 counts and for gains of 1.05 and 2.41 cnts/e^-. This test was done just for total counts of 10^4 since it was meant to mimic conditions found when imaging endogenous fluorescence from biological samples. Endogenous fluorescence emission is usually weak, rendering impossible to achieve high values of total counts with a short acquisition time.

The evaluation for different values of α_1 and α_2 produced figures C.12 and C.13. The values of these parameters ranged from 0.2 to 0.8 for α_1. Since the sum of α_1 and α_2 is constant and equal to one, the parameter α_2 varies from 0.8 to 0.2. The reference values presented in section 6.1 were used for τ_1 and τ_2. The simulations were computed for Δt from 1500 to 2500 ps and the laser power set to 90%. The accuracy and precision were obtained for 10^4, 10^5, and 10^6 total counts and 1.05 and 2.41 cnts/e^-.

The RLD algorithm was simulated for a gate width of 1000 ps. In these simulations, the RLD algorithm could not obtain the decay parameters for Δt lower than 700 ps. The shorter lifetime was defined as τ_1 and the longer lifetime corresponds to τ_2. The most relevant results are:

Test 1 - Figures C.1 to C.9

- The accuracy and precision of the decay parameters are not affected by the values of the laser power.
- Higher camera gains degrade the accuracy and precision of the measurements, this being more relevant for lower values of total counts.
- The accuracy and the precision of the decay parameter shows an almost constant value for gate separations between 1500 to 2500 ps, in particular for total counts 10^5 and 10^6. This is an important result because allows to identify a range of operating parameters where RLD measurements of FAD decays have predictable errors and uncertainties.
- In the range of Δt equal to 1500 to 2500 ps there are no significant differences of accuracy and precision when increasing the total count from 10^5 to 10^6.
- Accuracy and precision are always better for the longer lifetime independently of the condition tested.
- Accuracy and precision are always better for α_1 independently of the condition tested.
- The precision of the ratio depends of the uncertainty propagation from parameters α_1 and α_2.
- For the decay lifetime, it is possible to obtain an accuracy and precision below 10% for total counts 10^5 and 10^6 for all camera gains that where evaluated.
- For total counts equal to 10^4 is also possible to obtain accuracy and precision below 10% for the longer lifetime (τ_2).
- For the metabolic ratio (α_1/α_2), it is not possible to obtain an accuracy error below 20%, even for high values of total counts.
- Precision better than 10% for metabolic ratio is only possible for total counts of 10^5 and 10^6.

Test 2 - Figures C.10 and C.11

- Results confirms that the accuracy and precision degrades for higher values of camera gains.
- The accuracy of the shorter lifetime and of the metabolic ratio is relatively insensitive to variation on the average value of the shorter lifetime. However, the accuracy degrades as the values of the longer lifetime decreases.
- The accuracy and precision of the longer lifetime component varies with the shorter lifetime, with the performance degraded as this value decreases. However, the accuracy and precision is always better than 10%.
- The precision of the shorter lifetime is more sensitive to variations of its mean time and is also affected by variations of the longer lifetime. For the conditions studied, the precision remains below 25%.
- The accuracy of ratio is degraded by variations of the longer lifetime leading to errors higher than 50%.

Test 3 - Figures C.12 and C.13

- For high values of total counts, the accuracy and precision of the shorter lifetime is relatively insensitive to variations of the pre-exponential factor.
- The precision of the longer lifetime has the same behavior but its accuracy degrades for high values of the factor α_1. However, the accuracy error is always very small.
- Accuracy of ratio degrades considerably for lower values of α_1. This effect is increased significantly for high total counts. The precision of ratio is relatively insensitive for total counts of 10^5 to 10^6. For total counts of 10^4, this factor degrades significantly.

6.3 Discussion

There are published studies concerning optimal gating schemes for achieving higher precision with RLD, both for mono-exponential [39,77,78] and bi-exponential decays [15,38]. The influence of the gating scheme on the accuracy of measurements is addressed in a previous study from the Instrumentation Group [79]. It is clear that each particular set

of true decay parameters has its own optimal gating scheme. The determination of this optimal scheme can be very complex since it is possible to consider schemes with overlapping or non-overlapping gates or even schemes using gates with different widths. We restricted our analysis to schemes using gates of equal width.

It is desirable to work with gating schemes that lead to reduced error and uncertainty that remain stable for a broad range of gating parameters, in particular the time interval between gates. The simulations were performed for a gate width of 1000 ps and revealed that, for gate intervals Δt in the range from 1500 to 2500 ps, the accuracy and the precision of decay parameters remains rather stable.

The camera gain affects the accuracy and precision due to the shot noise from the electron multiplication process in the image intensifier. Therefore, lower gains are preferable to obtain reduced error and uncertainty. The total number of counts also influences the results, where higher counts give a more accurate and precise value. However, the number of counts is limited by the dynamic range of the CCD camera, which depends on the resolution of the ADC. In our microscope, the maximum pixel value is 4095 (12-bit ADC), making difficult to obtain a total count above 10^4 on a single data volume. Total counts higher than 10^4 require the accumulation of several data volumes. This means to loose the advantage of fast acquisition that is the main reason for using the RLD algorithm.

The accuracy error of the α_1/α_2 ratio is always higher than that of the other parameters due to the accumulation of the errors in α_1 and α_2. The best accuracy error for the ratio was near 20%. The RLD algorithm allows obtaining errors and uncertainties lower than 10%, except for the accuracies of α_1 and of the ratio. These lower values are attainable for higher counts and Δt from 1500 to 2500 ps.

The error and uncertainty of τ_1 are higher than for τ_2. This is an expected result since the IRF was not deconvoluted from the data. The RLD equations are accurate only when the width of the excitation laser pulse is at least two orders of magnitude shorter than the fluorescence lifetime. This requirement is not met in the developed microscope. It would be necessary to use a femtosecond pulsed laser. The accuracy and precision will increase if the IRF was deconvoluted from the fluorescence data. The Instrumentation Group published an article detailing a deconvolution algorithm for used with RLD for mono-exponential decays [80]. As far as we know, there is no equivalent algorithm for bi-exponential decays.

The main conclusion of this study is that it is impossible to obtain metabolic information using the RLD algorithm due to low accuracy even for high total counts. Despite being

possible to increase the precision of the ratio for high total counts, this condition is not obtainable in a experiment based in endogenous fluorescence due to the weak emission from the sample, the need to limit the acquisition time for live samples, due to photobleaching, and the reduced dynamic range of gated intensified cameras.

Chapter 7

Conclusions

7.1 Conclusions 78

7.2 Future work 79

7.1 Conclusions

The system was built to measure FAD fluorescence signals of thick biological tissues. Therefore, it excites the fluorophores with a central wavelength of 440 nm and acquires the emitted fluorescence photons in the range of 520 and 570 nm. The system proved to be functional, capable of measuring the fluorescence signal from samples. The performance of the microscope was evaluated by successive tests of different elements of the system. The FOV parameter of the objective with higher magnification (230 x 170 μm^2) fulfills the requirements (200 x 300 μm^2). The system also has a lateral resolution better than the required, suitable to distinguish structures in distances 17 μm shorter than the expected. The timing resolution, which indicates the accuracy of lifetime estimation, fulfills the requirements (400 ps). Yet, it is necessary to measure the IRF before the lifetime estimation to remove its influence on the measured fluorescence data. The lifetime estimation is more accurate for longer lifetimes. The previous work [6] obtained similar results for these parameters, which strengthens the confidence in the developed system.

The optical sectioning does not fulfill the requirements, exceeding the value more than 6 μm. The most adequate method to measure this parameter uses fluorescent microspheres, but these samples were not available at our laboratory. Therefore, the tests were done with a fluorescent plastic slide, which affected the quality of the measurements. Regarding the light-sheet thickness, was obtained a value higher than other state of the art light-sheet fluorescence microscopes found in literature [22, 31]. The error of the beam waist is very high. Thus, it is important to improve the measurement process, by reducing sources of systematic error, and to increase the number of measurements to reduce the uncertainty. Another method to measure the thickness of the beam is based on a beam profiler camera. Although a beam profiler was available at the laboratory, its working distance made it unsuitable to our needs. The optical sectioning of the microscope is related to the light-sheet. So, a higher thickness degrades the optical sectioning.

The goal of the microscope is the acquisition of data to obtain fluorescence lifetime images. The microscope was used to acquire FAD fluorescence signals from pig corneas. It was necessary to use high camera gains of 500 V, corresponding to 1.05 cnts/e^-, and exposure times up to 5.12 seconds to amplify the signal due to the low concentration of FAD in the cornea. Although it was verified that the acquired signal corresponds to endogenous fluorescence of the cornea, the fitted lifetimes do not agree with reference lifetimes for FAD fluorescence in pig corneas. This is most probably due to the lack of optical sectioning, which degrades image contrast and causes simultaneous excitation and, therefore,

detection of signals from epithelial (or endothelial) FAD and stromal collagen. To achieve images with better contrast and more accurate decay lifetimes, it is necessary to improve the optical sectioning of the microscope by decreasing the width of the light-sheet.

The computational study on the performance of the RLD algorithm, when used to analyze FAD fluorescence decay, showed that, for a gate width of 1000 ps, a time interval between two consecutive gates from 1500 to 2500 ps allows a stable value of error and uncertainty. However, the lower accuracy error of the free to protein-bound ratio is near 20%, which leads to erroneous evaluations of the metabolic process. Therefore, the RLD is not suitable for metabolic imaging based on the ratio of the pre-exponential factors of the FAD decay.

7.2 Future work

The microscope implemented on this project was the first work on the group using light-sheet illumination. The optical setup used to produce the light-sheet needs to be improved to reduce its thickness and increase the optical sectioning. The used telecentric objective proved to be inadequate for the illumination setup due to its low numerical aperture. In fact, light-sheet microscopes typically use, in the illumination setup, an objective with a higher numerical aperture of 0.3 [29, 59, 67]. Using a higher numerical aperture objective decreases the light-sheet thickness [29, 32]. Although we had two Olympus Plan N objectives available, they could not be used simultaneously on the microscope setup, due to conflicts of space, caused by their physical dimensions and their working distances, that prevented them from being placed perpendicularly to each other.

The determination of the axial resolution should be based on fluorescent microspheres to provide a more accurate result. The calculation of the theoretical values of the axial resolution and light-sheet thickness is useful to compare with the measured values. A 3D reconstruction of the propagation of the light-sheet would be interesting to evaluate the shape of the beam.

The cornea has a low concentration of the FAD fluorophore. Therefore, it is convenient to choose a fluorophore with a higher concentration. The Nicotinamide Adenine Dinucleotide (NAD(P)H) fluorophore is also used for metabolic imaging and has a higher concentration on cells [6]. Nonetheless, the excitation of this fluorophore requires ultraviolet light, which means that the laser should be replaced by one with a central wavelength in the ultraviolet region (340 nm) [6, 81]. This alteration would be costly considering the purchase of a new laser and other optical components. Also, the ultraviolet light has a higher damage

potential through photochemical interactions.

References

[1] T. W. Smith, "Corneal topography," *Documenta Ophthalmologica*, vol. 43, no. 2, pp. 249–276, 1977.

[2] J. P. Whitcher, M. Srinivasan, and M. P. Upadhyay, "Corneal blindness: a global perspective," *Bulletin of the world health organization*, vol. 79, pp. 214–221, 2001.

[3] E. B. van Munster and T. W. Gadella, "Fluorescence lifetime imaging microscopy (flim)," *Microscopy techniques*, pp. 143–175, 2005.

[4] J. W. Lichtman and J.-A. Conchello, "Fluorescence microscopy," *Nature methods*, vol. 2, no. 12, pp. 910–919, 2005.

[5] J. R. Lakowicz, *Principles of fluorescence spectroscopy*. Springer science & business media, 2013.

[6] S. F. Silva, *Time-Gated Fluorescence Lifetime Microscopy Methods and Instrumentation for Metabolic Imaging*. PhD thesis, 00500:: Universidade de Coimbra, 2019.

[7] A. Jain, C. Blum, and V. Subramaniam, "Fluorescence lifetime spectroscopy and imaging of visible fluorescent proteins," in *Advances in Biomedical Engineering*, pp. 147–176, Elsevier, 2009.

[8] L. Marcu, P. M. French, and D. S. Elson, *Fluorescence lifetime spectroscopy and imaging: principles and applications in biomedical diagnostics*. CRC Press, 2014.

[9] J. Siegel, D. S. Elson, S. E. Webb, K. B. Lee, A. Vlandas, G. L. Gambaruto, S. Leveˆque-Fort, M. J. Lever, P. J. Tadrous, G. W. Stamp, *et al.*, "Studying biological tissue with fluorescence lifetime imaging: microscopy, endoscopy, and complex decay profiles," *Applied optics*, vol. 42, no. 16, pp. 2995–3004, 2003.

[10] C.-W. Chang, D. Sud, and M.-A. Mycek, "Fluorescence lifetime imaging microscopy," *Methods in cell biology*, vol. 81, pp. 495–524, 2007.

[11] X. F. Wang, A. Periasamy, B. Herman, and D. M. Coleman, "Fluorescence lifetime imaging microscopy (flim): instrumentation and applications," *Critical Reviews in Analytical Chemistry*, vol. 23, no. 5, pp. 369–395, 1992.

[12] P. I. Bastiaens and A. Squire, "Fluorescence lifetime imaging microscopy: spatial resolution of biochemical processes in the cell," *Trends in cell biology*, vol. 9, no. 2, pp. 48–52, 1999.

[13] R. Datta, T. M. Heaster, J. T. Sharick, A. A. Gillette, and M. C. Skala, "Fluorescence lifetime imaging microscopy: fundamentals and advances in instrumentation, analysis, and applications," *Journal of biomedical optics*, vol. 25, no. 7, p. 071203, 2020.

[14] M. Cole, J. Siegel, S. Webb, R. Jones, K. Dowling, M. J. Dayel, D. Parsons-Karavassilis, P. French, M. Lever, L. Sucharov, *et al.*, "Time-domain whole-field fluorescence lifetime imaging with optical sectioning," *Journal of Microscopy*, vol. 203, no. 3, pp. 246–257, 2001.

[15] C.-W. Chang, *Improving accuracy and precision in biological applications of fluorescence lifetime imaging microscopy*. PhD thesis, University of Michigan, 2009.

[16] J. W. Borst and A. J. Visser, "Fluorescence lifetime imaging microscopy in life sciences," *Measurement Science and Technology*, vol. 21, no. 10, p. 102002, 2010.

[17] W. Becker, *Advanced time-correlated single photon counting techniques*, vol. 81. Springer Science & Business Media, 2005.

[18] M. Wahl, "Time-correlated single photon counting," *Technical Note*, pp. 1–14, 2014.

[19] D. O'Connor, *Time-correlated single photon counting*. Academic Press, 2012.

[20] W. Becker, *Advanced time-correlated single photon counting applications*, vol. 111. Springer, 2015.

[21] J. McGinty, J. Requejo-Isidro, I. Munro, C. Talbot, P. Kellett, J. Hares, C. Dunsby, M. Neil, and P. French, "Signal-to-noise characterization of time-gated intensifiers used for wide-field time-domain flim," *Journal of Physics D: Applied Physics*, vol. 42, no. 13, p. 135103, 2009.

[22] R. Li, A. Liu, T. Wu, W. Xiao, L. Tang, and L. Chen, "Digital scanned laser light-sheet fluorescence lifetime microscopy with wide-field time-gated imaging," *Journal of microscopy*, vol. 279, no. 1, pp. 69–76, 2020.

[23] J. Huisken and D. Y. Stainier, "Selective plane illumination microscopy techniques in developmental biology," 2009.

[24] M. Weber and J. Huisken, "Light sheet microscopy for real-time developmental biology," *Current opinion in genetics & development*, vol. 21, no. 5, pp. 566–572, 2011.

[25] E. G. Reynaud, U. Kržič, K. Greger, and E. H. Stelzer, "Light sheet-based fluorescence microscopy: more dimensions, more photons, and less photodamage," *HFSP journal*, vol. 2, no. 5, pp. 266–275, 2008.

[26] P. A. Santi, "Light sheet fluorescence microscopy: a review," *Journal of Histochemistry & Cytochemistry*, vol. 59, no. 2, pp. 129–138, 2011.

[27] A. H. Voie, D. Burns, and F. Spelman, "Orthogonal-plane fluorescence optical sectioning: Three-dimensional imaging of macroscopic biological specimens," *Journal of microscopy*, vol. 170, no. 3, pp. 229–236, 1993.

[28] J. Huisken, J. Swoger, F. Del Bene, J. Wittbrodt, and E. H. Stelzer, "Optical sectioning deep inside live embryos by selective plane illumination microscopy," *Science*, vol. 305, no. 5686, pp. 1007–1009, 2004.

[29] J. M. Girkin and M. T. Carvalho, "The light-sheet microscopy revolution," *Journal of Optics*, vol. 20, no. 5, p. 053002, 2018.

[30] K. Greger, M. J. Neetz, E. G. Reynaud, and E. H. Stelzer, "Three-dimensional fluorescence lifetime imaging with a single plane illumination microscope provides an improved signal to noise ratio," *Optics express*, vol. 19, no. 21, pp. 20743–20750, 2011.

[31] T. Funane, S. S. Hou, K. M. Zoltowska, S. J. van Veluw, O. Berezovska, A. T. Kumar, and B. J. Bacskai, "Selective plane illumination microscopy (spim) with time-domain fluorescence lifetime imaging microscopy (flim) for volumetric measurement of cleared mouse brain samples," *Review of Scientific Instruments*, vol. 89, no. 5, p. 053705, 2018.

[32] R. M. Power and J. Huisken, "A guide to light-sheet fluorescence microscopy for multiscale imaging," *Nature methods*, vol. 14, no. 4, pp. 360–373, 2017.

[33] C. Berney and G. Danuser, "Fret or no fret: a quantitative comparison," *Biophysical journal*, vol. 84, no. 6, pp. 3992–4010, 2003.

[34] A. Periasamy, P. Wodnicki, X. F. Wang, S. Kwon, G. W. Gordon, and B. Herman, "Time-resolved fluorescence lifetime imaging microscopy using a picosecond pulsed tunable dye laser system," *Review of Scientific Instruments*, vol. 67, no. 10, pp. 3722–3731, 1996.

[35] C. B. Talbot, R. Patalay, I. Munro, S. Warren, F. Ratto, P. Matteini, R. Pini, H. G. Breunig, K. König, A. C. Chu, *et al.*, "Application of ultrafast gold luminescence to measuring the instrument response function for multispectral multiphoton fluorescence lifetime imaging," *Optics Express*, vol. 19, no. 15, pp. 13848–13861, 2011.

[36] S. C. Warren, A. Margineanu, D. Alibhai, D. J. Kelly, C. Talbot, Y. Alexandrov, I. Munro, M. Katan, C. Dunsby, and P. M. French, "Rapid global fitting of large fluorescence lifetime imaging microscopy datasets," *PloS one*, vol. 8, no. 8, p. e70687, 2013.

[37] R. Woods, S. Scypinski, and L. C. Love, "Transient digitizer for the determination of microsecond luminescence lifetimes," *Analytical Chemistry*, vol. 56, no. 8, pp. 1395–1400, 1984.

[38] K. K. Sharman, A. Periasamy, H. Ashworth, and J. Demas, "Error analysis of the rapid lifetime determination method for double-exponential decays and new windowing schemes," *Analytical chemistry*, vol. 71, no. 5, pp. 947–952, 1999.

[39] R. M. Ballew and J. Demas, "An error analysis of the rapid lifetime determination method for the evaluation of single exponential decays," *Analytical Chemistry*, vol. 61, no. 1, pp. 30–33, 1989.

[40] A. J. Walsh, R. S. Cook, M. E. Sanders, L. Aurisicchio, G. Ciliberto, C. L. Arteaga, and M. C. Skala, "Quantitative optical imaging of primary tumor organoid metabolism predicts drug response in breast cancer," *Cancer research*, vol. 74, no. 18, pp. 5184–5194, 2014.

[41] M. Y. Berezin and S. Achilefu, "Fluorescence lifetime measurements and biological imaging," *Chemical reviews*, vol. 110, no. 5, pp. 2641–2684, 2010.

[42] S. Webb, Y. Gu, S. Lévêque-Fort, J. Siegel, M. Cole, K. Dowling, R. Jones, P. French, M. Neil, R. Juškaitis, *et al.*, "A wide-field time-domain fluorescence lifetime imaging microscope with optical sectioning," *Review of Scientific Instruments*, vol. 73, no. 4, pp. 1898–1907, 2002.

[43] PicoQuant, "Sepia PDL 828 - picosecond pulsed drivers," 2021.

[44] PicoQuant, "LDH series," 2021.

[45] H. Sun, *A practical guide to handling laser diode beams*, vol. 147. Springer, 2015.

[46] LaVision, "PicoStar HR manual," 2003.

[47] K. Greger, J. Swoger, and E. Stelzer, "Basic building units and properties of a fluorescence single plane illumination microscope," *Review of Scientific Instruments*, vol. 78, no. 2, p. 023705, 2007.

[48] I. Thorlabs, "Imaging microscope objectives, dry," 2021.

[49] Olympus, "PLN/ LPLN - achromat objectives," 2021.

[50] M. World, "Infinity corrected optics," 2021.

[51] E. Optics, "The advantages of telecentricity," 2021.

[52] I. Thorlabs, "Scan lenses for laser scanning microscopy," 2021.

[53] S. Optics, "F-theta lenses," 2021.

[54] I. Thorlabs, "Imaging catalog," 2021.

[55] I. Thorlabs, "N-BK7 bi-convex lenses, uncoated," 2021.

[56] I. Thorlabs, "Mounted N-BK7 plano-convex lenses (uncoated)," 2021.

[57] I. Thorlabs, "Mounted plano-convex round cylindrical lenses, N-BK7," 2021.

[58] I. Thorlabs, "Beam expander design comparison: Keplerian and galilean," 2021.

[59] C. Chardès, P. Mélénec, V. Bertrand, and P.-F. Lenne, "Setting up a simple light sheet microscope for in toto imaging of c. elegans development," *JoVE (Journal of Visualized Experiments)*, no. 87, p. e51342, 2014.

[60] I. Thorlabs, "Resolution test targets," 2021.

[61] H. Kaur and N. Sohi, "A study for applications of histogram in image enhancement," *Int. J. Eng. Sci*, vol. 6, no. 6, pp. 59–63, 2017.

[62] J. Im, J. Jeon, M. H. Hayes, and J. Paik, "Single image-based ghost-free high dynamic range imaging using local histogram stretching and spatially-adaptive denoising," *IEEE Transactions on Consumer Electronics*, vol. 57, no. 4, pp. 1478–1484, 2011.

[63] E. Glynn, "Usaf 1951 and microcopy resolution test charts and pixel profiles," *Photonics Spectra*, pp. 183–189, 1999.

[64] J. M. Khosrofian and B. A. Garetz, "Measurement of a gaussian laser beam diameter through the direct inversion of knife-edge data," *Applied optics*, vol. 22, no. 21, pp. 3406–3410, 1983.

[65] M. A. de Araújo, R. Silva, E. de Lima, D. P. Pereira, and P. C. de Oliveira, "Measurement of gaussian laser beam radius using the knife-edge technique: improvement on data analysis," *Applied optics*, vol. 48, no. 2, pp. 393–396, 2009.

[66] T. F. Johnston, "Beam propagation (m 2) measurement made as easy as it gets: the four-cuts method," *Applied optics*, vol. 37, no. 21, pp. 4840–4850, 1998.

[67] J. G. Ritter, R. Veith, J.-P. Siebrasse, and U. Kubitscheck, "High-contrast single-particle tracking by selective focal plane illumination microscopy," *Optics express*, vol. 16, no. 10, pp. 7142–7152, 2008.

[68] R. Scott Harris, D. R. Hess, and J. G. Venegas, "An objective analysis of the pressure-volume curve in the acute respiratory distress syndrome," *American journal of respiratory and critical care medicine*, vol. 161, no. 2, pp. 432–439, 2000.

[69] C. Sheppard, "Microscopy overview," 2004.

[70] E. Instruments, "Fluorescence lifetime standards data table," 2021.

[71] I. Sanchez, R. Martin, F. Ussa, and I. Fernandez-Bueno, "The parameters of the porcine eyeball," *Graefe's Archive for Clinical and Experimental Ophthalmology*, vol. 249, no. 4, pp. 475–482, 2011.

[72] L. Jay, A. Brocas, K. Singh, J.-C. Kieffer, I. Brunette, and T. Ozaki, "Determination of porcine corneal layers with high spatial resolution by simultaneous second and third harmonic generation microscopy," *Optics express*, vol. 16, no. 21, pp. 16284–16293, 2008.

[73] N. E. Institute, "NEI media library," 2019.

[74] Z. Chen, J. You, X. Liu, S. Cooper, C. Hodge, G. Sutton, J. M. Crook, and G. G. Wallace, "Biomaterials for corneal bioengineering," *Biomedical Materials*, vol. 13, no. 3, p. 032002, 2018.

[75] A. Batista, H. G. Breunig, A. Uchugonova, A. M. Morgado, and K. König, "Two-photon spectral fluorescence lifetime and second-harmonic generation imaging of the porcine cornea with a 12-femtosecond laser microscope," *Journal of biomedical optics*, vol. 21, no. 3, p. 036002, 2016.

[76] ISS, "Lifetime data of selected fluorophores," 2020.

[77] B. Heeg, "Precision of mono-exponential decay estimates from rapid lifetime determination in the presence of signal photon and background noise," *Measurement Science and Technology*, vol. 25, no. 10, p. 105201, 2014.

[78] S. P. Chan, Z. Fuller, J. Demas, and B. DeGraff, "Optimized gating scheme for rapid lifetime determinations of single-exponential luminescence lifetimes," *Analytical Chemistry*, vol. 73, no. 18, pp. 4486–4490, 2001.

[79] S. F. Silva, J. P. Domingues, and A. M. Morgado, "Can we use rapid lifetime determination for fast, fluorescence lifetime based, metabolic imaging? precision and accuracy of double-exponential decay measurements with low total counts," *Plos one*, vol. 14, no. 5, p. e0216894, 2019.

[80] S. F. Silva, J. P. Domingues, and A. M. Morgado, "Accurate rapid lifetime determination on time-gated flim microscopy with optical sectioning," *Journal of healthcare engineering*, vol. 2018, 2018.

[81] Biotek, "Determination of NADH or NADPH concentrations with the FL600™ fluorescence microplate reader using fluorescence or absorbance modes," 2006.

Appendix A

Data analysis

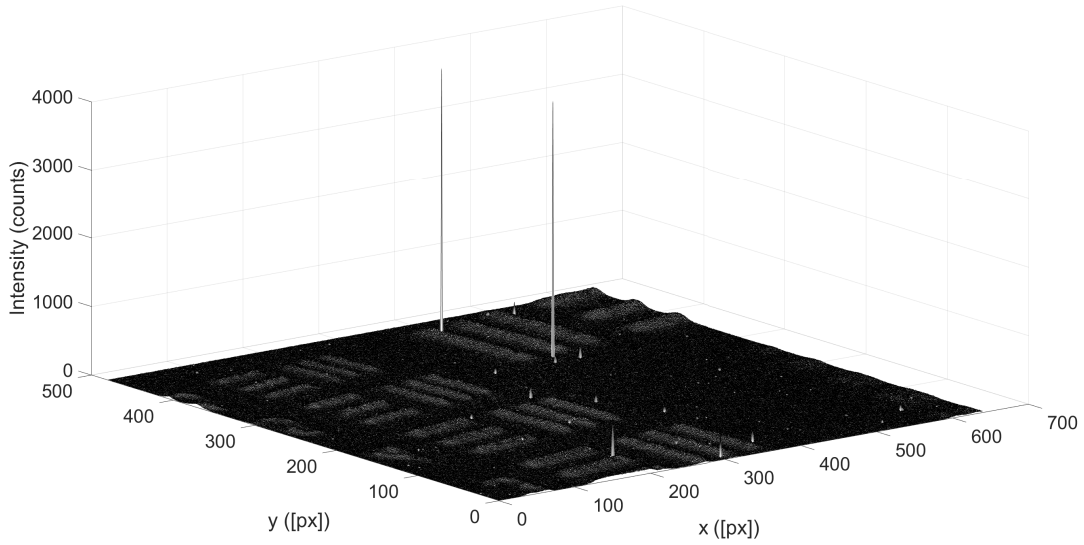

Figure A.1: Intensity plot of the target image acquired with Olympus Plan N 40x objective.

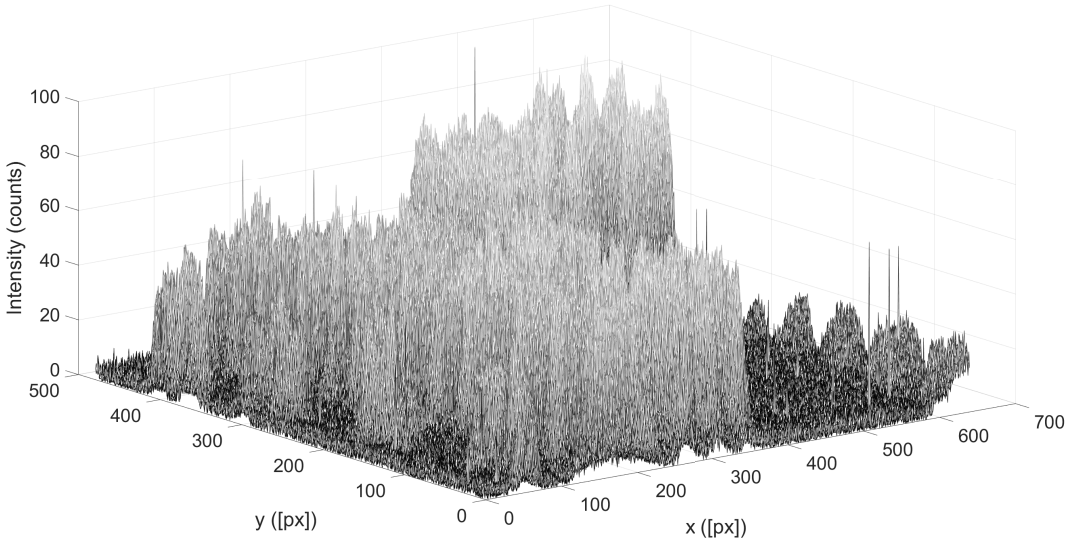

Figure A.2: Intensity plot of the target image acquired with Olympus Plan N 40x objective with outliers removed.

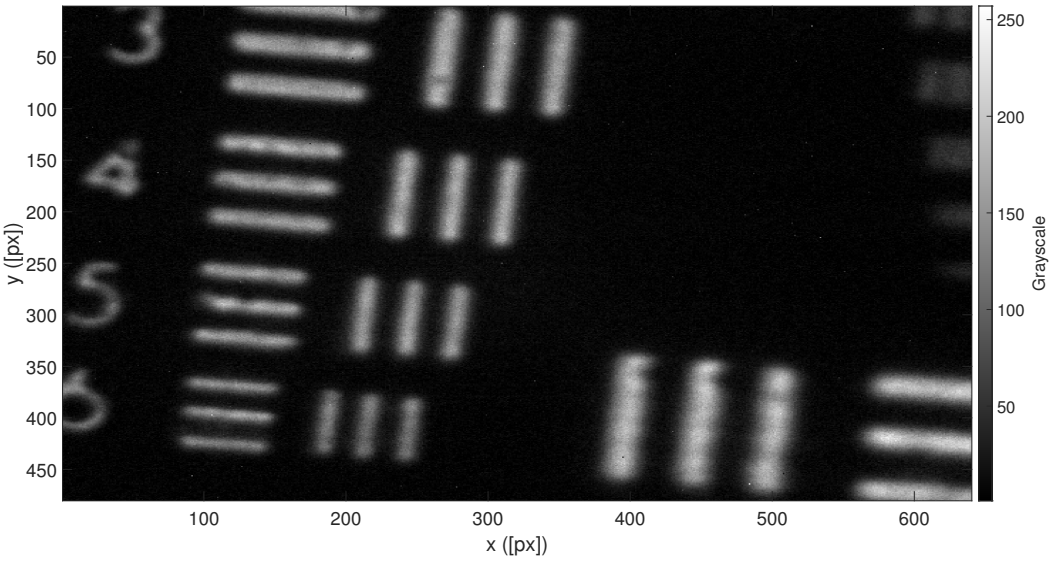

Figure A.3: Acquired target image with Olympus Plan N 40x objective with the histogram stretching enhancement and outliers removed.

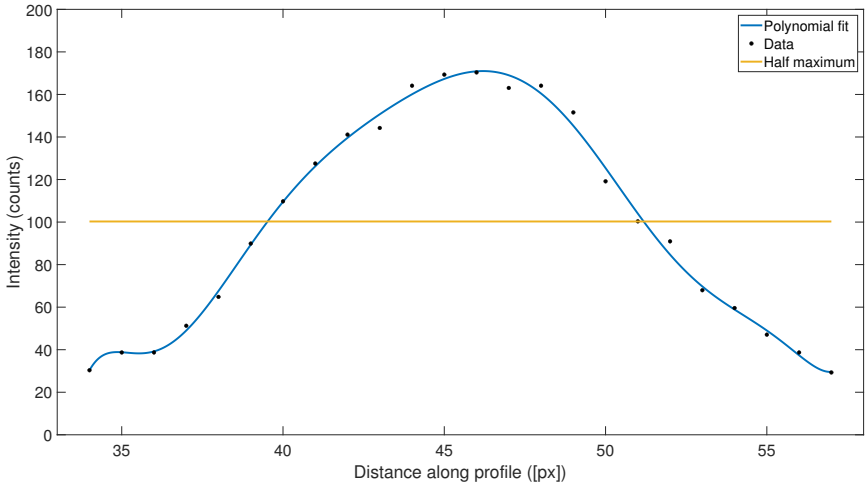

(a) Detection unit with Olympus Plan N 20x for the y-axis.

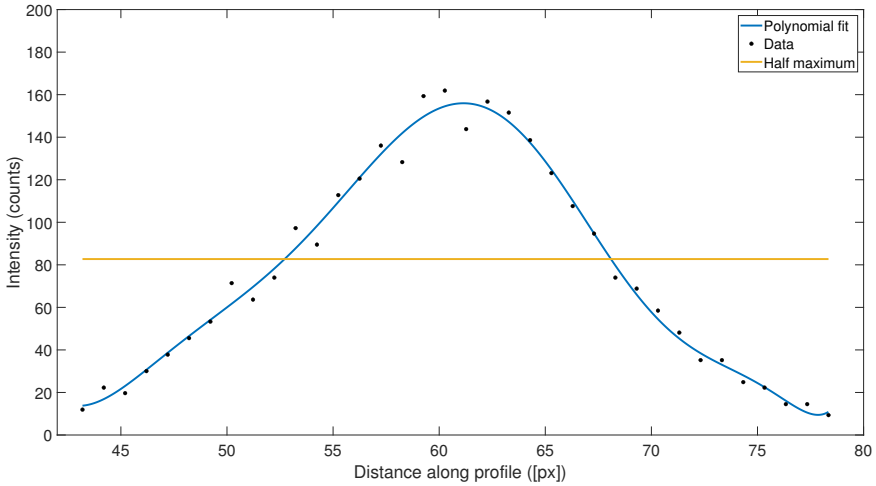

(b) Detection unit with Olympus Plan N 40x for the x-axis.

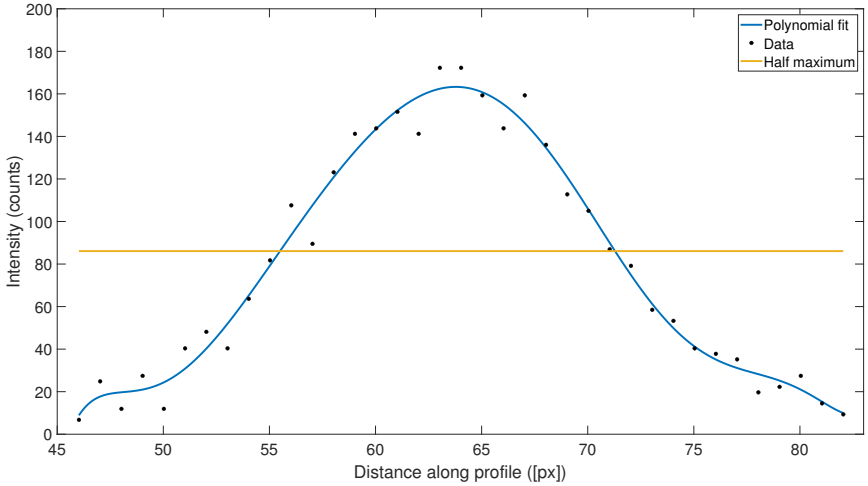

(c) Detection unit with Olympus Plan N 40x for the y-axis.

Figure A.4: Plot of the middle peak data, the corresponding nine-degree polynomial fit, and the half-maximum intensity of the the detection unit. This plot allow obtaining the width in number of pixels of one line of the target for the detection unit.

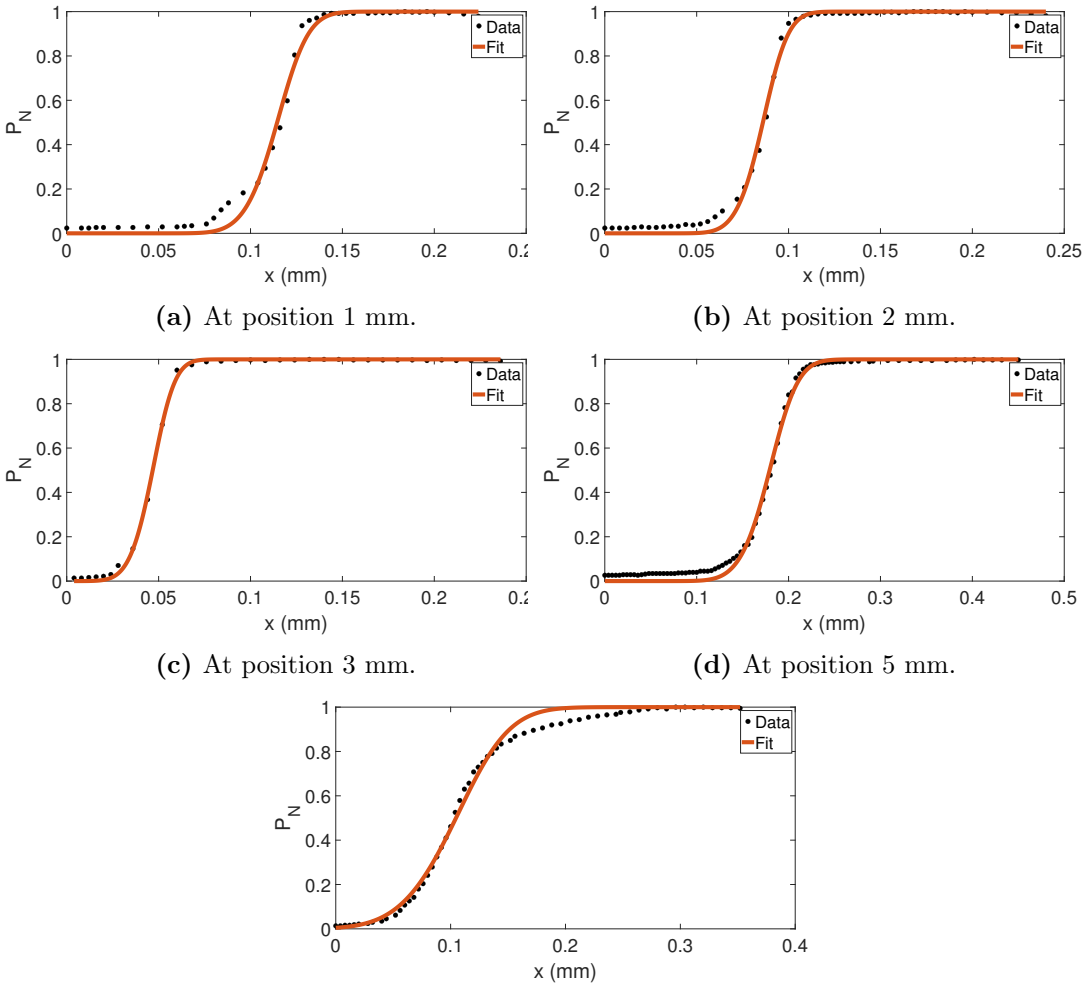

(a) At position 1 mm.

(b) At position 2 mm.

(c) At position 3 mm.

(d) At position 5 mm.

(e) At position 9 mm.

Figure A.5: Plot of the measured data with the Khosrofian and Garetz fit at different positions across the beam propagation. P_N is the normalized power and x is the position of the knife-edge.

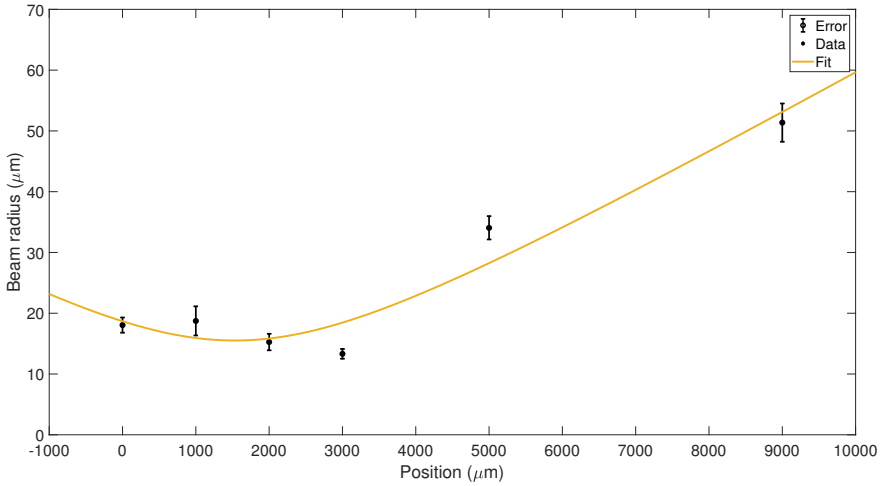

(a) For $M^2 = 1$.

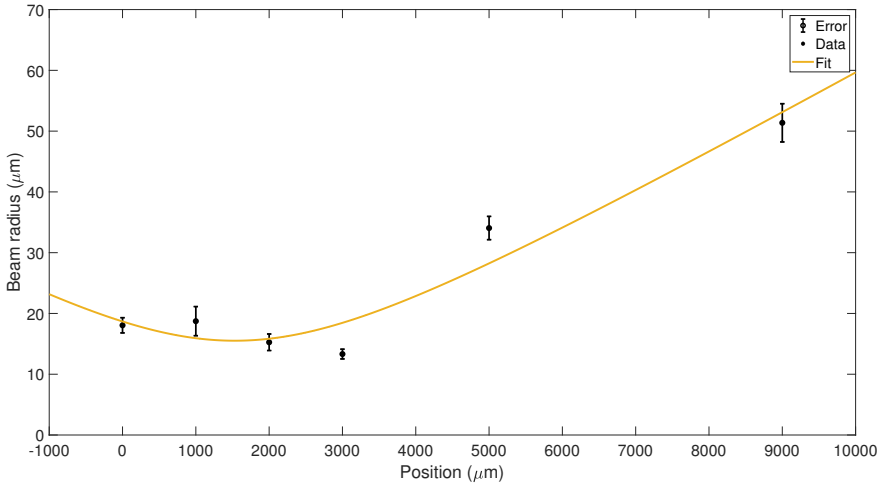

(b) For $M^2 = 1.5$.

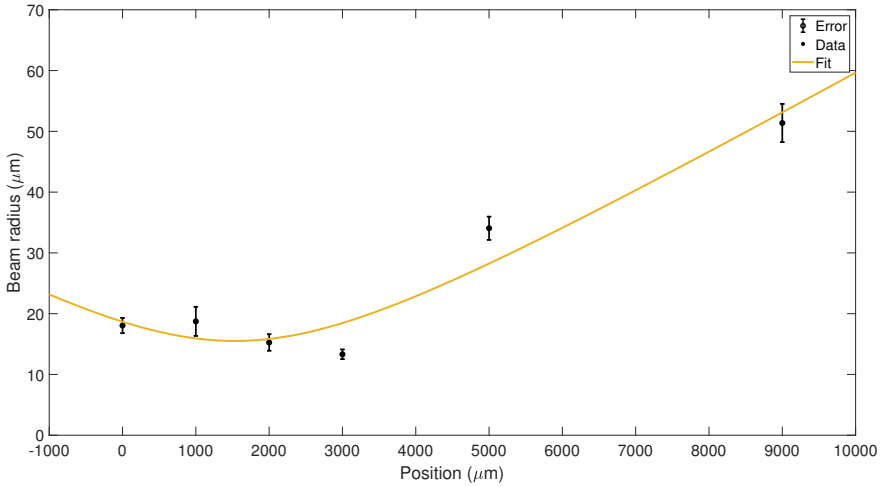

(c) For $M^2 = 3$.

Figure A.6: Plot of the obtained beam radius as a function of the position with the respective beam waist fit for different values of M^2.

Appendix B

Fluorescence decay of cornea images

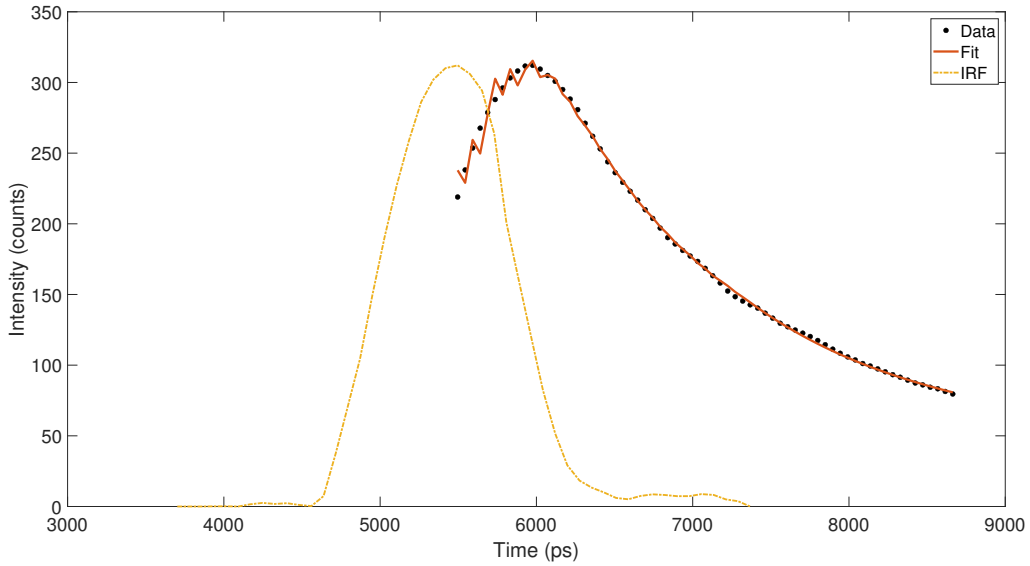

Figure B.1: Plot of the fluorescence decay and bi-exponential fit of the epithelium images acquired with Olympus Plan N 20x.

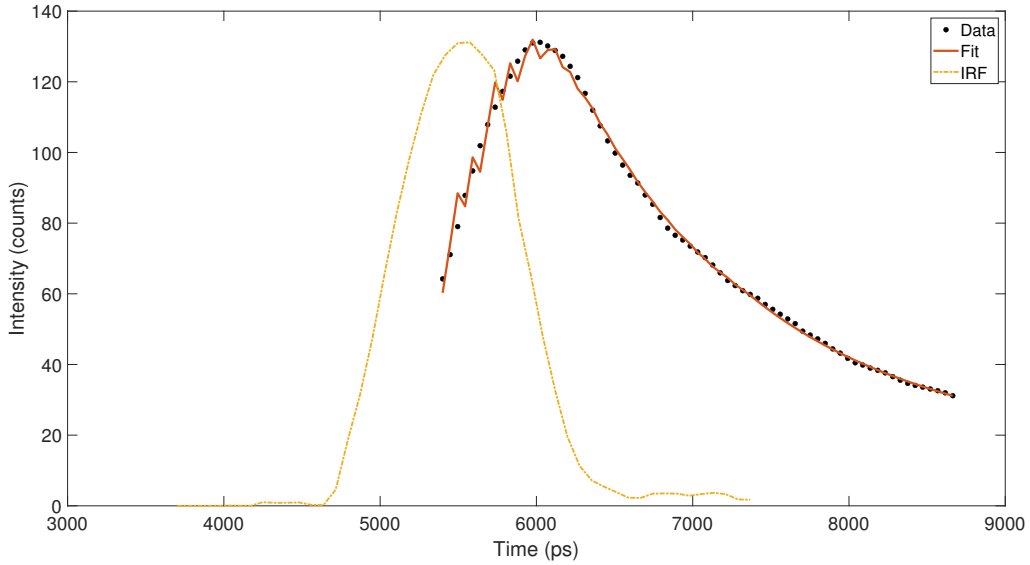

Figure B.2: Plot of the fluorescence decay and bi-exponential fit of the epithelium images acquired with Olympus Plan N 40x.

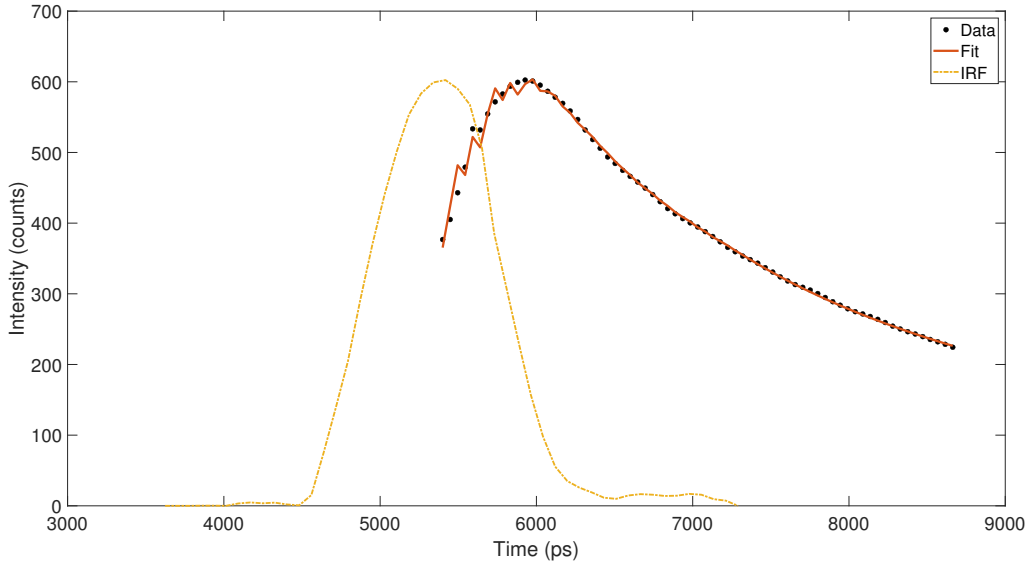

Figure B.3: Plot of the fluorescence decay and bi-exponential fit of the endothelium images acquired with Olympus Plan N 20x.

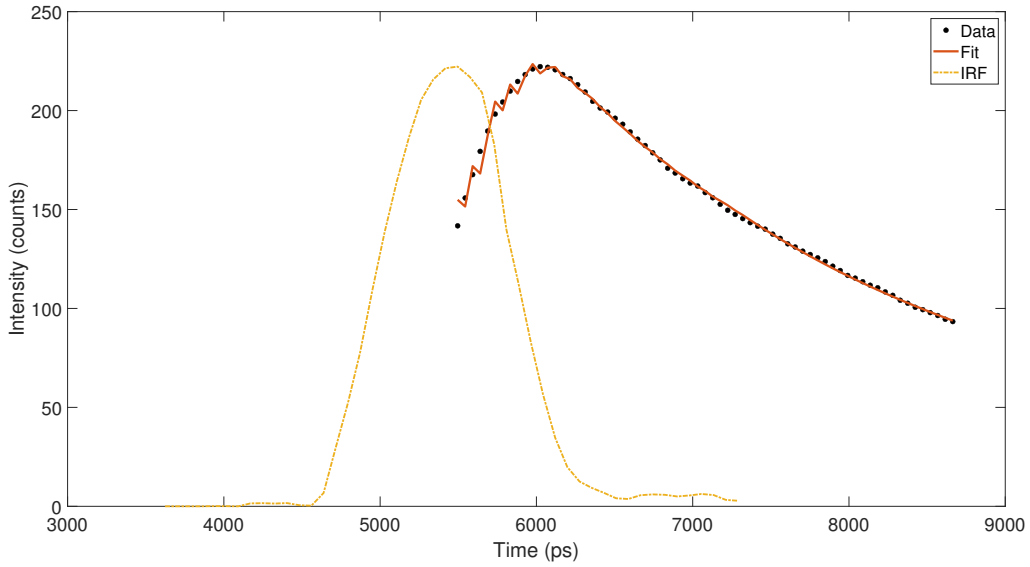

Figure B.4: Plot of the fluorescence decay and bi-exponential fit of the endothelium images acquired with Olympus Plan N 40x.

Appendix C

Simulations

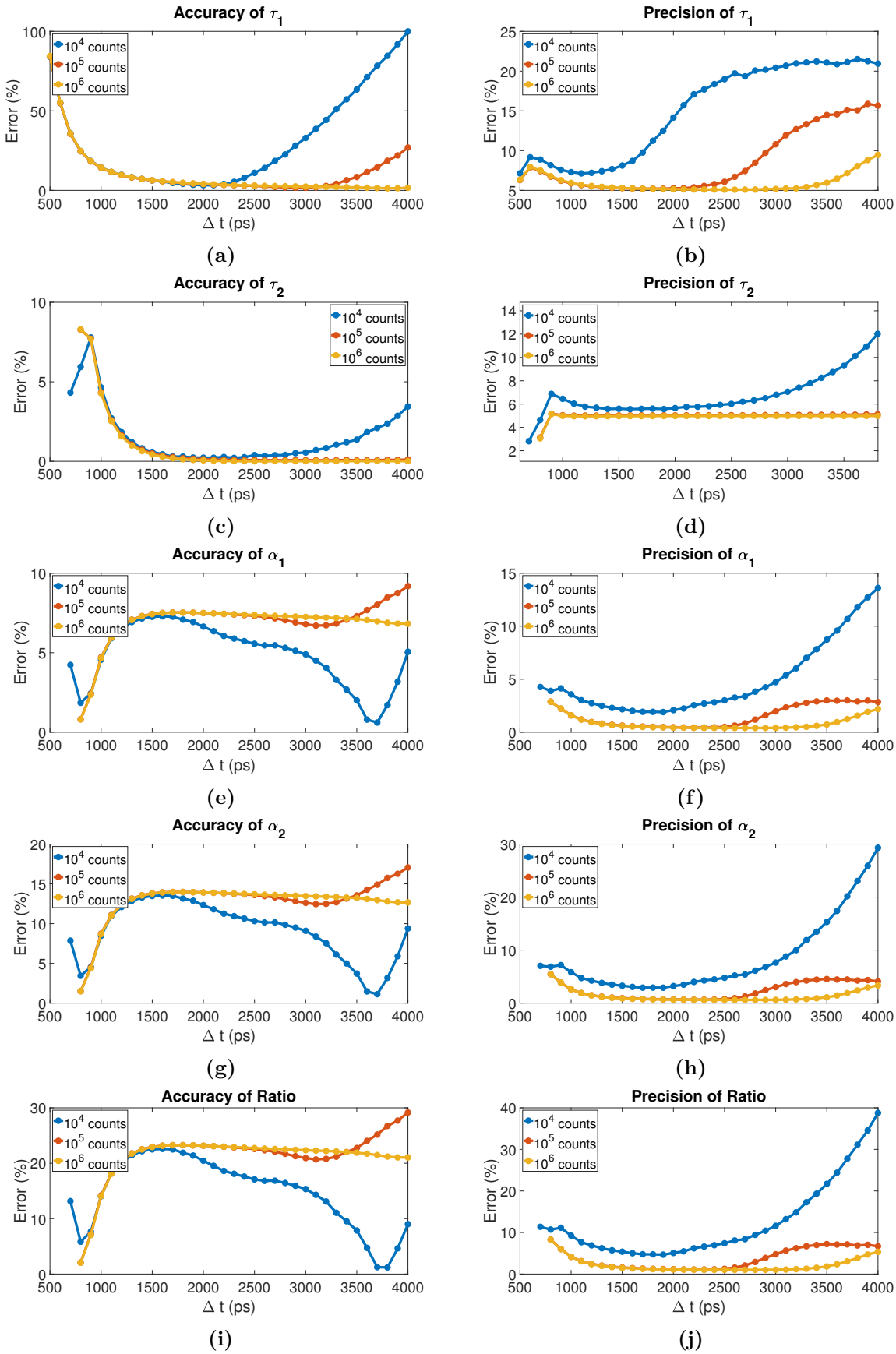

Figure C.1: Accuracy and precision errors of the parameters τ_1, τ_2, α_1, α_2 and ratio as a function of the Δt for 1.05 cnts/e$^-$ and laser power set to 80%.

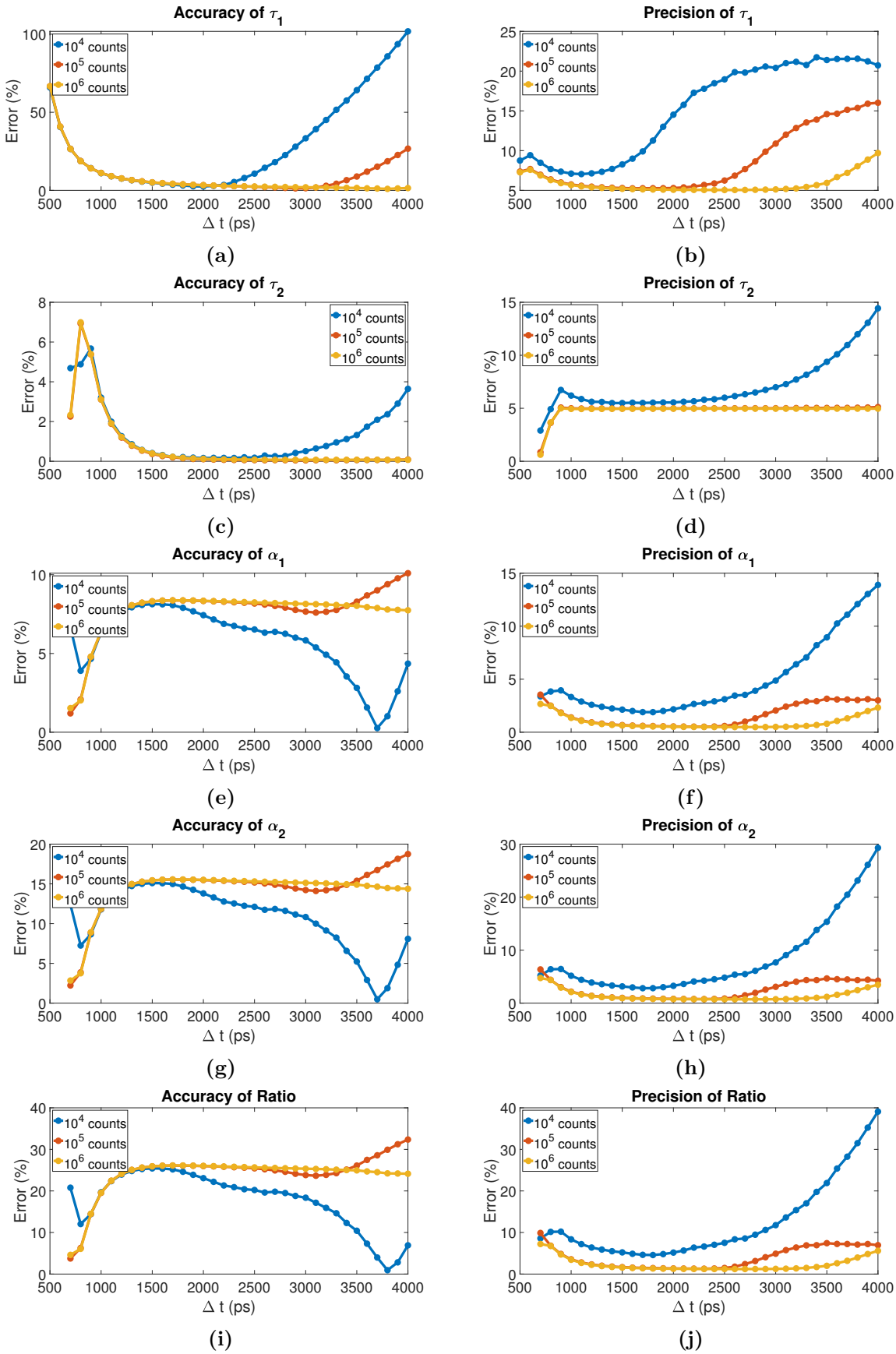

Figure C.2: Accuracy and precision errors of the parameters τ_1, τ_2, α_1, α_2 and ratio as a function of the Δt for 1.05 cnts/e$^-$ and laser power set to 90%.

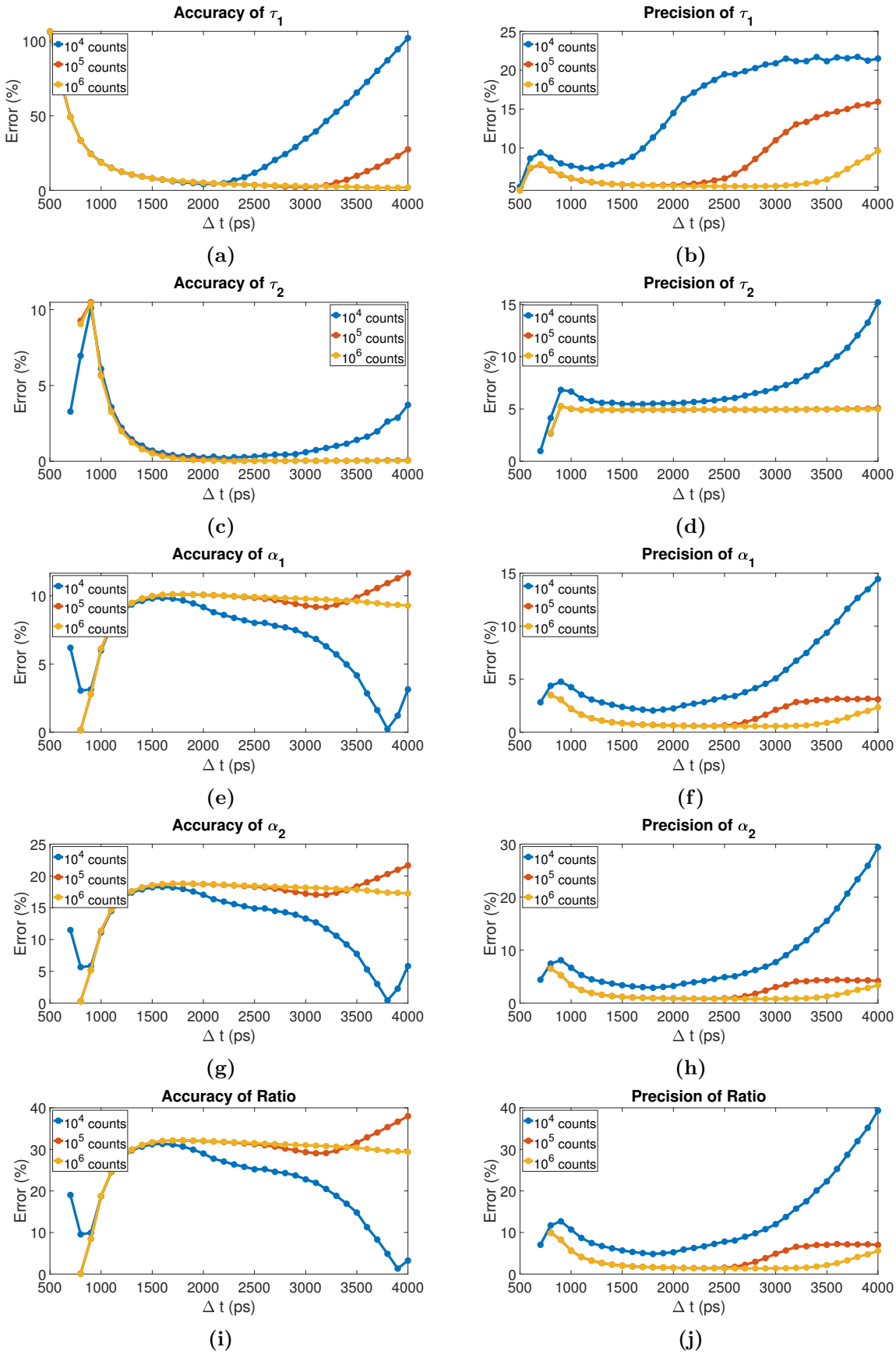

Figure C.3: Accuracy and precision errors of the parameters τ_1, τ_2, α_1, α_2 and ratio as a function of the Δt for 1.05 cnts/e$^-$ and laser power set to 100%.

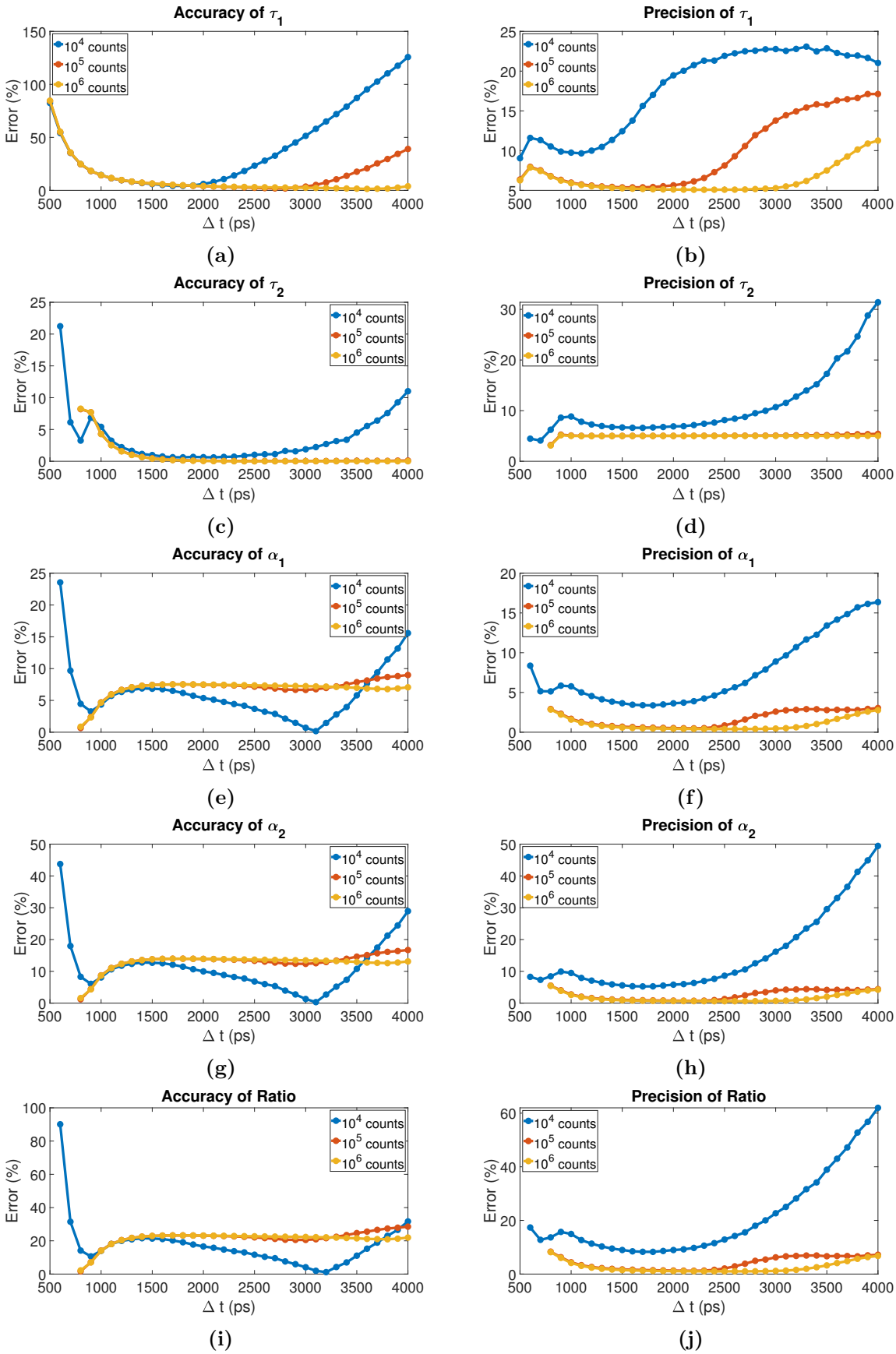

Figure C.4: Accuracy and precision errors of the parameters τ_1, τ_2, α_1, α_2 and ratio as a function of the Δt for 2.41 cnts/e$^-$ and laser power set to 80%.

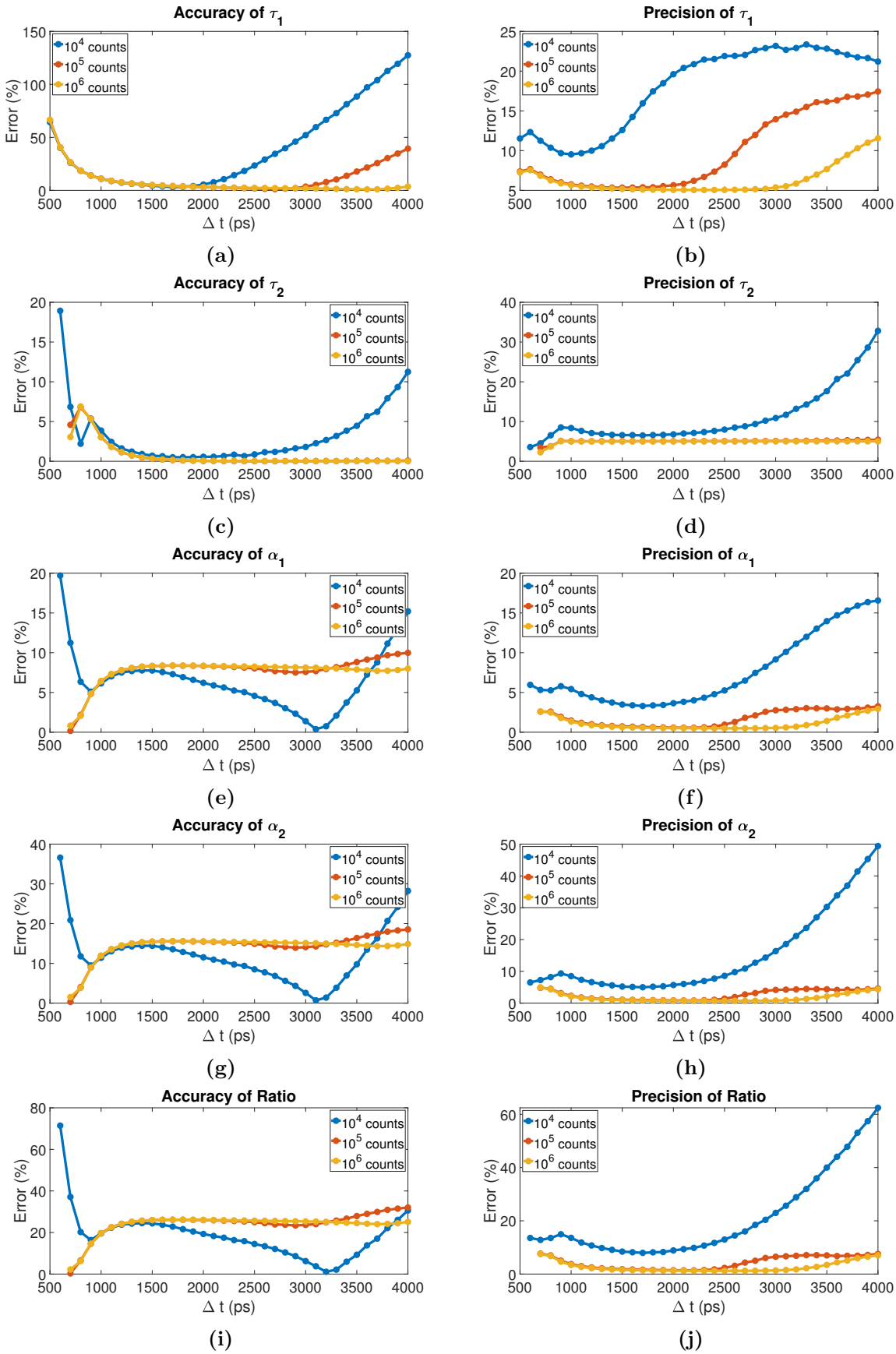

Figure C.5: Accuracy and precision errors of the parameters τ_1, τ_2, α_1, α_2 and ratio as a function of the Δt for 2.41 cnts/e$^-$ and laser power set to 90%.

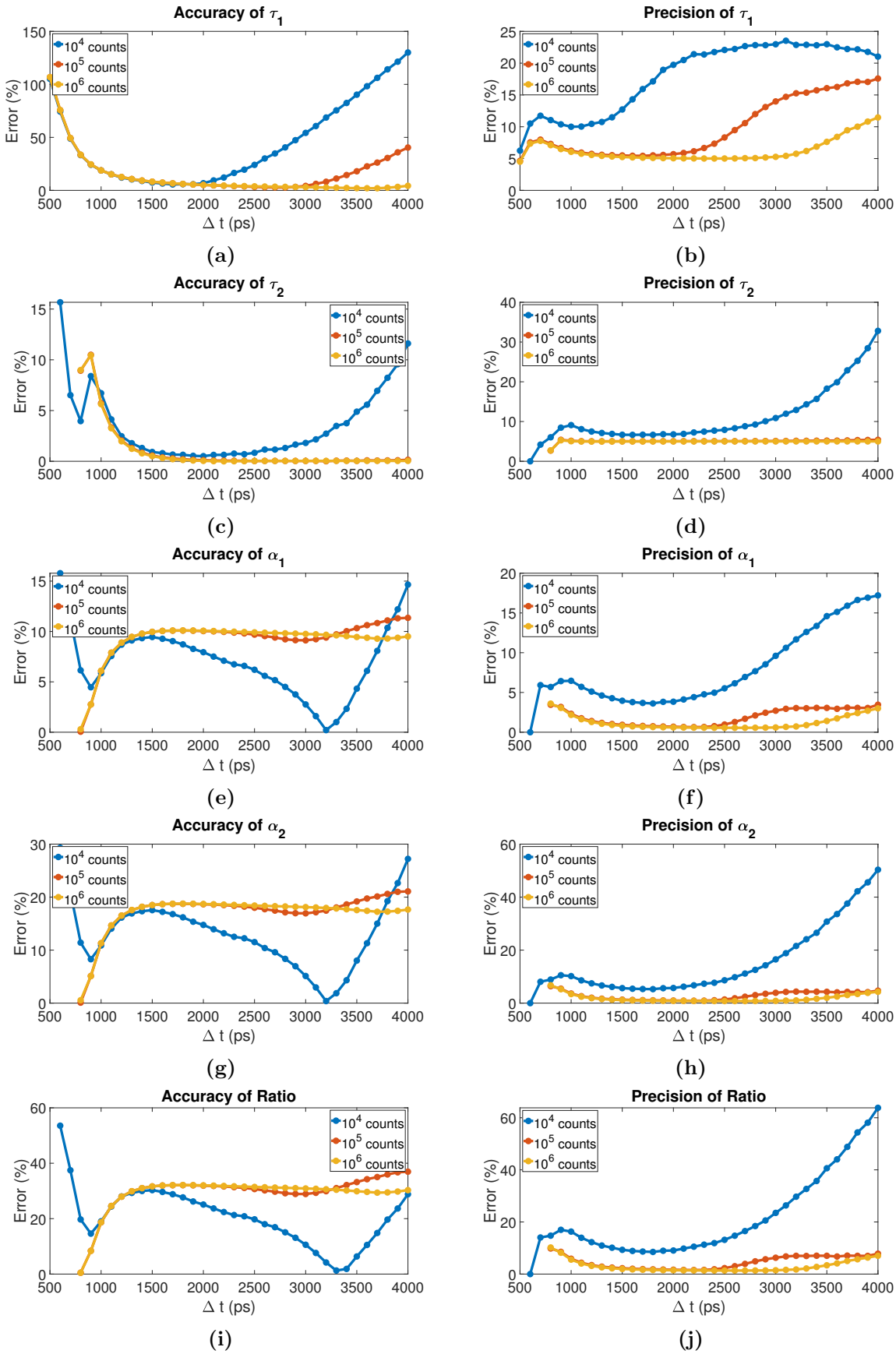

Figure C.6: Accuracy and precision errors of the parameters τ_1, τ_2, α_1, α_2 and ratio as a function of the Δt for 2.41 cnts/e$^-$ and laser power set to 100%.

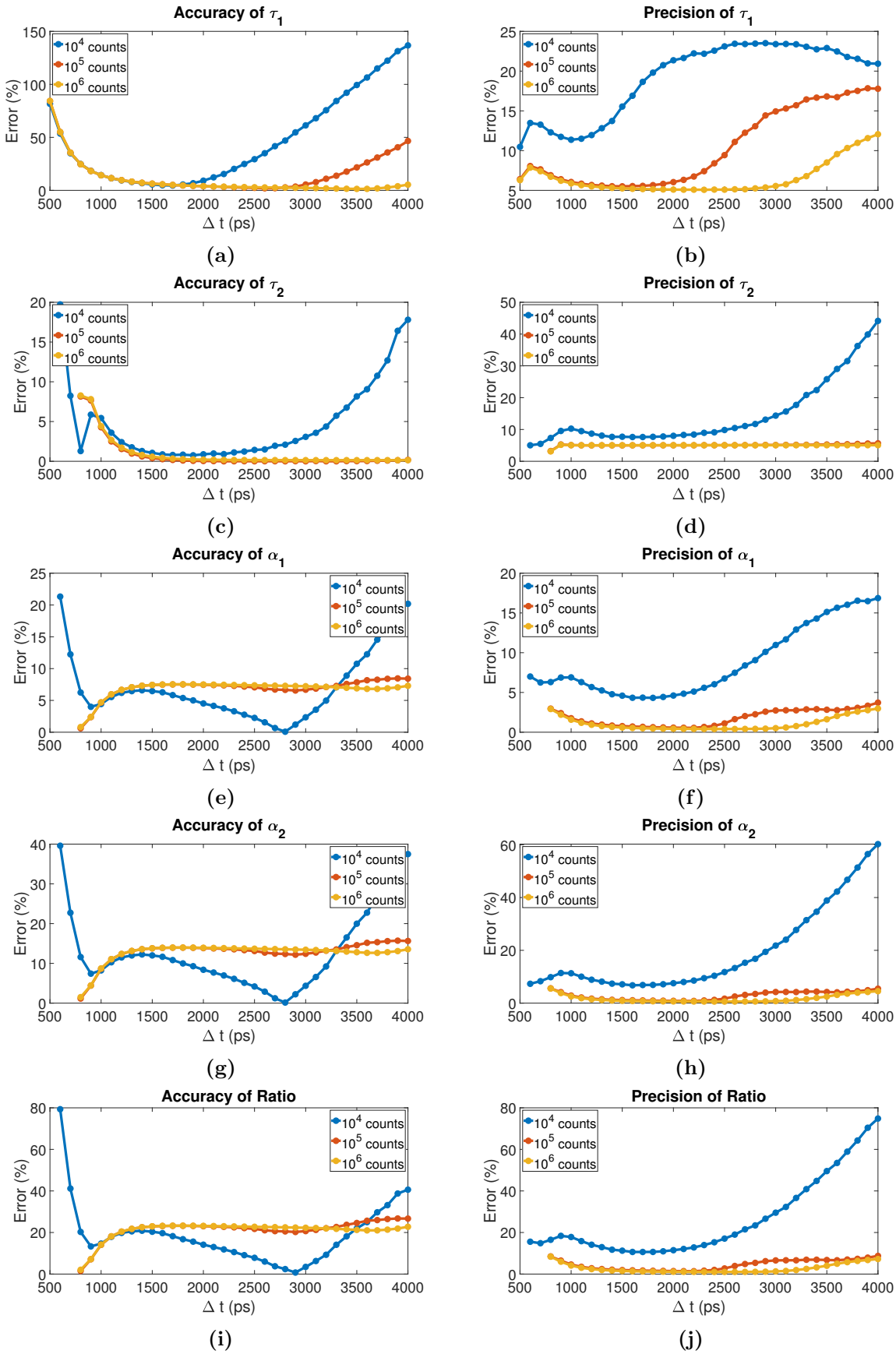

Figure C.7: Accuracy and precision errors of the parameters τ_1, τ_2, α_1, α_2 and ratio as a function of the Δt for 5.2 cnts/e$^-$ and laser power set to 80%.

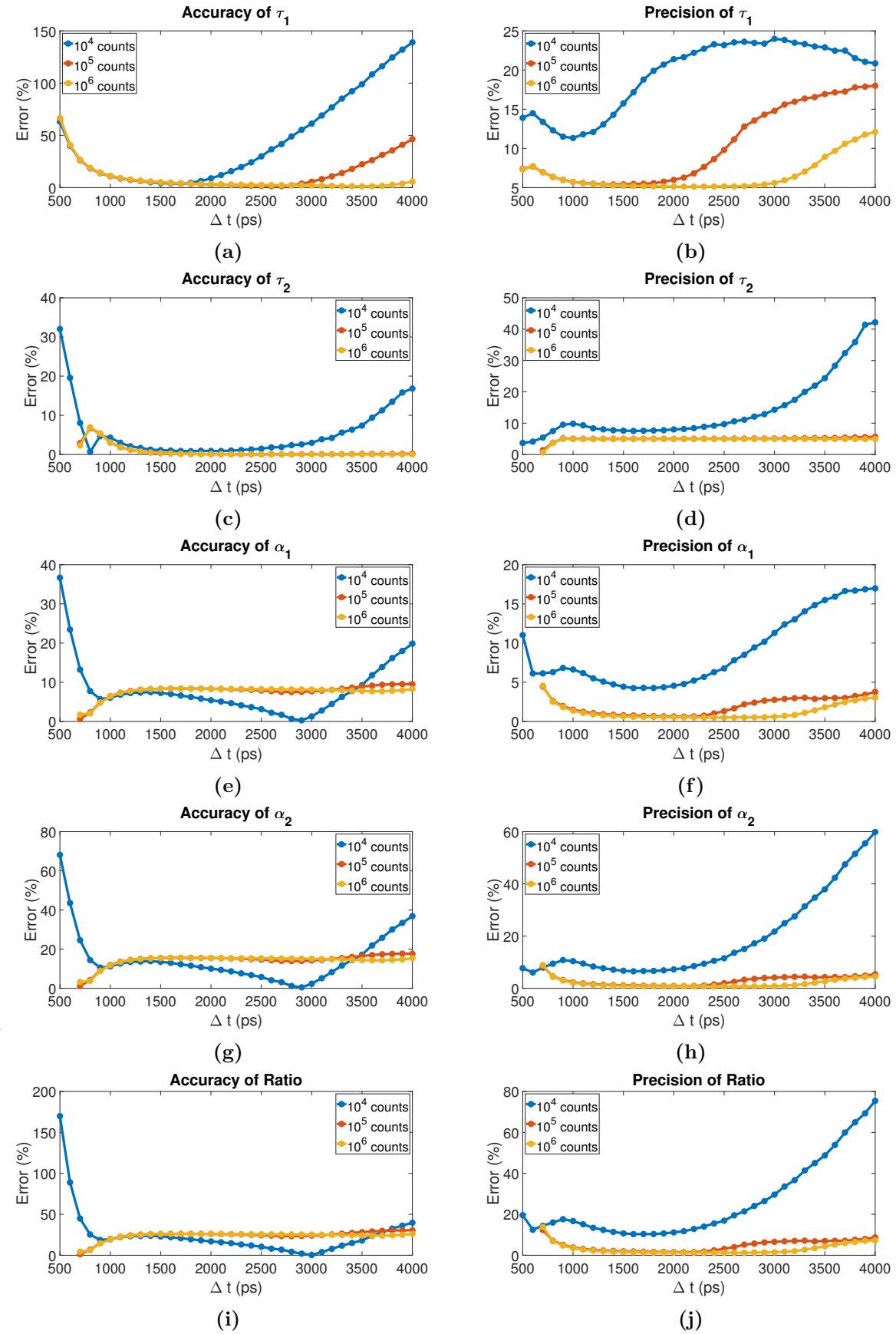

Figure C.8: Accuracy and precision errors of the parameters τ_1, τ_2, α_1, α_2 and ratio as a function of the Δt for 5.2 cnts/e$^-$ and laser power set to 90%.

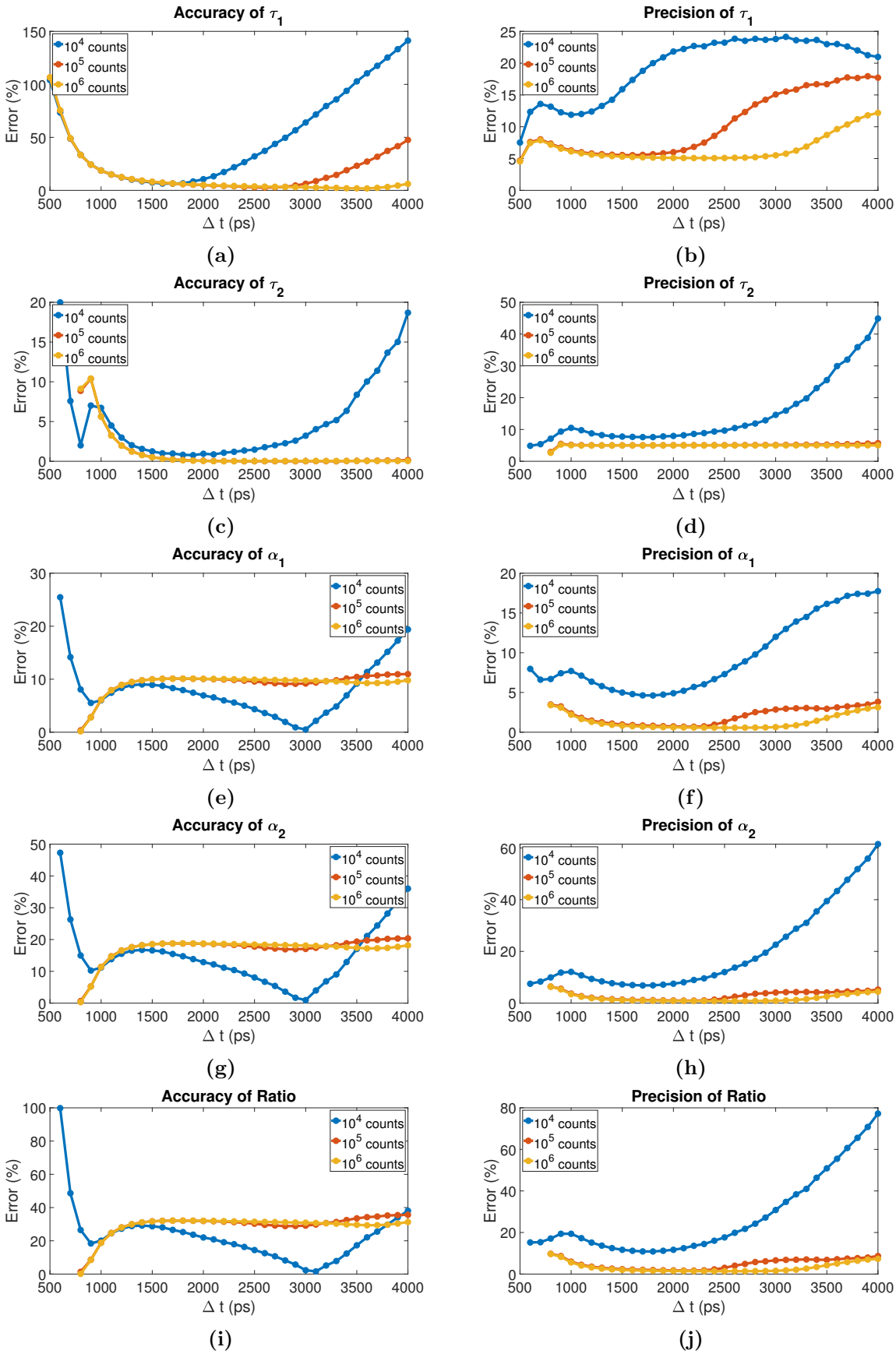

Figure C.9: Accuracy and precision errors of the parameters τ_1, τ_2, α_1, α_2 and ratio as a function of the Δt for 5.2 cnts/e$^-$ and laser power set to 100%.

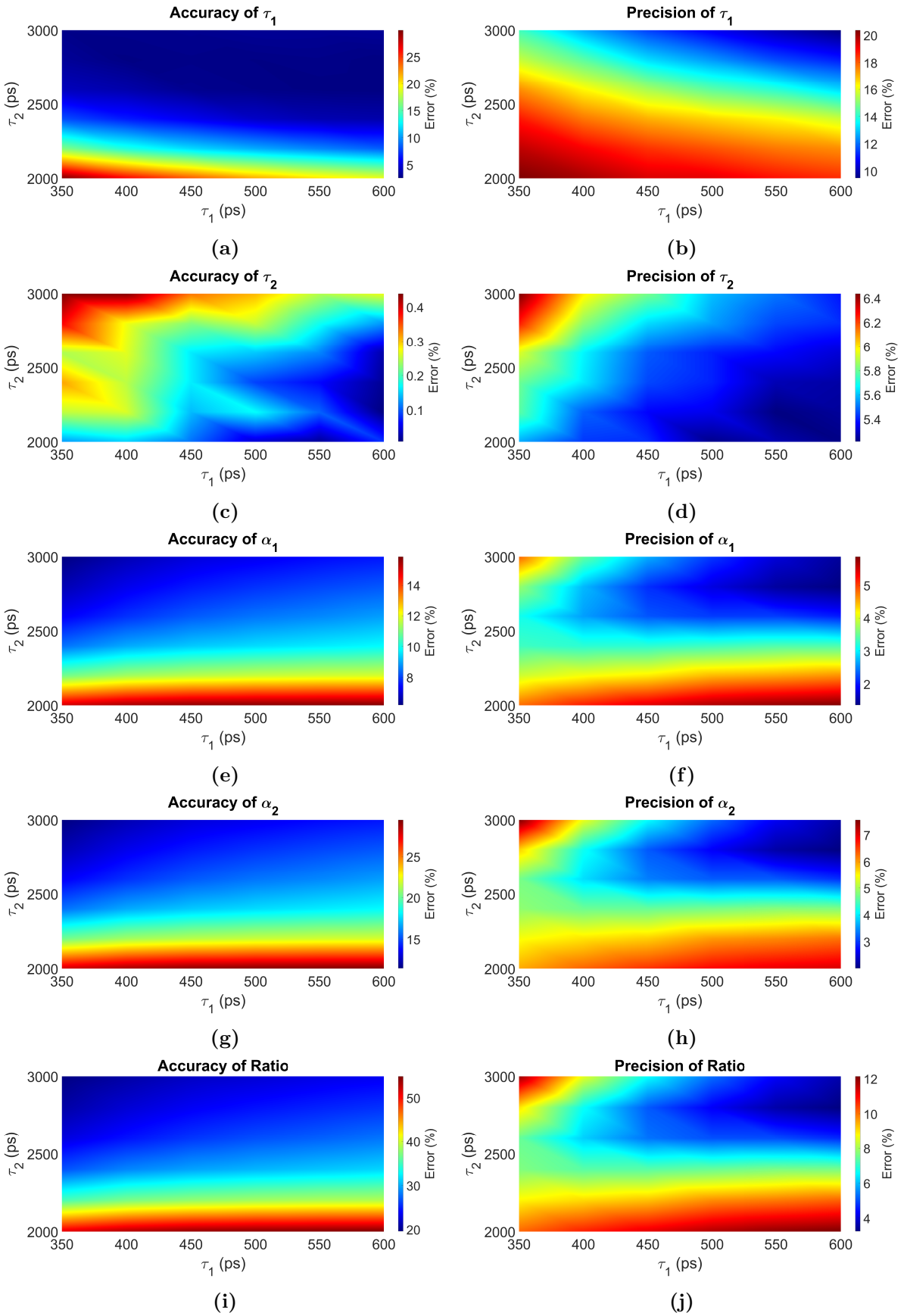

Figure C.10: Accuracy and precision errors of the parameters τ_1, τ_2, α_1, α_2 and ratio as a function of τ_1 and τ_2 for 1.05 cnts/e$^-$, 10^4 total counts and laser power set to 90%.

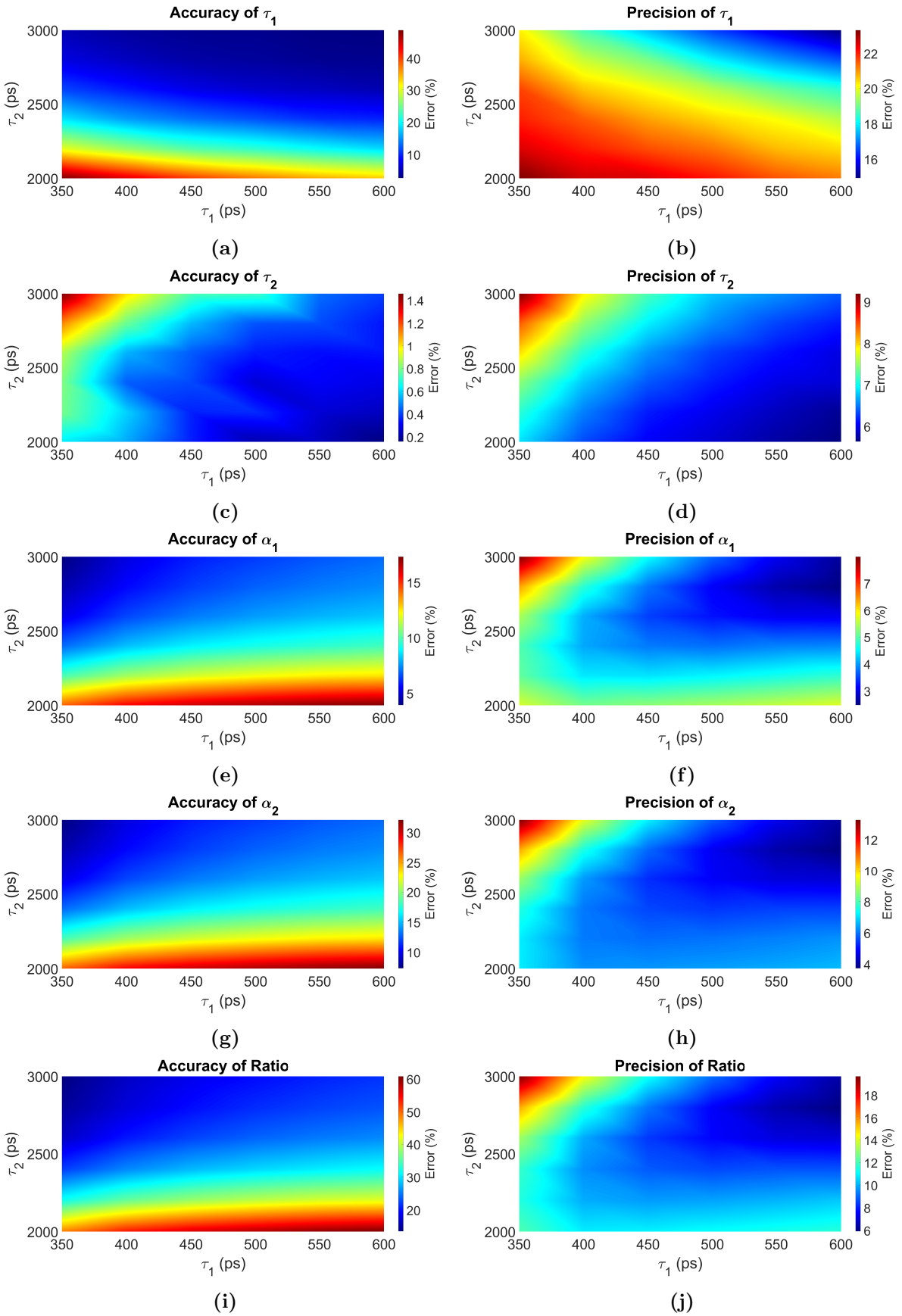

Figure C.11: Accuracy and precision errors of the parameters τ_1, τ_2, α_1, α_2 and ratio as a function of τ_1 and τ_2 for 2.41 cnts/e$^-$, 10^4 total counts and laser power set to 90%.

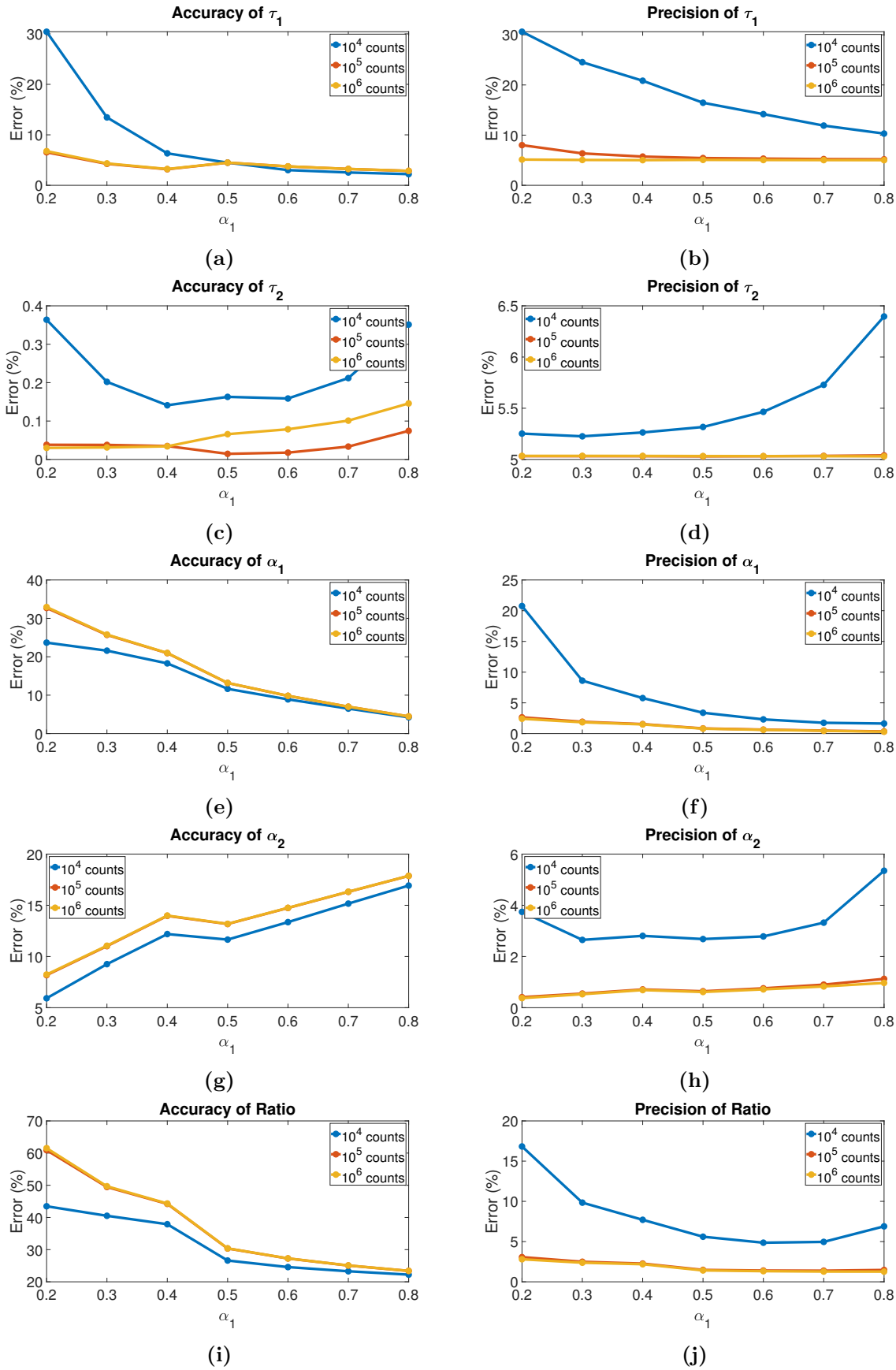

Figure C.12: Accuracy and precision errors of the parameters τ_1, τ_2, α_1, α_2 and ratio as a function of the α_1 for 1.05 cnts/e$^-$ and laser power set to 90%.

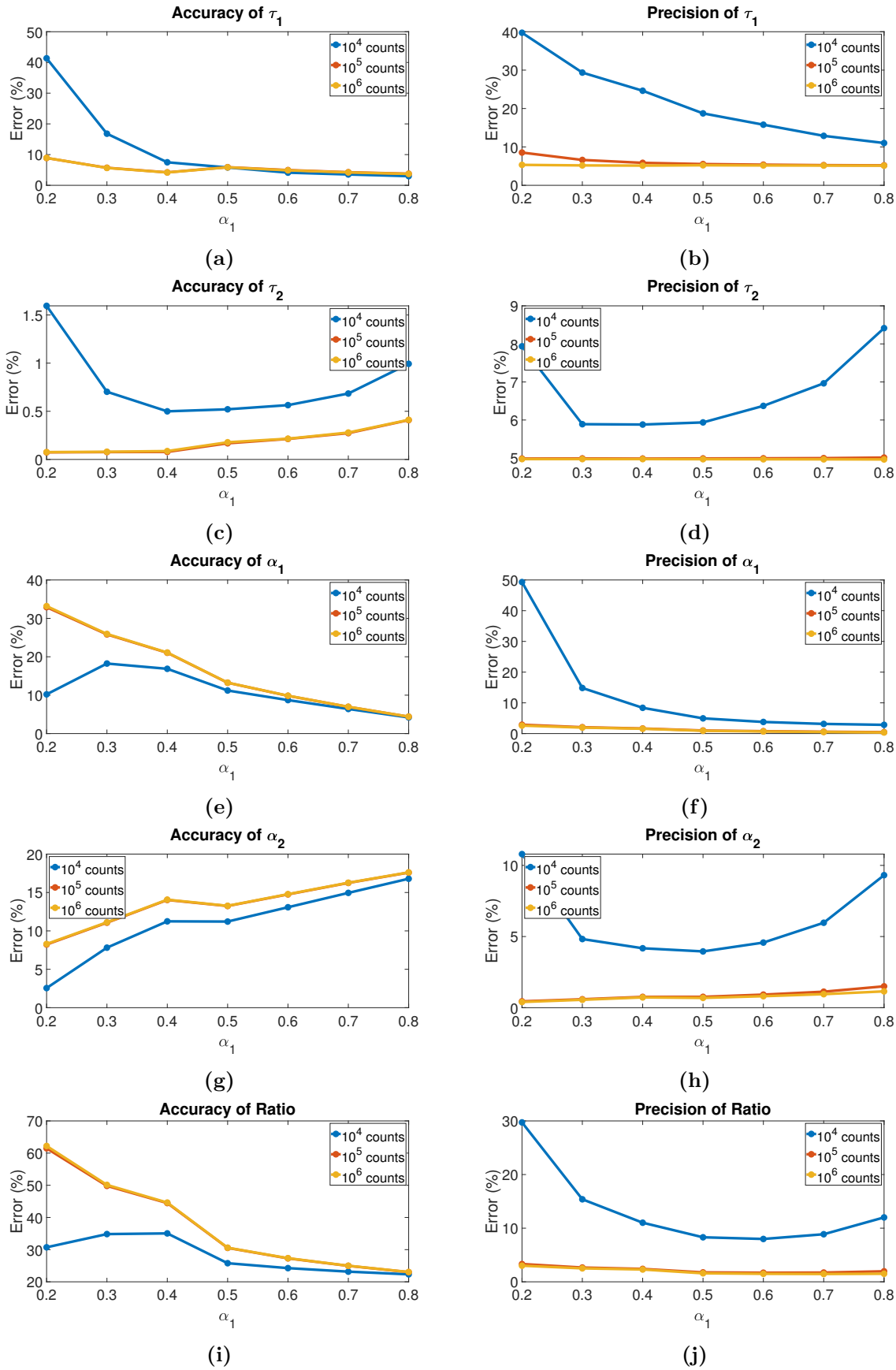

Figure C.13: Accuracy and precision errors of the parameters τ_1, τ_2, α_1, α_2 and ratio as a function of the α_1 for 2.41 cnts/e$^-$ and laser power set to 90%.